

DEVELOPMENT OF A HUMAN BODY MODEL (THUMS VERSION 7) TO SIMULATE KINEMATICS AND INJURIES OF RECLINED OCCUPANTS IN FRONTAL COLLISIONS

Takao Matsuda
Naoya Kobayashi
Noriyuki Fujita
Yuichi Kitagawa
Toyota Motor Corporation
Japan

Paper Number 23-0030

ABSTRACT

This paper describes the development of THUMS Version 7 which is a virtual human body model (HBM) to be used for simulating impact kinematics and injuries of occupants assuming a reclined seating posture in vehicle frontal collisions. In highly automated vehicles, it is expected that occupants wish to take various sitting positions including a reclined posture. Prior research has found that there is a relatively high possibility of injury to the occupant for a reclined posture in vehicle collisions. If the lap belt engagement with the pelvis is lost in a frontal collision, there is the possibility that the internal organs are highly loaded. The latest released Version 6 does not have precise representation of the small intestine but has a generic soft solid. It was decided to upgrade THUMS for accurate prediction of internal organ injury. The geometry and mechanical properties of the small intestine and the other relevant body parts were fundamentally revised in Version 7. The interaction between the pelvis and lap belt was most important in simulating occupant kinematics leading to the abdominal loading. The pelvis dimensions and soft tissue thickness of the anterior pelvis were carefully reviewed to represent the belt-pelvis interaction in the average body-size occupant. Three anthropometry models were generated: 5th-percentile adult female (AF05), 50th-percentile adult male (AM50), and 95th-percentile adult male (AM95). The geometry and material properties of the abdominal soft tissue, small intestine and mesentery were carefully defined to realistically reproduce the mechanical responses during the abdominal loading by referring to the loading test data on actual human tissues reported in the literature. The lumbar spine was also revised. Prior research has found that the lumbar spine receives a high load when the pelvis is firmly restrained to prevent disengagement of the lap belt in a reclined posture. The material properties of the intervertebral discs and spinal ligaments were carefully reviewed. The validity of the updated models was examined by comparing the mechanical responses with the test data from Post Mortem Human Subjects (PMHS). It was confirmed that the Version 7 responses generally matched the test data or fell within the test data variability. The validations were performed at both component and whole-body level by referring to the available test data.

INTRODUCTION

In highly automated vehicles (autonomous driving level: four or higher), occupants are partially or fully freed from driving operations. It is expected that occupants may wish to ride in various seating arrangements and postures, and to spend their ride time in unconventional ways, such as relaxing, playing games, or working. Several studies have confirmed users' expectations for a more relaxing and comfortable ride by reclining their seats in future automated vehicles [1-2]. On the other hand, the vehicle crash tests conducted in the current regulatory compliance certification and the new car assessment programs basically assume the upright seat arrangement. In the reclining seat arrangement, there is a possibility that a vehicle collision occurs while the occupants are seated in a reclined posture. It is necessary to understand the effects on impact kinematics and possible injuries of such occupants during the collision. Various studies have been conducted for this purpose, such as collision tests using PMHS and vehicle collision simulations using HBMs. Discussions are underway to determine the effectiveness of the current restraint systems and future countermeasures to better protect the occupants.

The National Highway Traffic Safety Administration (NHTSA) has investigated occupant kinematics and injuries during frontal crashes in forward-facing and rear-facing reclined seat configurations [3-4]. Richardson et al. (2020) [5] conducted a 50 kph frontal sled test of a reclined PMHS to measure the occupant kinematics and injury responses. In the reclining posture, it was reported that the initial rearward pitch of the pelvis triggered disengagement of the lap belt from the anterior pelvis. As a result, the belt shifted up to the abdominal area

(called submarining). The lumbar spine was loaded by combined compression and bending as the upper body moved forward due to inertia. In recent years, many studies have been conducted using computer simulations with HBMs. The NHTSA has suggested that HBMs could be used in the future to confirm crash safety of automated vehicles in addition to physical testing [6]. It is expected to be used as a future evaluation tool taking advantage of the flexibility in posture change and higher biofidelity. Boyle et al. (2019) [7] investigated responses in frontal crashes for vehicle occupants in reclining posture through a simulation study using HBM. Their study results indicated that the submarining is more likely to occur as the reclining angle became larger. It was also indicated that the lumbar spine was subjected to higher load when the submarining was prevented by firmly restraining the pelvis. Similar results were reported in other studies on impact kinematics and injury outcomes of reclined occupants in vehicle frontal collisions [8-11].

HBMs are widely used for vehicle collision simulations in the field of occupant safety research. The HBMs are generally validated to PMHS test data to be used for prediction of impact kinematics and injury in vehicle collisions. In the previous research, the test conditions assumed an upright seating posture. Further validations are necessary to ensure the prediction accuracy of kinematics and injury in the reclining posture. As mentioned before, when the lap belt shifted up to the abdominal area (submarining) during a frontal collision, there is a possibility that the internal organs are loaded. There is another possibility that the lumbar spine is highly loaded if the submarining is prevented. Further validations are necessary for the prediction of abdominal organ damage and lumbar spine injury due to submarining, as suggested in previous studies. The current HBMs do not fully represent the complex geometry of the small intestine and mesentery but have a generic soft solid in the corresponding region. Such a simplified model does not accurately predict organ damage. Further validation is also necessary for the prediction of lumbar spine injury. This paper describes the development work of THUMS Version 7, which will be a major update of Version 6. The development targets are 1) to accurately predict the interaction between the pelvis and lap belt of a reclining occupant, and 2) to predict injuries to the internal organs and the lumbar spine in vehicle frontal collisions.

MODEL DEVELOPMENT

Overview of THUMS Version 7

THUMS is a series of virtual human body models that precisely represents the whole-body geometry and anatomical structures of the human body and reproduces the physical properties of the constituent tissues such as bones and internal organs. The development purpose was to simulate human body kinematics in vehicle collisions and to analyze crash-induced injuries. Figure 1 shows an overall view of the newly developed THUMS Version 7 occupant models. There are three body sizes equivalent to small female (AF05), midsize male (AM50), and large male (AM95). THUMS Version 4 [12], released in 2010, included detailed anatomic structures based on high-precision CT scan data to predict bone fractures, ligament tears, and brain and internal organ injuries. Version 5 [13], released in 2015, was a major update of Version 3 [14], released in 2008, with the addition of skeletal muscle models to simulate occupant postural changes prior to a collision. Version 6 [15], released in 2019, incorporated the muscle models into Version 4.

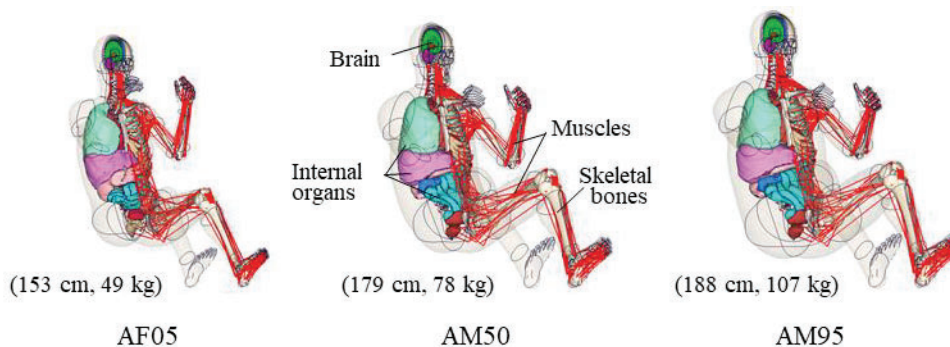


Figure 1. Overall view of human body FE models (THUMS Version 7).

Version 7 was developed based on Version 6 with significant improvements for injury simulation of occupants seated in a reclined position. One of the new features was the highly precise representation of the geometry and mechanical properties of the internal organs and lumbar spine. It was necessary to accurately reproduce the interaction between the pelvis and lap belt. Table 1 summarizes the modification items. The other features were the external geometry of the pelvis and abdomen, the physical properties of skin and adipose tissue, the structure of the small intestine and mesentery, and the characteristics of the intervertebral discs and ligaments of the spine. These new features contributed to accurate injury prediction. Modifications were also made to the regions other than the abdomen-pelvis. The detailed information is available in Appendix.

In the development work of Version 7, LS-DYNATM MPP971 R11.2.2 (Ansys, USA) was used to perform crash (dynamic loading) simulations. LS-DYNA is a general-purpose multi-physics simulation software package including a nonlinear explicit finite element solver.

Pelvis Model

The pelvis geometry was carefully reviewed to realistically reproduce submarining dependence on the seat reclining angle. Table 2 shows the measured mean \pm standard deviation [16] and the pelvis dimensions for three body sizes (AF05, AM50, AM95). Version 6 AM50 was generated based on the CT scan data of an actual person whose body size was close to the midsize male. AF05 was generated using the same procedure. AM95 was scaled from AM50. The overall height (h_{max}), width (w_{max}), and depth (d_{iliac}) of the THUMS pelvises were at most 40 mm smaller than the mean size. The smaller size pelvis could underestimate the engagement of the lap belt and pelvis in vehicle frontal collision. To enhance prediction for the average result before considering individual differences, the Version 7 pelvis models were modified to match the average dimensions.

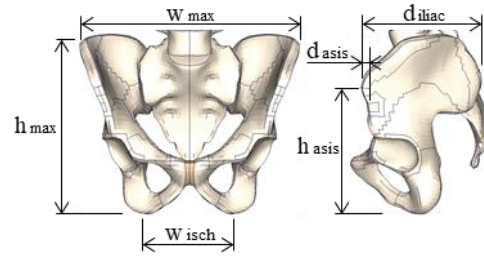
Table 1.
Model generation and modification.

Body Region	Simulation target	Model generation and modification	Reference
Pelvis	Submarining	Pelvis geometry	[16]
Abdomen		Abdominal skin geometry and property	[17-18]
		Adipose tissue property	[19]
	Abdominal injury	Small intestine and mesentery models	[20-23]
Lumbar spine	Lumbar spine fracture	Intervertebral disc property	[23-24]
		Ligament property	[25]
		Cortical bone thickness of vertebrae	[26-28]
Others	Improvements for simulation accuracy (Refer to Appendix)	Head dimensions	[42]
		Cortical bone thickness of ribs	[43]
		Heart model	[45]
		Long bone model	[23]

Table 2.
Pelvis geometry.

	AF05			AM50		
	Measurement (Hwang, 2016)	THUMS V6	THUMS V7	Measurement (Hwang, 2016)	THUMS V6	THUMS V7
Wmax [mm]	260 \pm 20	223 (-37)	259 (- 1)	282 \pm 20	244 (-38)	283 (+ 1)
Wisch [mm]	119 \pm 13	115 (- 4)	117 (- 2)	98 \pm 10	96 (- 2)	96 (- 2)
Hmax [mm]	191 \pm 11	184 (- 7)	190 (- 1)	220 \pm 12	200 (-20)	220 (0)
Hasis [mm]	136 \pm 10	139 (+ 3)	137 (+ 1)	152 \pm 10	146 (- 6)	151 (- 1)
Diliac [mm]	135 \pm 8	131 (- 4)	136 (+ 1)	148 \pm 11	133 (-15)	148 (0)
Dasis [mm]	11 \pm 4	11 (0)	11 (0)	10 \pm 5	4 (- 6)	10 (0)

	AM95		
	Measurement (Hwang, 2016)	THUMS V6	THUMS V7
Wmax [mm]	286 ±20	261 (-25)	285 (- 1)
Wisch [mm]	100 ±10	103 (+ 3)	101 (+ 1)
Hmax [mm]	226 ±12	214 (-12)	225 (- 1)
Hasis [mm]	155 ±10	156 (+ 1)	155 (0)
Diliac [mm]	151 ±11	142 (- 9)	151 (0)
Dasis [mm]	11 ±5	4 (- 7)	11 (0)



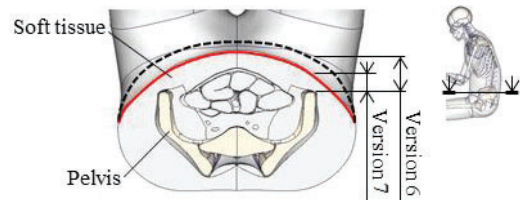
Abdominal Model

The geometry and mechanical properties of the soft tissues (skin, adipose) of the anterior abdomen were revised. The soft tissue on the anterior aspect of the Anterior Superior Iliac Spine (ASIS) of the pelvis greatly influences the interaction with the lap belt. Table 3 summarizes the mean numbers of soft tissue thickness for each body sizes [17] with a comparison of THUMS dimensions. The soft tissue thickness values of Version 6 AM50 and AM95 were larger than the mean numbers. In Version 7, these thickness values were modified to approach the mean numbers. During the mesh modification work, the quality of the solid elements was monitored so as not to be degraded (aspect ratio < 5). The modification reduced the discrepancy between the thickness values and the mean numbers to about ±10 mm. Figure 2 shows the tensile properties of the skin. The material model of the Version 6 skin assumed a linear elastic material. Compared to human skin data [18], the modulus was higher up to a strain of 0.5 and lower after that region. In Version 7, nonlinear characteristics were defined for the skin material in order to better represent the human skin tissue. Annaidi et al. (2013) [18] found that the mean modulus of elasticity of the skin depends on the orientation of the Langer line. The modulus in the vertical direction is lower than that in the parallel direction. When the lap belt loads the abdomen, the skin tissue is pulled in the direction perpendicular to the Langer line. The modulus of the skin properties in Version 7 was adjusted to the lower limit of the test data.

When the lap belt disengages from the pelvis, the adipose tissue in front of the iliac crest exhibits compressive and shear deformation modes simultaneously. Sun et al. (2021) [19] experimentally determined the compression and shear properties of the adipose tissue at three levels of strain rate (3, 13, and 50 s⁻¹). Figure 3 superimposes the average properties and corridors obtained from the tests and the compression and shear properties of the THUMS adipose tissue model. The Stress-Strain properties of the Version 7 material model (hyper-elastic) were set so that the properties in compression and shear at each strain rate were close to the average properties from the tests.

Table 3.
Abdominal skin geometry.

	Soft tissue thickness in front of ASIS [mm]		
	UMTRI	THUMS V6	THUMS V7
AF05	29	16 (-13)	16 (-13)
AM50	20	60 (+40)	19 (- 1)
AM95	35	90 (+55)	45 (+10)



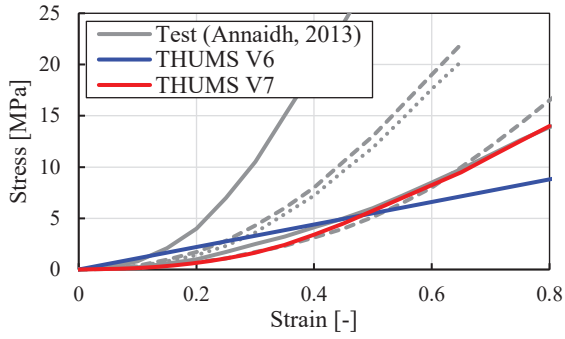
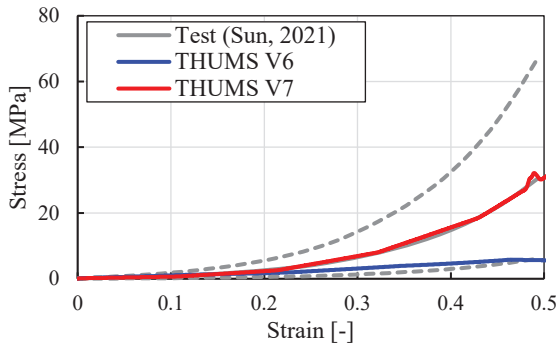
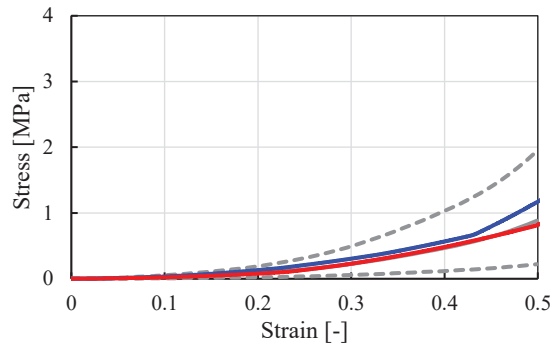


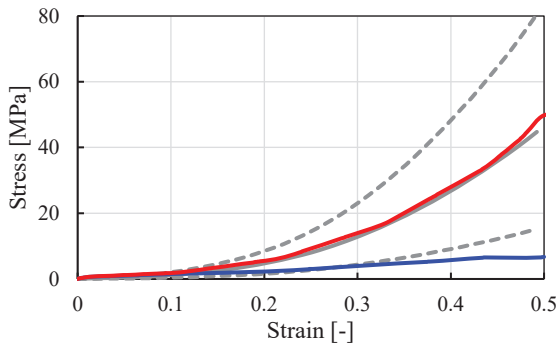
Figure 2. Abdominal skin property.



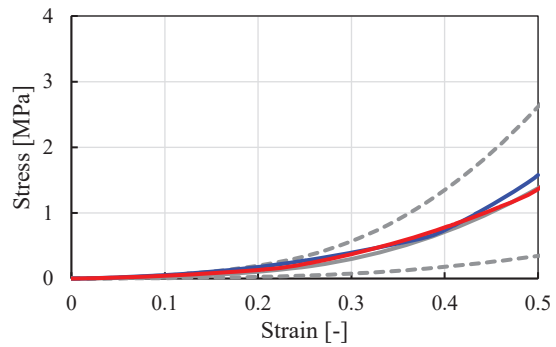
(a) Compression (strain rate: 3 s^{-1})



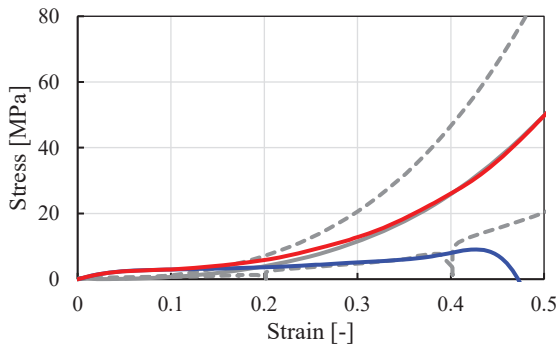
(d) Shear (strain rate: 3 s^{-1})



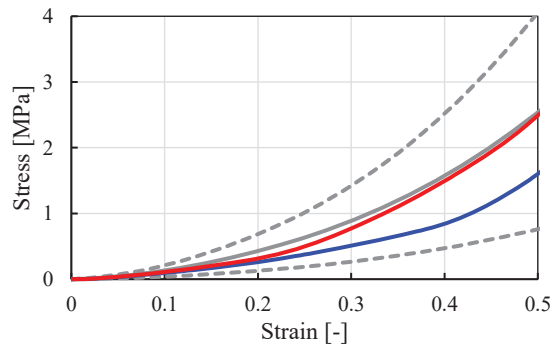
(b) Compression (strain rate: 13 s^{-1})



(e) Shear (strain rate: 13 s^{-1})



(c) Compression (strain rate: 50 s^{-1})



(f) Shear (strain rate: 50 s^{-1})

Figure 3. Adipose tissue property.

Small Intestine and Mesentery Model

In order to analyze injuries of the small intestine and mesentery, the anatomical structures and characteristics of the small intestine and mesentery were more accurately reproduced in Version 7. Figure 4 shows the small intestine models of Version 6 and Version 7. In Version 6 (as well as Version 4), the small intestine was represented as a simplified homogeneous structure which was different from the anatomic structure of the small intestine and mesentery. In Version 7, the long and folded intestinal geometry, mesentery, and intramesenteric vessels were precisely represented in the abdominal region [20]. In finite element modeling, shell elements were used to replicate the intestinal tract as a tubular part with a diameter of approximately 20 mm. The inside of the tube was filled with solid elements to mimic the contents. Based on tensile measurement data of the actual human tissue [21], a transverse anisotropic nonlinear elastic material with different properties in the axial and circumferential directions was defined for the intestinal part (Figure 5). For the solid part, the same material properties as the Version 4 small intestine model were used, assuming a foam material with nonlinear compressive properties. The mesenteric model was generated as a lattice mesh structure with contractible beam elements. Shell elements were added to fill the interstices of the mesh for contact calculations. The mesenteric vascular was also replicated by connecting beam elements using the nodes of the mesh forming the mesenteric model. Nonlinear elastic materials were defined for the mesenteric beam elements based on the tensile test data of the human gastric serosa [22]. Null material with no deformation resistance was applied to the shell elements in the mesenteric part for contact calculations. For the beam elements of the intramesenteric vessels, nonlinear elastic materials were defined based on the tensile test data of the human abdominal aorta [23].

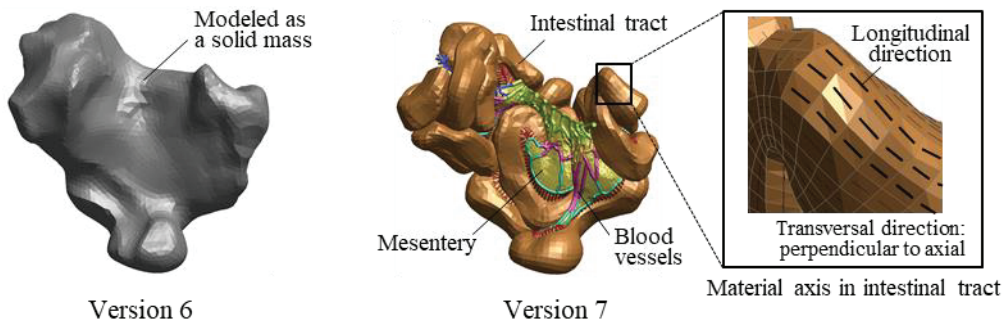


Figure 4. Small intestine model.

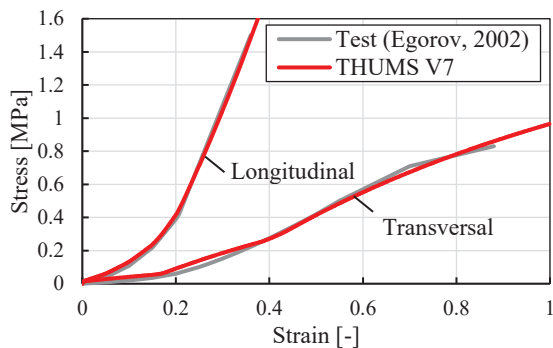


Figure 5. Tensile properties of intestinal tract.

Lumbar Spine Model

The lumbar spine part was also updated in Version 7. The mechanical properties of the intervertebral disc and the ligaments around the spine were carefully reviewed. A nonlinear foam material was defined for the intervertebral discs based on the quasi-static (strain rate: 0.01s^{-1}) compression test data [23] of the actual human tissue. Kemper et al. (2013) [24] identified the relationship between strain rate and disc stiffness (Equation (1)). Based on the relationship, the rate of increase in stiffness at strain rates of 5.3, 12.1, and 73.7 s^{-1} were calculated. The intervertebral disc properties in Version 7 were determined by scaling the stress-strain characteristics of the quasi-static compression (Figure 6).

$$k = 57.328 \dot{\varepsilon} + 2019.1 \quad \text{Equation (1)}$$

k : Stiffness (N/mm), $\dot{\varepsilon}$: Strain rate (s^{-1})

There are multiple ligaments attached around the spine. Those ligaments contribute to the mechanical properties of the spine. In Version 6, linear elastic properties were assumed for the ligaments. In Version 7, nonlinear elastic properties were adopted in order to more accurately simulate the tensile properties of actual ligaments [25]. The nonlinear properties were approximated by three straight lines (Figure 7). For the Intertransverse ligament (ITL) and Facet capsular ligament (CL), for which no reference data are available, the average numbers of Anterior longitudinal ligament (ALL), Interspinous ligament (ISL), Supraspinous ligament (SSL), Posterior longitudinal ligament (PLL) and Ligamentum flavum (LF) were defined for the property.

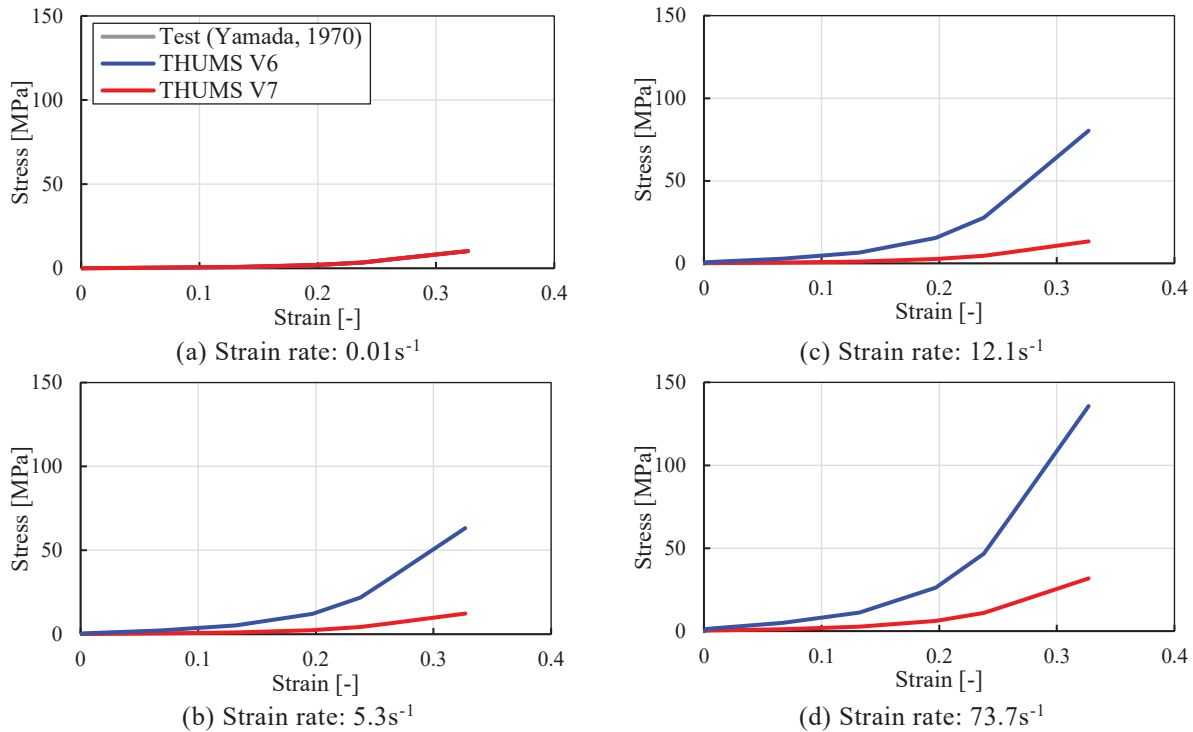


Figure 6. Intervertebral disc property.

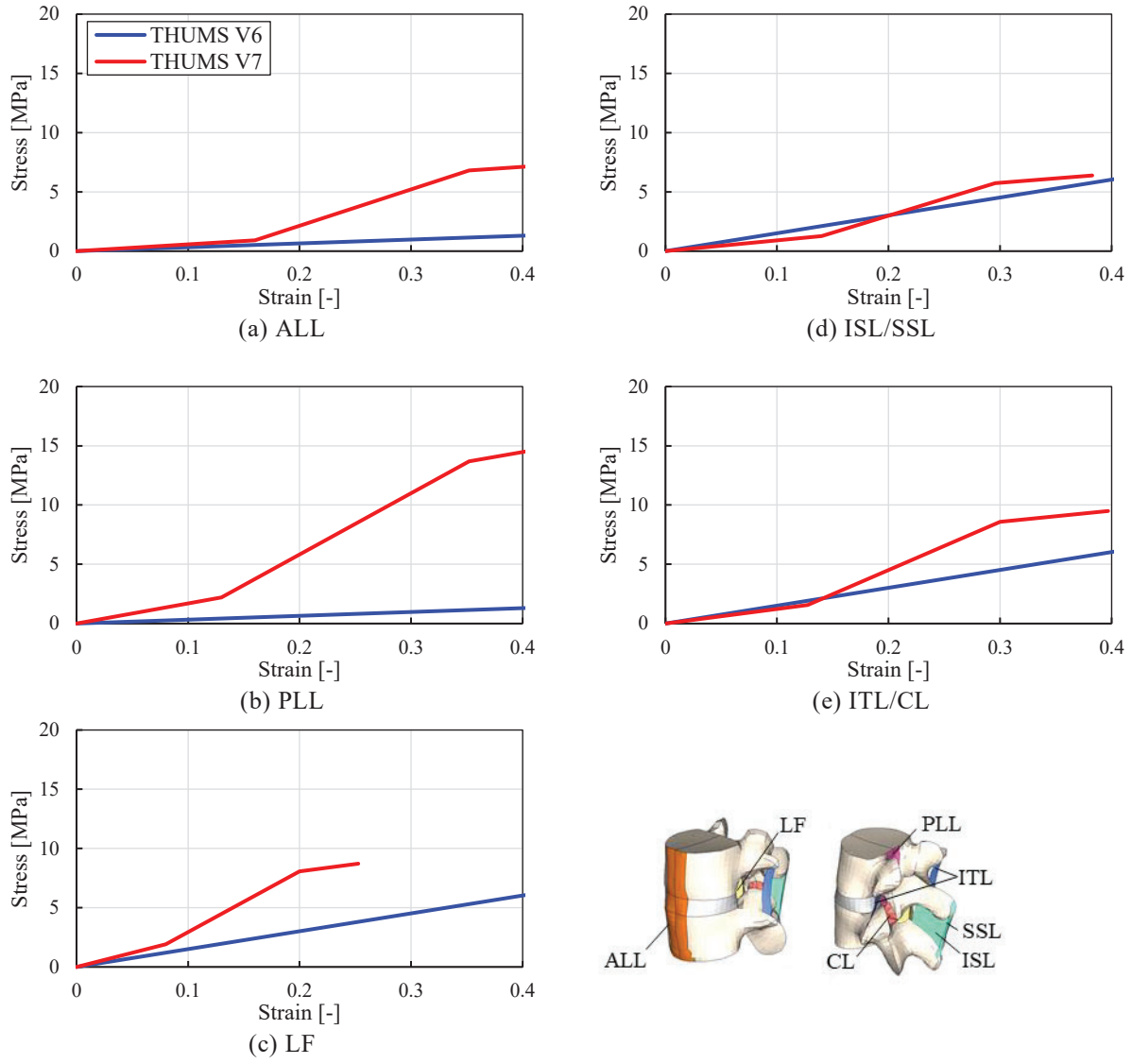


Figure 7. Ligament property

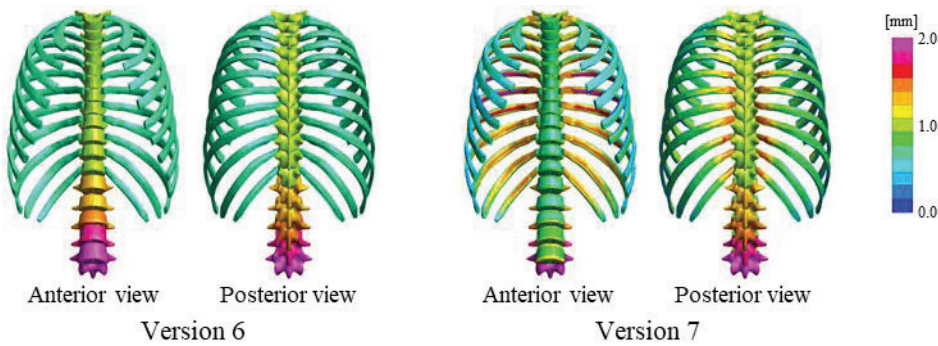


Figure 8. Cortical bone thickness distribution of vertebrae.

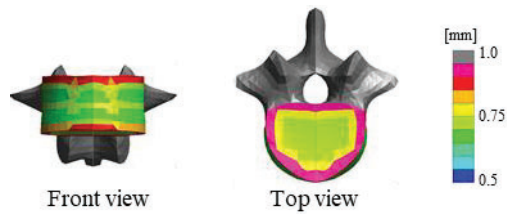


Figure 9. Cortical bone thickness distribution of L1 vertebra.

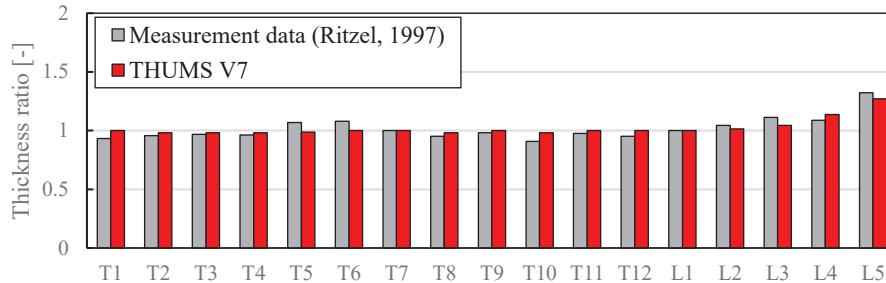


Figure 10. Ratio of cortical bone thickness to L1 vertebra.

In Version 6, a uniform thickness was assumed for the cortical bone of all vertebrae. In Version 7, uneven distribution of thickness was incorporated into the cortical bone of each vertebra (Figure 8). The realistic thickness distribution contributes to accurate prediction of vertebral fractures. First, the thickness distributions of the lateral and vertical walls of the vertebral bodies were determined based on the measurement data of the actual human L1 [26-27]. For the areas other than the vertebral body, such as the vertebral arch and spinous process, the cortical bone thickness was assumed to be uniform. The same thickness values as Version 6 were used for Version 7 (Figure 9). For the other vertebrae in the lumbar spine and thoracic spine, the cortical bone thickness of each vertebra was determined by calculating the thickness ratio of each vertebra to that of L1, based on the measured data of the cortical bone thickness of the front surface of the vertebra [28] (Figure 10). The thickness distribution of the cortical bone from T1 to L1 was assumed to be the same. The thickness of the cortical bone of L5 was assumed to be 1.27 times greater than that of L1. It was assumed that the thickness gradually increased from L1 to L5. The thickness of the cervical spine was not changed from Version 6.

MODEL VALIDATION

The validity of the mechanical responses of THUMS Version 7 were examined by comparing with PMHS tests described in the literature. The results were also compared with Version 6 results to confirm the effects of the model modifications. First, the model was validated for each component unit of the abdomen and lumbar region, and then the whole-body kinematics were verified under vehicle frontal impact conditions. In the component validation for the pelvis and abdomen, both ends of the lap belt were towed backward to replicate a sliding motion on a reclined occupant in a vehicle frontal collision. The load response characteristics were also examined under other conditions. The mechanical properties of the Functional Spine Unit (FSU) and the entire lumbar spine from L1 to L5, were validated in the combined loading of bending and shear. Finally, using a whole-body model seated in a reclining posture, the impact kinematics was examined by monitoring the displacement and trajectory of target points on the body. The impact condition assumed a vehicle frontal collision. The THUMS results were compared with the PMHS test data reported in the literature. Table 4 summarizes the validation cases.

Table 4.
Model validation cases.

Body Region	Model validation	Reference	
Component	Pelvis	Interaction between pelvis and lap belt	[29]
	Abdomen	Load response of abdomen	[30-34]
		Abdominal organ injuries	[30-34]
	Lumbar spine	Characteristics of lumbar spine [FSU]	[35-36]
		Characteristics of lumbar spine [L1-L5]	[37]
		Lumbar spine fractures	[38]
	Others (Refer to Appendix)	Rib fractures	[44]
		Load response of heart	-
Bending stiffness of long bone		[23]	
Whole-body	Kinematics during frontal collision in forward-facing reclined seating	[3,39]	

Component Validation

Interaction between pelvis and lap belt Richardson et al. (2021) [29] conducted PMHS tests to monitor the lap belt motion and load response when the engagement with the pelvis was lost and the lap belt slid up causing the submarining. Figure 11 shows a schematic view of the simulation model. The subject was an adult male with a height of 183 cm and a weight of 104 kg. The THUMS AM95 model (188 cm, 107 kg) was selected for comparison. The thoracic, lumbar, and sacral vertebrae were rigidly connected to the support column, which was reclined 45 degrees from the vertical as support conditions equivalent to those in the test. Both legs were supported to make the femur angle inclined by approximately 15 degrees from the horizontal line. The lap belt was draped over ASIS and Anterior Inferior Iliac Spine (AIIS) and was adjusted so that the angle between the ASIS-AIIS line and the lap belt became 74 degrees which was the average in the tests. Both ends of the lap belt were connected to steel cables and pulled rearward with a prescribed displacement of approximately 140 mm (Figure 12).

Figure 13 shows the trajectory of the center of the lap belt calculated from the simulation using Version 7. It was close to the trajectory measured in the test. Figure 14 shows the lap belt tension vs. X displacement diagram of the center of the belt. Version 6 generated a higher load by 2 kN compared to the test data. The calculated load in Version 7 was closer to the test data. In addition, the load-displacement characteristics after the disengagement of the lap belt in Version 7 were closer to those of the tests compared to Version 6.

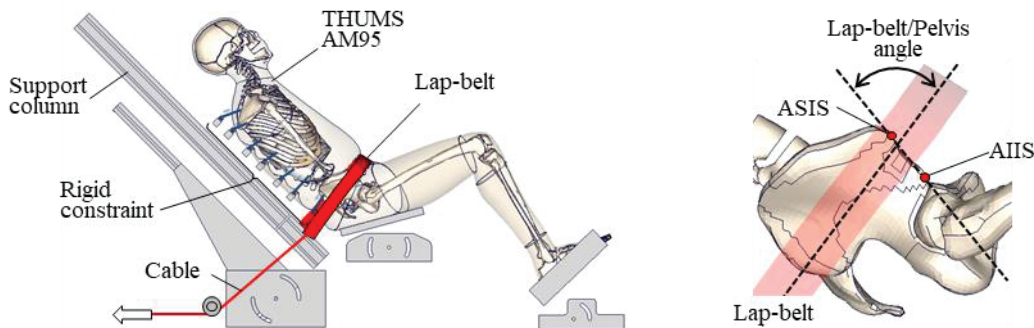


Figure 11. Simulation model of lap belt loading to pelvis.

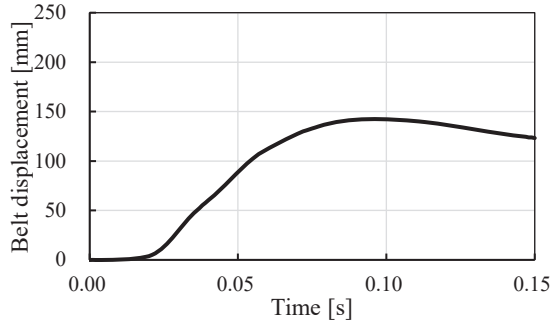


Figure 12. Lap belt displacement pulse.

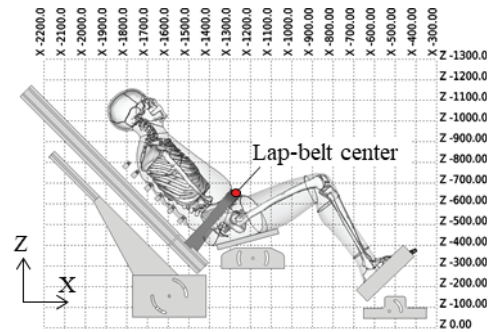
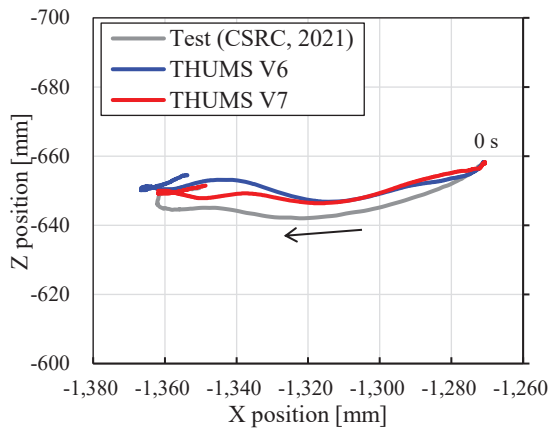


Figure 13. Trajectories of center point of lap belt.

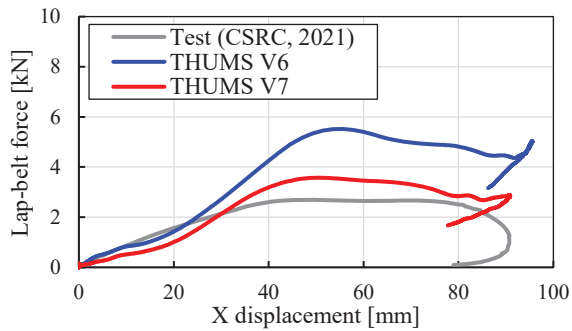


Figure 14. Lap belt force vs. X displacement curves.

Load response of abdomen

The validation for the abdominal model was conducted by applying compressive load under various conditions. Table 5 summarizes the loading conditions. Figure 15 shows a schematic view of the simulation models. A total of six cases were simulated: three cases with rigid impactors (Cases-i1, i2, i3) [30-32] and another three cases with seat belts (Cases-b1, b2, b3) [32-34]. The loading conditions in the simulation models, such as impactor geometry, mass, initial velocity and belt position, and velocity history were set to be equivalent to those in the tests. In each case, the THUMS model was selected whose body size was close to the average of the test subjects. The AF05 model was used in Case-b1, while the AM50 model was used in the other cases.

Figures 16 (a)-(c) show the results of the load-deflection diagrams under the impactor loading conditions. In Case-i1, the load output from Version 7 was within the test corridor from the start of loading up to a deflection of 100 mm.

After that, the Version 7 load slightly exceeded the upper boundary of the corridor. In Case-i2 and Case-i3, the loads output from Version 7 were within the variability of the test results over almost the entire range of loads applied. Figures 16 (d)-(f) show the results of the load-deflection (Case-b2: lap belt displacement) diagram under the belt loading conditions. In Case-b1, the maximum load value and the deflection at that time output from Version 7 were within the test corridor. The Version 7 load was partially below the lower boundary of the test corridor in the deflection range below 50 mm. In Case-b2, the maximum load value output from Version 7 was close to the test results. The calculated load-deflection diagram up to the maximum peak was lower than the test results. In Case-b3, the maximum load value, the deflection at that time and the curve after turning to unloading output from Version 7 were within the test corridor. The initial load rise at the deflection range below 10 mm was higher than the upper boundary of the test corridor.

Table 5.
Validation cases of abdominal loading.

Case No.	Load type	Load conditions (speed, mass)	THUMS physique	Reference
Case-i1	Rigid-bar impact	6.1m/s, 32kg	AM50	[30]
Case-i2	Rigid-steering impact	10m/s, 18kg	AM50	[31]
Case-i3	Rigid-bar impact	9.0m/s, 48kg	AM50	[32]
Case-b1	Seatbelt loading	3.0m/s, -	AF05	[32]
Case-b2	Seatbelt loading (lap & shoulder)	3.0m/s, -	AM50	[33]
Case-b3	Seatbelt loading	6.9m/s, -	AM50	[34]

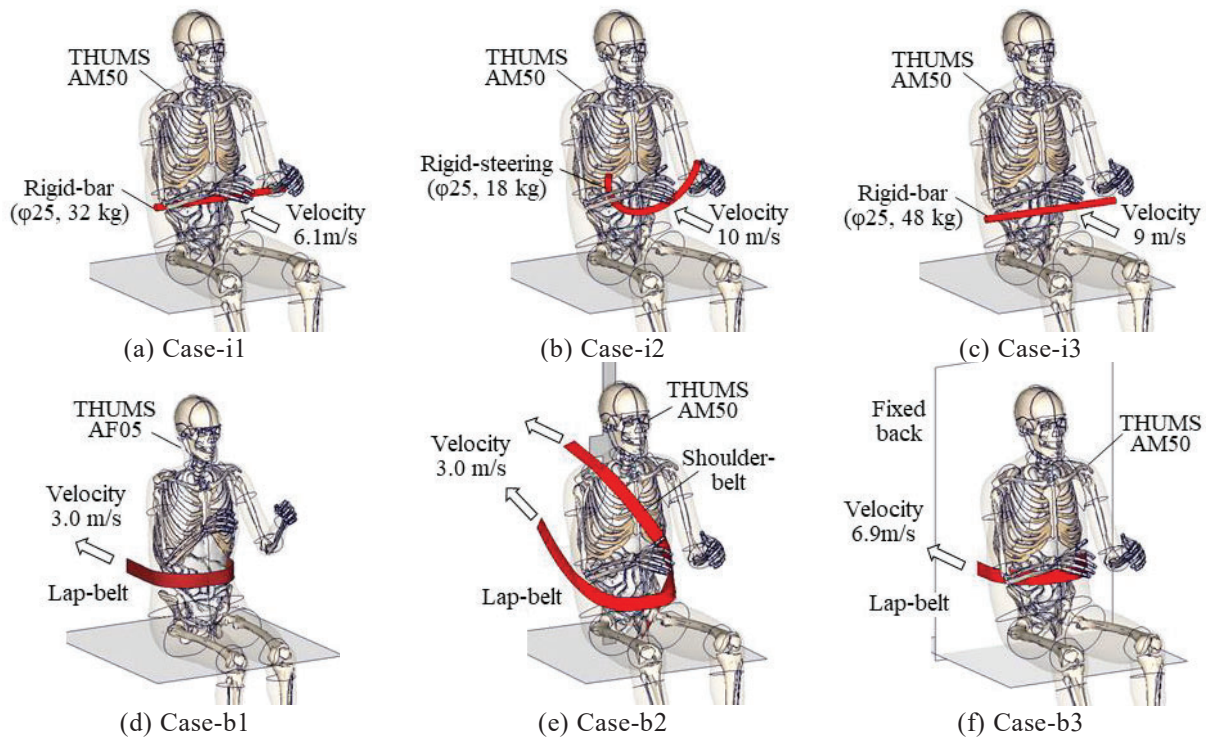


Figure 15. Simulation models of abdominal loading.

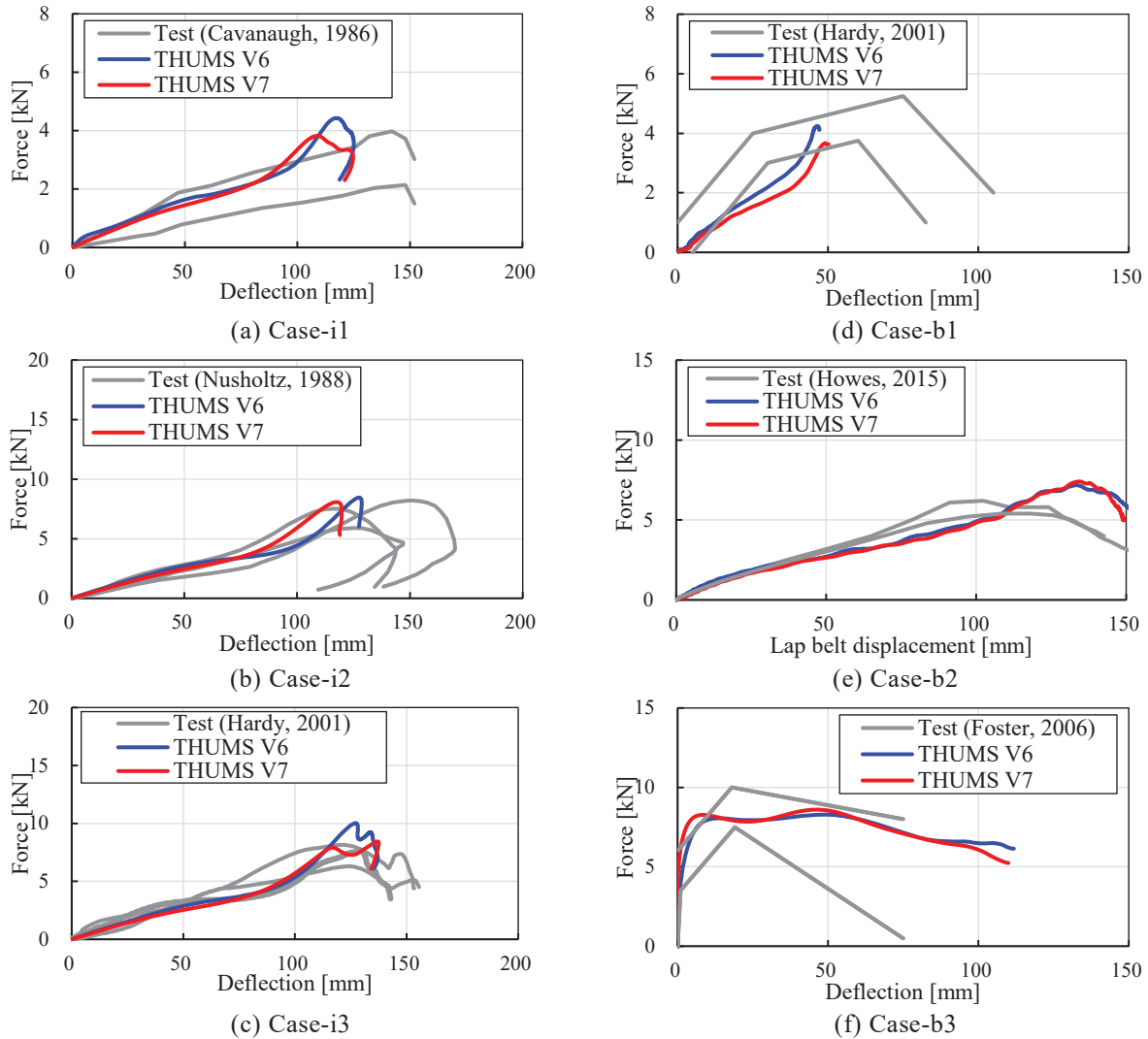


Figure 16. Impactor and belt force vs. abdominal deflection curves.

Abdominal organ injuries

The mechanical properties of the abdominal part were validated in six loading cases. Table 6 summarizes the maximum strain values calculated in the shell and beam elements of the intestinal tract, mesentery, and mesenteric vessels. Table 6 also shows the measured values of the rupture strain obtained from tensile tests of the intestinal tract [21], mesentery [22], and vessels [23]. The amounts of energy applied to the abdomen are also shown in the same table. In this validation, the rupture strain values of the intestine in the axial and circumferential directions were tentatively assumed to be 0.37 and 0.88, respectively. The maximum strain values calculated from the intestine model were lower than the thresholds in all cases. In the simulations, the calculated strain value was lowest in Case-b2, while intestinal rupture occurred in both axial and circumferential directions in the test corresponding to Case-b2. The calculated strain values of the mesenteric exceeded the threshold in all cases. On the other hand, the mesentery was not damaged in all test cases. The calculated strain value of the vascular was highest in Case-i2. There was no description of vascular injury in the literature.

Table 6.
Maximum strain of intestinal tract, mesentery and blood vessel.

Case No.	Maximum strain [-]				Loaded energy [J]
	Intestinal tract		Mesentery	Blood vessel	
	Longitudinal	Transversal			
Threshold (Rupture strain)	0.37	0.88	0.44	0.94	-
Case-i1	0.36	0.56	1.00	0.72	234
Case-i2	0.35	0.73	1.10	0.98	395
Case-i3	0.36	0.64	1.37	0.96	530
Case-b1	0.33	0.73	0.70	0.64	80
Case-b2	0.32	0.73	0.91	0.70	567
Case-b3	0.36	0.56	1.09	0.85	846

Characteristics of lumbar spine [FSU] The mechanical properties of the lumbar spine model were examined. First, the compressive and shear/bending properties of the FSU were checked, then the shear and bending properties of the entire lumbar spine were verified.

Arun et al. (2017) [35] performed a compression test to the FSU of L1-L2. A simulation model was generated to reproduce the test. The upper and lower vertebrae were potted to the cups so that the neutral plane of the disc was perpendicular to the direction of compression. The lower potting cup was restrained and the upper one was compressed with a downward velocity of 1.0 m/s. The load-displacement characteristics were compared between the test and simulation (Figure 17(a)). Belwadi et al. (2008) [36] performed a test on T12-L2 applying a combined load of shear and bending. The upper vertebrae were potted and restrained at a position where the center of gravity of the lower vertebrae coincided with the center of the lower potting cup and the top of the upper vertebral end plate was parallel to the top of the lower potting cup. The lower potting cup was restrained and the upper one was loaded with a displacement of 4 mm/s in the horizontal forward direction and a rotation of 0.061 rad/s in the forward flexion direction simultaneously. Another simulation model was generated to reproduce the test (Figure 17(b)). The calculated load-displacement and moment-angle characteristics were compared to those measured in the test. Figure 18(a) shows the load-displacement diagram in compression. Figures 18(b-1) and (b-2) show the shear load-shear displacement and forward bending moment-deformation angle diagrams in flexural shear. The load-displacement curve calculated by Version 7 was within the test corridor while that by Version 6 was higher than the upper boundary. The stiffness in shear and flexion output from Version 7 was also lower than in that from Version 6. The shear load, displacement, moment and angle, calculated by Version 7, at the timing of fracture prediction (cortical bone plastic strain $\geq 2\%$) were within the variation of the test data.

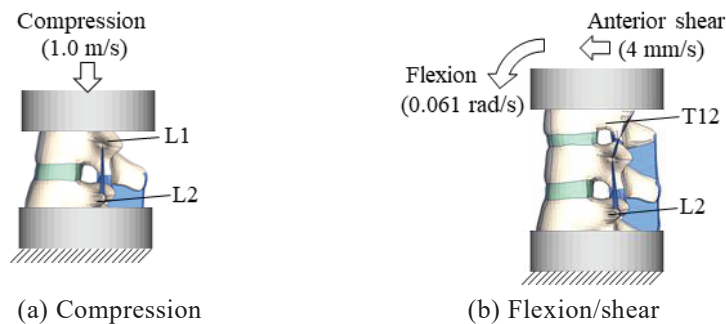
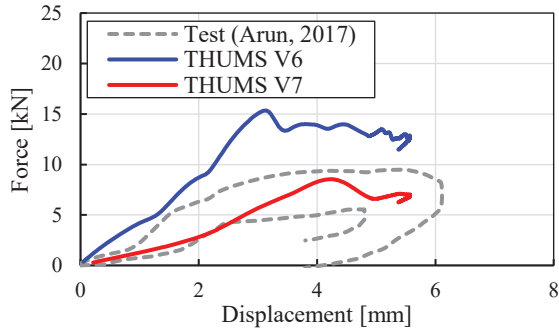
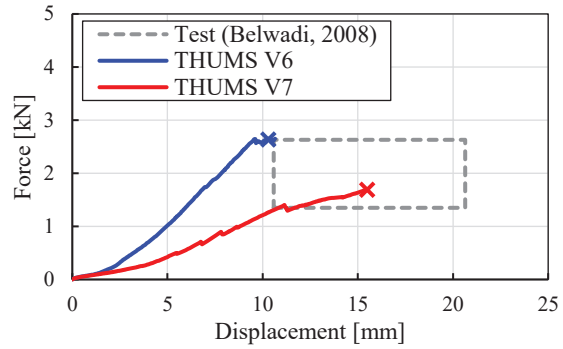


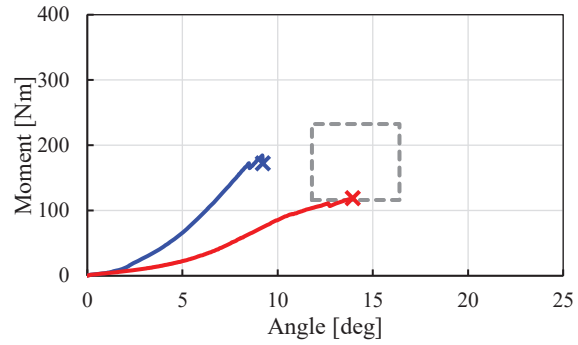
Figure 17. Simulation models of FSU loading.



(a) Compression force - displacement



(b-1) Anterior shear force – displacement



(b-2) Flexion moment - angle

Figure 18. Compressive force vs. displacement (a) and anterior shear force vs. displacement, flexion moment vs. angle curves (b-1, b-2).

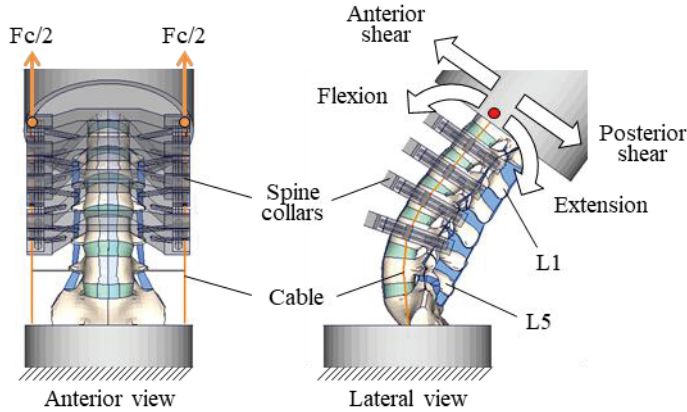


Figure 19. Simulation model of lumbar spine loading.

Table 7. Validation cases of lumbar spine loading.

Direction	Compression load		
	0 N	900 N	1800 N
Flexion	Case-fl0	Case-fl9	Case-fl18
Extension	Case-ex0	Case-ex9	Case-ex18
Anterior shear	Case-as0	Case-as9	Case-as18
Posterior shear	Case-ps0	Case-ps9	Case-ps18

Characteristics of lumbar spine [L1-L5] The mechanical properties of the entire lumbar spine model were verified. Chastain et al. (2021) [37] conducted a bending and shear test to the lumbar spine from T12 to S1. The section was cut from T12 to S1, and soft tissues other than the posterior ligament tissue were excluded. T12 and S1 were potted in a cup and the potting cup on the S1 side was completely restrained. Collars (with a beacon marker for kinematics measurement and a mechanism for adjusting the anterior-posterior position of the cable) were attached to L1 to L4 as in the test. The cables were pulled through both sides of the collars, and a compressive load was applied in the axial direction of the lumbar spine. Bending (flexion/extension) and shear (anterior/posterior) characteristics were investigated at compressive loads of 0, 900, and 1800 N, respectively. The loading rates in bending and shear were 3 deg/s and 50 N/s. The upper potting cup was operated in such a way that the change in compression load and shear load was zero in the bending test and zero in the shear test. Displacements and angles were measured in the upper potting cup, and loads and moments were measured in a section set horizontally in the lower potting cup. A simulation model was generated to reproduce the test. Figure 19 shows a schematic view of the simulation model. Table 7 summarizes the simulation cases. Figure 20 shows the calculated the moment-angle curves in flexion and extension. The simulation results in the flexion cases (Case-fl series) slightly exceeded the upper limit of the test corridors in the region above about 20 degrees. The calculated flexion properties and moment-angle characteristics in the extension cases (Case-ex series) were generally within the test corridors.

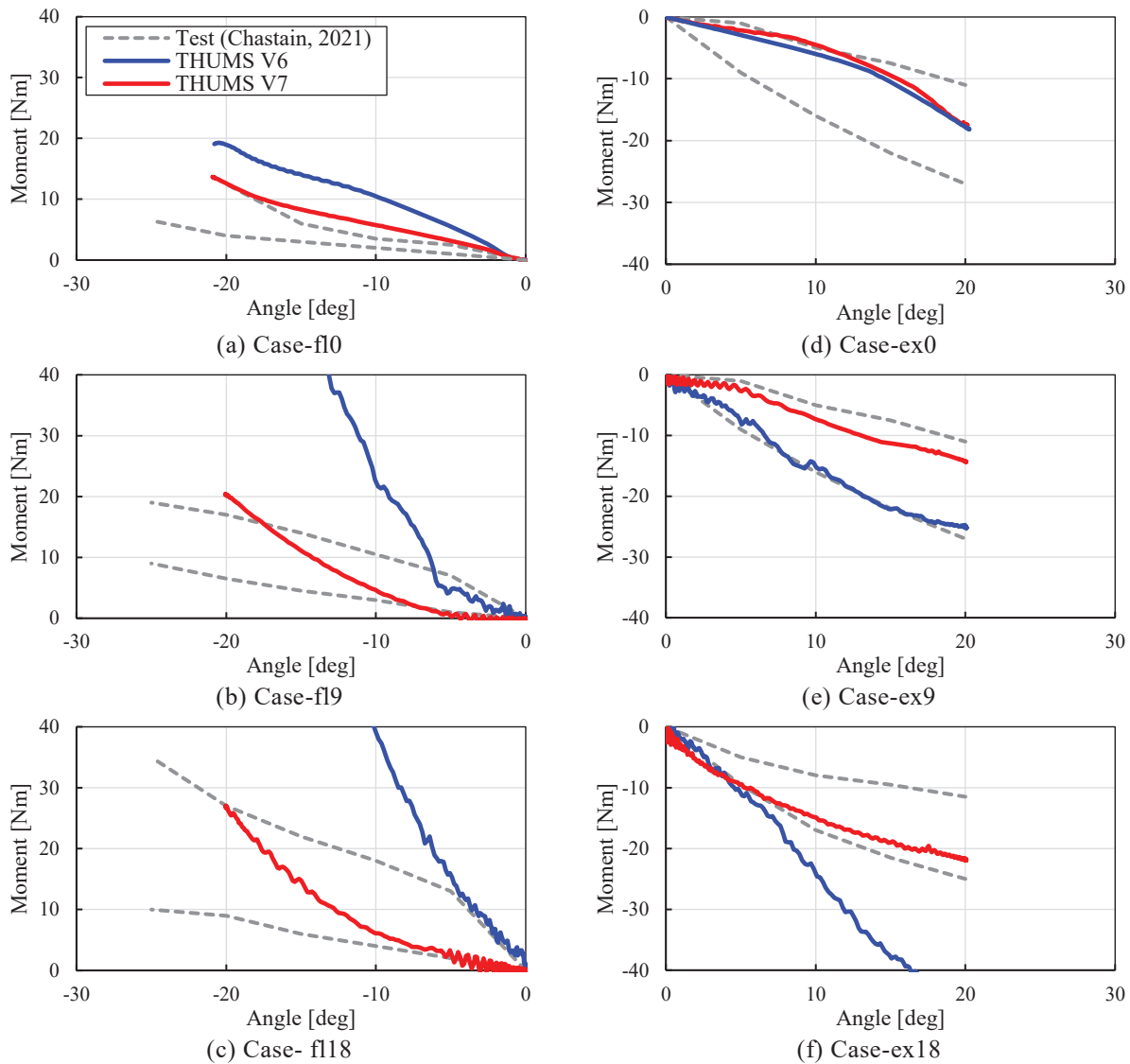


Figure 20. Flexion and extension moment vs. angle curves.

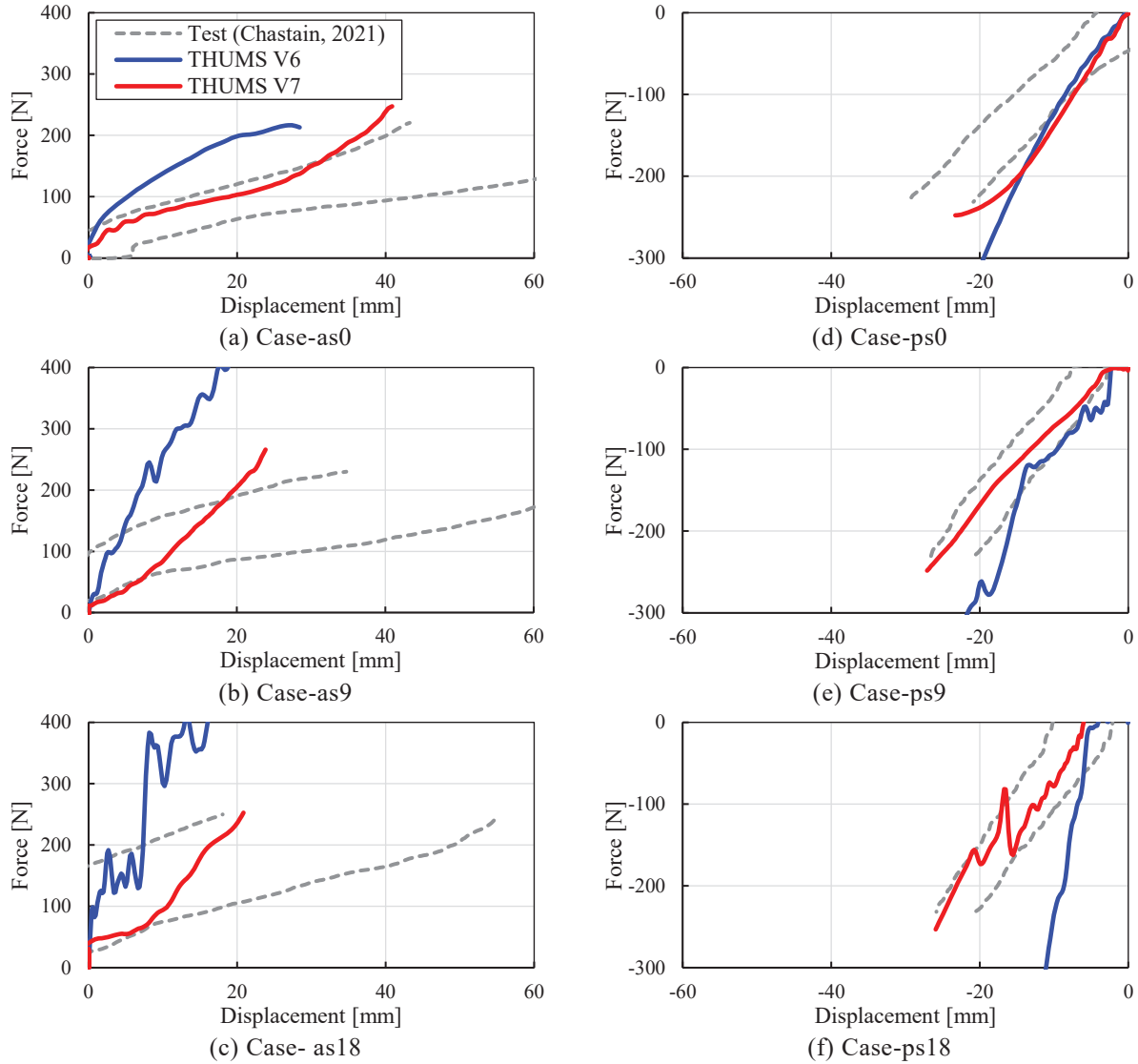


Figure 21. Anterior and Posterior shear force vs. shear displacement curves.

Figure 21 shows the shear load-displacement characteristics in anterior and posterior shear. The simulation results in the anterior shear cases (Case-as series) were higher than the upper boundary of test corridors for the displacement range of 20~30 mm. The calculated curves for the other range remained within the test corridors. The calculated shear load-displacement characteristics in the posterior shear cases (Case-ps series) were almost fully within the test corridors.

Lumbar spine fractures The prediction accuracy of vertebral fracture under combined compression and bending loading conditions was examined. Tushak et al. (2022) [38] conducted a test applying compression and flexion to FSU. Two FSU segments, upper (T12-L2) and lower (L3-L5), were extracted and the upper and lower vertebrae were fixed with potting cups. Compressive loads (three cases: 2200, 3300, and 4500 N) were applied quasi-statically to the lower potting cup, and then the upper potting cup was flexed forward at an angular velocity of 10.47 rad/s to apply bending loads. Simulation models were generated to reproduce the tests (Figure 22). Table 8 summarizes the calculation cases. The calculated loads and moments at which vertebral fractures were predicted by the simulation model were compared with the test results. It was assumed that fracture occurred when the plastic strain of the cortical bone exceeded 2%. Figures 23 (a) and (b) compare the load and moment at fracture in the upper and lower segments

of lumbar spine between the simulation and the test. In Version 6, the calculated moment in the lower segment was higher than the test variation range. In Version 7, the calculated moment was close to the upper boundary of the test variation. The magnitude of load and moment at fracture prediction was within the test variation for both the upper and lower segments.

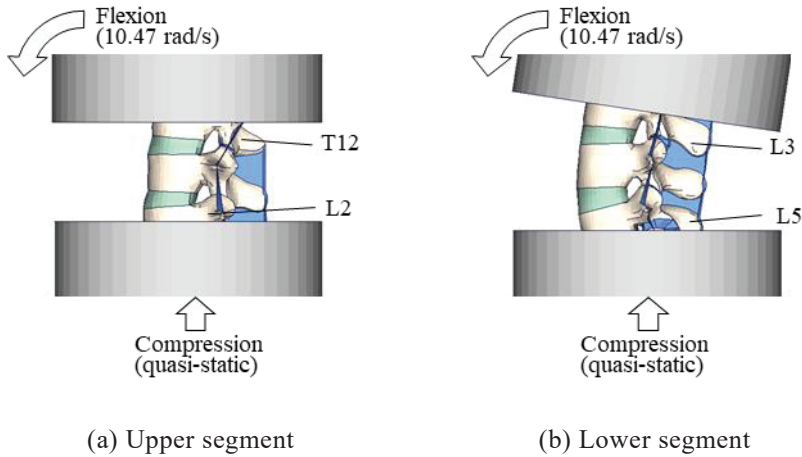


Figure 22. Simulation models of FSU loading to validate vertebral fracture.

Table 8.
Validation cases of FSU loading to validate vertebral fracture.

Segment	Compression load		
	2200 N	3300 N	4500 N
Upper	Case-u22	Case-u33	Case-u45
Lower	Case-l22	Case-l33	Case-l45

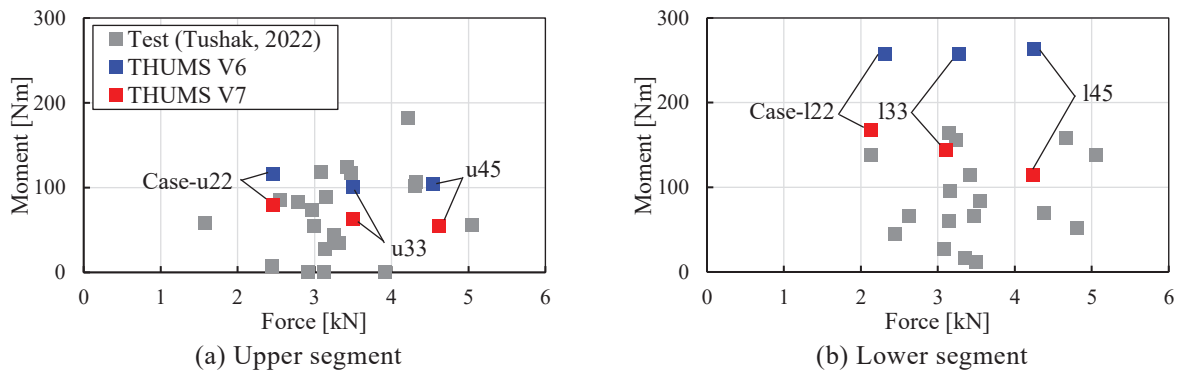


Figure 23. Flexional moments and compressive loads at vertebral fracture.

Whole-Body Validation

Frontal collision in forward-facing seating

Reed et al. (2019) [3] conducted a frontal impact sled test with PMHS seated in a reclining position. The seatback angle was set to 45deg. At the time of writing this manuscript, the test results at 32 kph were available in the NHTSA Database [39]. This test was used for the validation. Figure 24 illustrates the simulation model with Version 7 to reproduce the test for validation purpose. Figure 25 shows the time history waveforms of sled G pulse. The average height and weight of the three PMHS used in the test were 174 cm and 70 kg, respectively. THUMS AM50 model (179 cm, 78 kg), which was close to the subject body size, was selected for the simulation. The measured coordinate values of each part of the three PMHS were used as the reference. The initial posture of THUMS was adjusted by the following procedure. The pelvic angle was adjusted so that the angle of the line connecting hip-point and the center of the intervertebral disc between L5 and S1 became 68.4deg which was the average measured value in the tests. The spinal alignment was adjusted so that the coordinates of the head, T1, T8, T12, and L4 stayed within the range of test variation. The simulation model replicated the spring-controlled semi-rigid seat used in the PMHS test [40]. The seat pan (seat rear) angle, anti-submarine ramp (seat front) angle and spring characteristics were set to the values in the test. The relative position between the ASIS and lap belt was arranged to match the measurement values in the test.

Figure 26 compares the impact kinematics of PMHS and Version 7 in lateral view. Both PMHS and THUMS showed forward motions with the upper body bending forward and the pelvis tilting backward. In both PMHS and THUMS, the engagement between the lap belt and pelvis was maintained until the end of the impact. Figure 27 compares the trajectories of each measurement point in PMHS and THUMS. Figure 28 compares the displacement history of each part in the X and Z directions (average of three tests). For all measurement points, the trajectories of Version 7 were almost entirely within the variation range of the PMHS tests. The displacement histories for each of the THUMS sections were close to the average history of the PMHS.

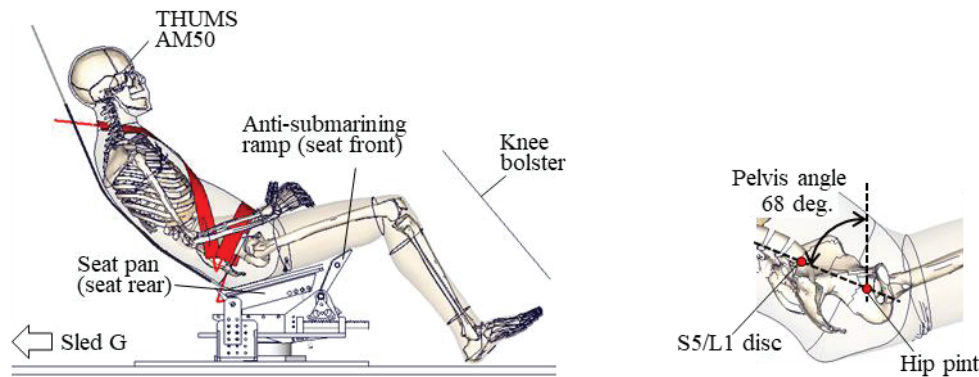


Figure 24. Simulation model of frontal sled test in reclined posture.

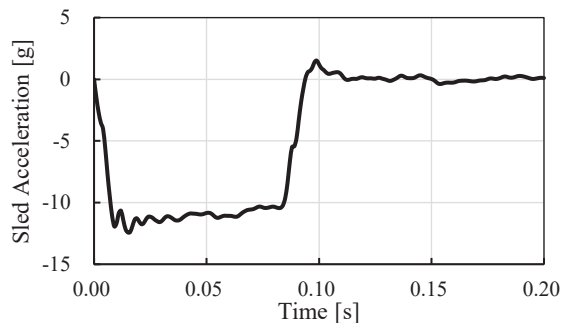


Figure 25. Sled G pulse (delta V: 32 kph).

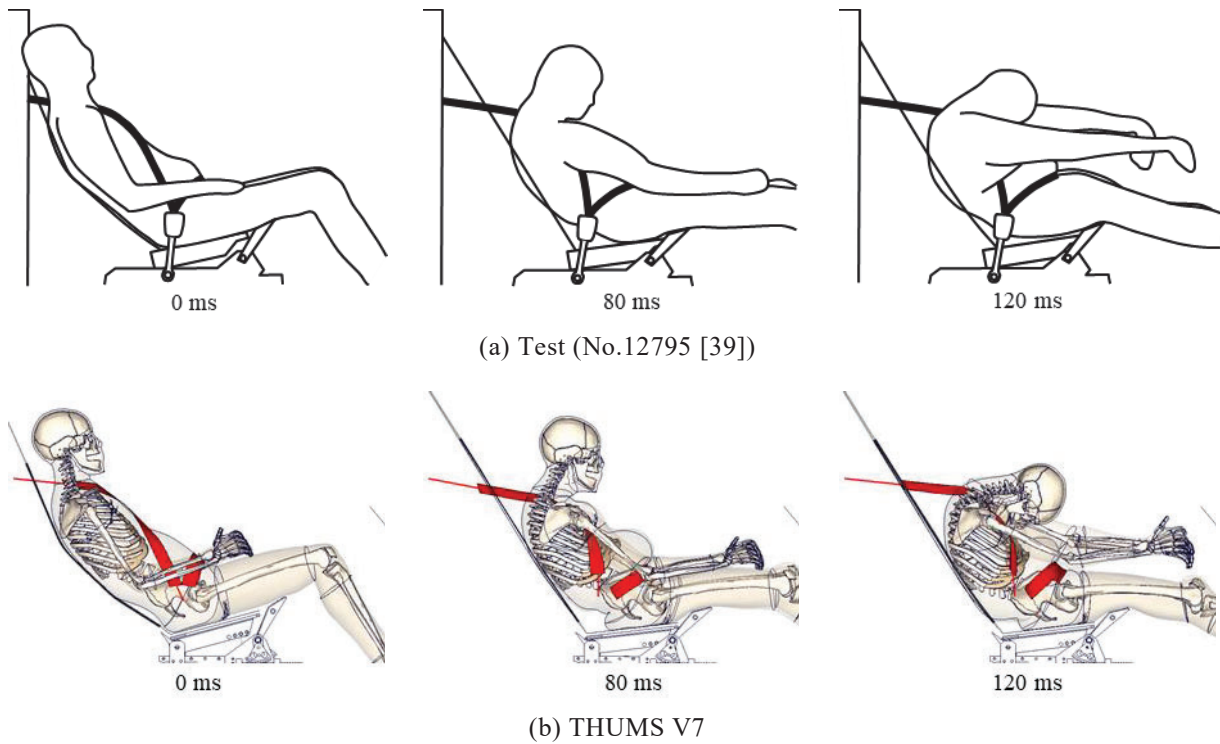


Figure 26. Kinematics of occupant.

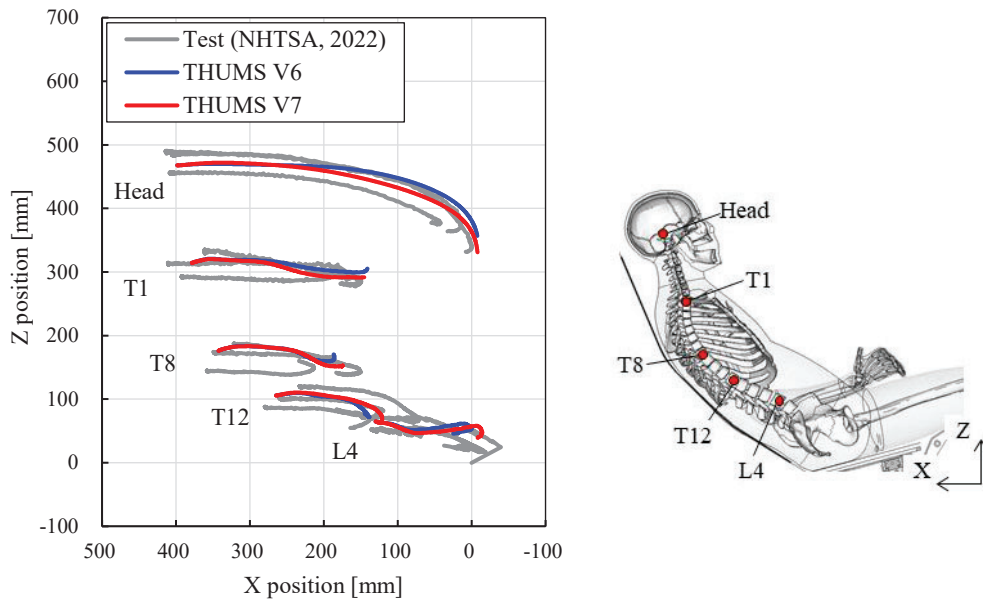


Figure 27. Trajectories of each measurement point of occupant.

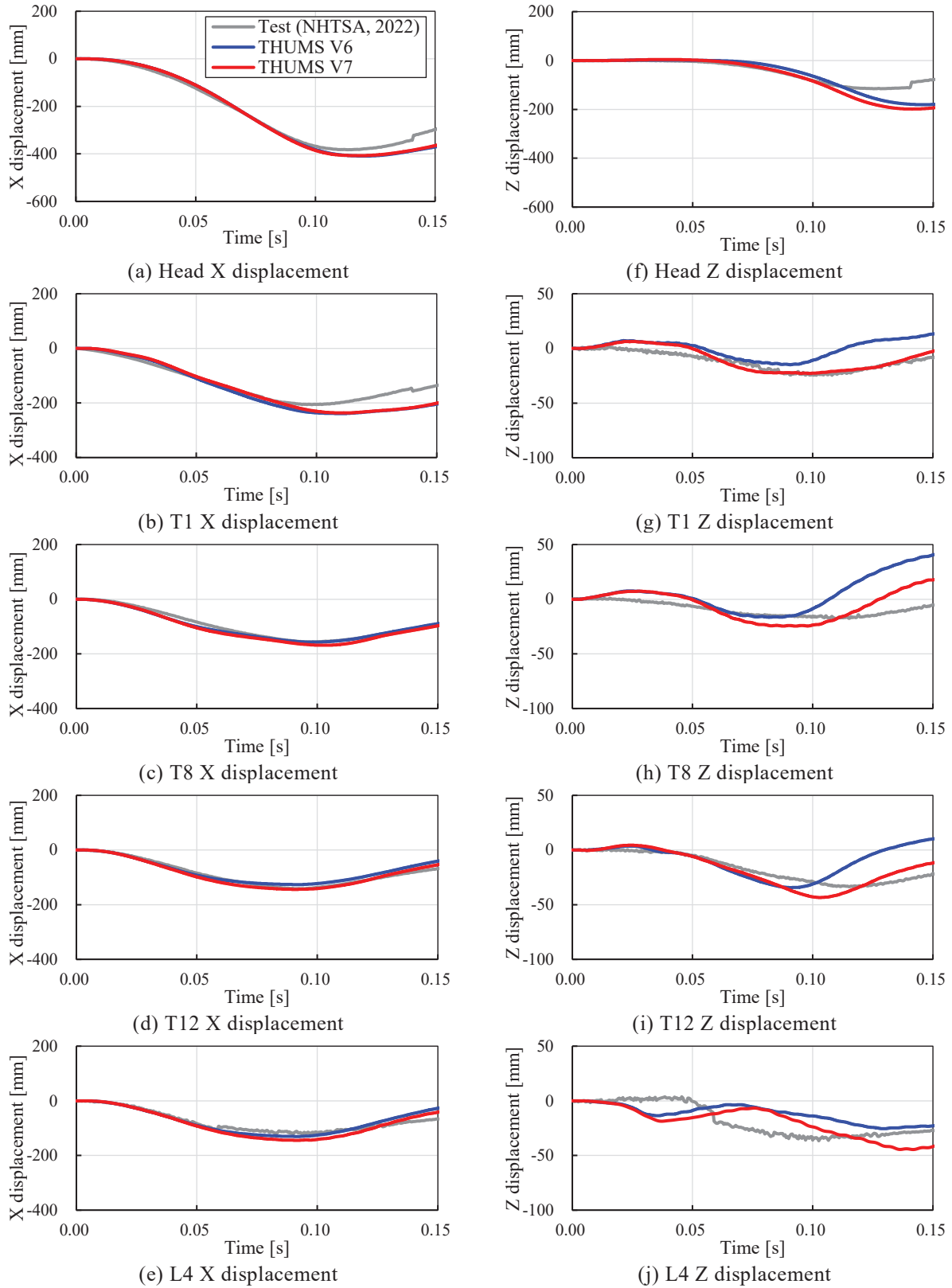


Figure 28. Displacement time histories of each measurement point.

The ISO rating specified in ISO/TS 18571 [41] was calculated to quantitatively evaluate the agreement of two time history curves. The closer the ISO rating value is to 1, the higher the degree of conformity. Table 9 shows the evaluation results. Regarding the Z displacements at each measurement point, the ISO rating values of Version 7 were higher than those of Version 6. As a result, the average rating value was approximately 0.1 higher in Version 7. The seat (Fr, Rr) reaction forces and seatbelt (shoulder, lap) loads for each displacement history were also close to the test load levels (Figure 29).

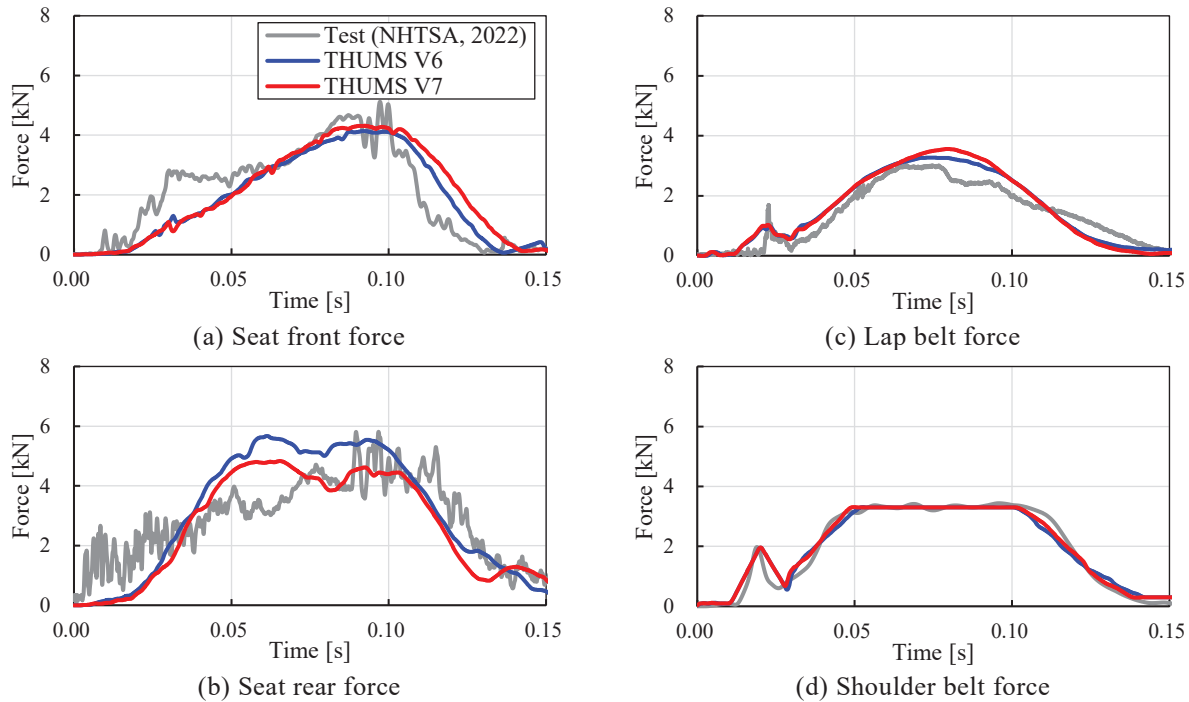


Figure 29. Time history of seat reaction forces and belt forces.

Table 9.
Evaluated values (ISO ratings) of the match with the test curves.

Displacement		THUMS V6		THUMS V7	
		ISO rating	Grade	ISO rating	Grade
Head	X	0.91	Good	0.92	Good
	Z	0.66	Fair	0.66	Fair
T1	X	0.78	Fair	0.78	Fair
	Z	0.28	Poor	0.73	Fair
T8	X	0.94	Excellent	0.92	Good
	Z	0.36	Poor	0.42	Poor
T12	X	0.83	Good	0.92	Good
	Z	0.36	Poor	0.70	Fair
L4	X	0.78	Fair	0.79	Fair
	Z	0.29	Poor	0.41	Poor
Average		0.62	Poor	0.73	Fair

DISCUSSION

Abdominal Organ Injuries Prediction

In the component validations, the maximum strain of the intestinal tract was calculated by simulating the abdominal loading tests with PMHS. In the test, the intestinal tract was damaged only in Case-b2. On the other hand, the maximum axial strain of the intestinal tract calculated by THUMS Version 7 was lowest in Case-b2. Figure 30 shows the abdominal deformation and strain distribution of the intestinal tract at the time of maximum intestinal strain in Case-b2 and Case-b3. In Case-b2, the displacement of the lap belt was 131 mm, which was larger than that in Case-b3 (115 mm). In Case-b2, the lap belt was tilted 30° from the horizontal and the abdominal deflection perpendicular to the body axis was 109 mm. The lap belt generated an energy of 567 J to the abdomen, which was less than 846 J in Case-b3. The fact that the maximum strain on the intestinal tract in Case-b2 was smaller than the value in Case-b3 was consistent with the energy amount relationship. Therefore, the calculated intestinal strain is considered to be reasonable. In the test of Case-b2, a water-filled balloon was inserted into the intestinal tract to measure intestinal stretch. Intestinal injury occurred at 15 locations. Nine of these occurred near the balloon and four occurred between the balloons. This suggests that the balloon affected the occurrence of intestinal injury. Of the six test cases used for simulations, intestinal injury was confirmed only in Case-b2. There is not a sufficient number of data to determine the validity of the predicted results. The mean value of the measured data [21], 37%, was assumed as the threshold for intestinal rupture. However, the standard deviation was 13%, which indicated a large variation. It is desirable to continue to accumulate damage data for validation. Probabilistic damage risk curves can be calculated from simulations. Further data accumulation and model validation are needed for the accurate prediction of mesenteric and vascular damage.

Whole-Body Kinematics Prediction

The whole-body impact kinematics was examined in the frontal collision condition with THUMS Version 7 seated in the reclining position. Figure 27 compares the displacement history curves of key landmarks between THUMS and the PMHS. The curve obtained from Version 7 was closer to the test results than that from Version 6. Comparing the ISO rating values of the two, Version 7 upper body values for Z displacement were better than those for Version 6. Figure 31 shows the spine deformation of the mid-section at 100 ms, when the Z displacement of T1 reached its maximum. The stress distribution in the intervertebral discs and ligaments around the spine was also displayed. In Version 7, the curvature of the spine during flexion was greater than that in Version 6. The position of T1 was about 12 mm lower (Figure 31(a)). As shown in Figure 31(b), the stresses generated in the intervertebral discs and ligaments in Version 7 were lower than those in Version 6. The characteristics of the intervertebral discs and ligaments were revised in Version 7. That lowered the bending stiffness of the spine. The more flexible spine generated a larger Z-displacement at key landmarks and approached the test data. Note that test the conditions did not cause disengagement of the lap belt from the pelvis. The improvement in accuracy of submarining prediction by modifying the pelvic geometry could not be evaluated under the given condition.

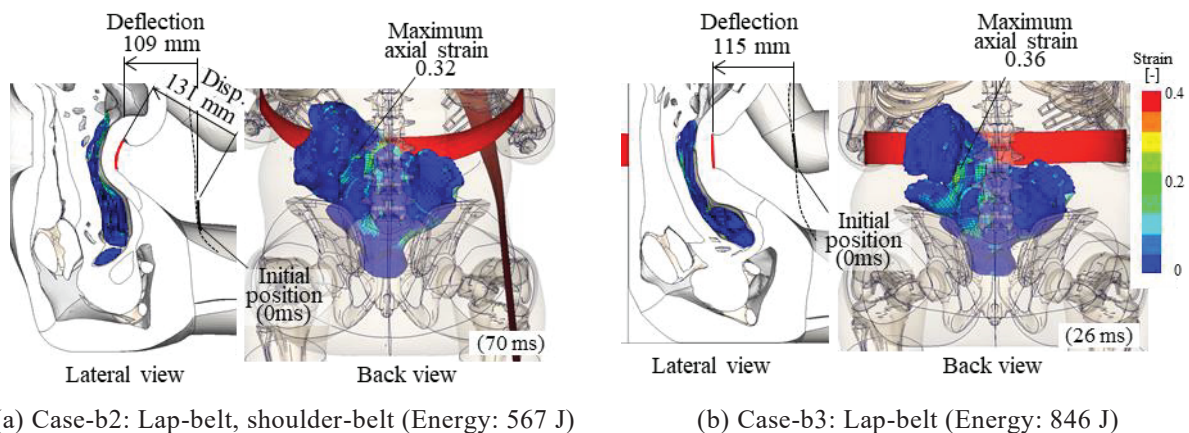


Figure 30. Comparison of abdominal deformity and intestinal tract strain.

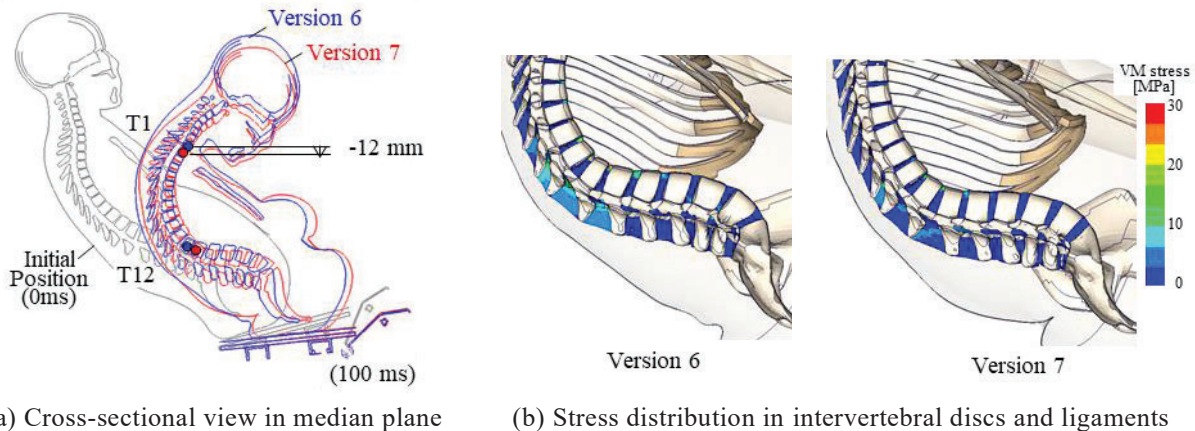


Figure 31. Comparison of spine curvature.

LIMITATION

In a vehicle frontal collision with the occupants seated in a reclined position, there is a possibility that a large load is applied to the abdominal area including the internal organs and lumbar spine. In order to accurately predict the injury risk of the internal organs and lumbar spine, the relevant parts of THUMS have been greatly improved in Version 7. The prediction accuracy was verified under component-level loading conditions for which test data are publicly available. In the validation using the FSU, THUMS predicted vertebral fractures at loading levels close to those in the physical tests. Fracture prediction was not validated for the entire lumbar spine or the entire vertebrae. There are few published test data on damage to the intestinal tract, mesentery, and blood vessels of the small intestine. It is necessary to continue component-level verification, as well as to accumulate test data that can be used as a reference for comparison and reproducible analysis based on crash data.

The vehicle frontal collision test with the occupants seated in a reclining position, referenced in this report, was conducted under a moderate speed (ΔV : 32 kph). The lap belt was well engaged with the pelvis during the test. At a high speed such as 56 kph, it is likely that the occupant moves further forward and the lap belt engagement could be lost depending on the conditions. The pelvis dimensions and the soft tissue thickness around the abdomen may affect the engagement during a collision. Future studies should include the test conditions in which lap belt disengagement could occur.

CONCLUSIONS

This paper describes the development status of the THUMS Version 7. The objectives were first to simulate impact kinematics of an occupant seated in a reclined position during a frontal vehicle collision, and second to accurately predict injuries of the internal organs and lumbar spine. For accurate simulation of the interaction between the pelvis and lap belt, the pelvis geometry was modified to come close to the average size of each body type (AF05, AM50, AM95). The material properties of the skin and adipose tissue of the anterior pelvis were greatly improved in order to better represent those of actual human tissue. The intestinal tract and mesentery structures of the small intestine were precisely represented, and material constitutive laws were introduced to account for anisotropy. For the lumbar spine, the material properties of the intervertebral discs and ligaments were revised, and the realistic distribution of cortical bone thickness of the vertebral bodies was reproduced. The mechanical properties of the abdomen and lumbar spine were validated by comparison with component-level test results. The abdominal load response of the Version 7 when loaded with impactors and belts was found to be similar to the test results. The validity of the mechanical response of the lumbar spine when loaded in compression, shear, and bending was also examined. Comparisons were made with the available test data such that Version 7 reproduced the kinematics of an occupant seated in a reclining position during a frontal collision close to those of the PMHS.

REFERENCES

- [1] Jorlöv, S., Bohman, K., Larsson, A. 2017. "Seating Positions and Activities in Highly Automated Cars - A Qualitative Study of Future Automated Driving Scenarios." IRCOBI Conference, Antwerp, Belgium
- [2] Östling, M., Larsson, A. 2019. "Occupant Activities and Sitting Positions in Automated Vehicles in China and Sweden." 26th International Technical Conference on the Enhanced Safety of Vehicles (ESV), 19-0083, Eindhoven, Netherlands
- [3] Reed, M. P., Zaseck, L., Hu, J. 2019. "Automated Vehicle Occupant Kinematics - Phase I :Task Implementation Plan." University of Michigan Transportation Research Institute
- [4] Kang, Y.-S., Stammen, J., Ramachandra, R., Agnew, A. M., Hagedorn, A., Thomas, C., Kwon, H. J., Moorhouse, K., Bolte IV., J. H. 2020. "Biomechanical Responses and Injury Assessment of Post Mortem Human Subjects in Various Rear-facing Seating Configurations." Stapp Car Crash Journal, Vol. 64, 155-212
- [5] Richardson, R., Donlon, J.-P., Jayathirtha, M., Forman, J. L., Shaw, G., Gepner, B., Kerrigan, J. R. 2020. "Kinematic and Injury Response of Reclined PMHS in Frontal Impacts" Stapp Car Crash Journal, Vol. 64, 83-153
- [6] NHTSA, 2017. "Automated Driving Systems 2.0 - A Vision for Safety." Internet: [https://www.nhtsa.gov/sites/nhtsa.gov/files/documents/13069a-ads2.0_090617_v9a_tag.pdf], Data Accessed November 3, 2022
- [7] Boyle, K. J., Reed, M. P., Zaseck, L. W., Hu, J. 2019. "A Human Modelling Study on Occupant Kinematics in Highly Reclined Seats during Frontal Crashes." IRCOBI Conference, Florence, Italy
- [8] Lin, H., Gepner, B., Wu, T., Forman, J., Panzer, M. 2018. "Effect of Seatback Recline on Occupant Model Response in Frontal Crashes." IRCOBI Conference, Athens, Greece
- [9] Draper, D., Huf, A., Wernicke, P., Peldschus, S. 2019. "The Influence of Reclined Seating Positions on Lumbar Spine Kinematics and Loading in Frontal Impact Scenarios." 26th ESV Conference, 19-0062, Eindhoven, Netherlands
- [10] Gepner, B.D., Draper, D., Mroz, K., Richardson, R., Ostling, M., Pipkorn, B., Forman, J. L., Kerrigan, J. R. 2019. "Comparison of Human Body Models in Frontal Crashes with Reclined Seatback" IRCOBI Conference, Florence, Italy
- [11] Mroz, K., Östling, M., Richardson, R., Kerrigan, J., Forman, J., Gepner, B., Lubbe, N., Pipkorn, B. 2020. "Effect of Seat and Seat Belt Characteristics on the Lumbar Spine and Pelvis Loading of the SAFER Human Body Model in Reclined Postures", IRCOBI Conference, Munich, Germany
- [12] Shigeta, K., Kitagawa, Y., Yasuki, T. 2009. "Development of Next Generation Human Body FE Model Capable of Organ Injury Prediction." 21st ESV Conference, 09-0111, Stuttgart, Germany
- [13] Iwamoto, M., Nakahira, Y., Kimpara, H. 2015. "Development and Validation of the Total HUMAN Model for Safety (THUMS) Toward Further Understanding of Occupant Injury Mechanisms in Precrash and During Crash." Traffic Injury Prevention, 16 sup1, S36 - S48
- [14] Iwamoto, M., Nakahira, Y., Tamura, A., Kimpara, H., Watanabe, I., Miki, K. 2007. "Development of Advanced Human Models in THUMS." 6th European LS - DYNA Users' Conference, Gothenburg, Sweden
- [15] Kato, D., Nakahira, Y., Atsumi, N., Iwamoto, M. 2018. "Development of Human - Body Model THUMS Version 6 Containing Muscle Controllers and Application to Injury Analysis in Frontal Collision after Brake Deceleration." IRCOBI Conference, Athens, Greece
- [16] Hwang, E., Hallman, J., Klein, K., Rupp, J., Reed, M. P., Hu, J. 2016. "Rapid Development of Diverse Human Body Models for Crash Simulations through Mesh Morphing." SAE 2016-01-1491
- [17] University of Michigan Transportation Research Institute (UMTRI), "Human Shapes: Realistic Human Body Shape Modeler Based on Real Data" Internet: [<http://humanshape.org/>], Data Accessed November 3, 2022
- [18] Annaihd, A. N., Bruyere, K., Destrade, M., Gilchrist, M. D., Ottenio, M. 2012. "Characterization of the Anisotropic Mechanical Properties of Excised Human Skin." Journal of the Mechanical Behavior of Biomedical Materials, 5, 139-148
- [19] Sun, Z., Lee, S.-H., Gepner, B. D., Rigby, J., Hallman, J. J., Kerrigan, J. R. 2021. "Comparison of Porcine and Human Adipose Tissue Loading Responses under Dynamic Compression and Shear: A Pilot Study." Journal of the Mechanical Behavior of Biomedical Materials, 113, 104112
- [20] Nakahira, Y., Watanabe, I., Iwamoto, M. 2019. "Investigation of Small Intestine and Mesentery Modeling Methods to Analyze Traumatic Abdominal Injury." JSAE 20196202
- [21] Egorov, V. I., Schastlivtsev, I. V., Prut, E. V., Baranov, A. O., Turusov, R. A. 2002. "Mechanical Properties of the Human Gastrointestinal Tract" Journal of Biomechanics, 35, 1417-1425

- [22] Inoue, T. 1957. "Experimental Studies on Physical Strength of Gastrointestinal Serous Membranes." *Medical Journal of Kobe University*, Vol. 11, No. 3, 420-435
- [23] Yamada, H., Evans, F.G. (Ed.) 1970. "Strength of Biological Materials" Williams & Wilkins, USA
- [24] Kemper, A., McNally, C., Manoogian, S., McNeely, D., Duma, S. 2013. "Stiffness Properties of Human Lumbar Intervertebral Discs in Compression and the Influence of Strain Rate." *SAE 07-0471*, 127-133
- [25] Lourenço, C., Claro, J. C. P. 2015. "Biomechanical Experimental Data Curation: An Example for Main Lumbar Spine Ligaments Characterization for a MBS Spine Model." *Mechanisms and Machine Science*, ISSN 2211-0984, Vol. 24
- [26] Picazo, M. L., Baro, A. M., Barquero, L. M. D. R., Gregorio, S. D., Martelli, Y., Romera, J., Steghöfer, M., Ballester, M. A. G., Humbert, L. 2018. "3-D Subject-Specific Shape and Density Estimation of the Lumbar Spine from a Single Anteroposterior DXA Image Including Assessment of Cortical and Trabecular Bone" *IEEE Transactions Medical Imaging*, 37(12), 2651-2662
- [27] Zhao, F.-D., Pollintine, P., Hole, B. D., Adams, M. A., Dolan, P. 2009. "Vertebral Fractures Usually Affect the Cranial Endplate Because It Is Thinner and Supported by Less-dense Trabecular Bone." *Bone*, 44(2), 372–379
- [28] Ritzel, H., Amling, M., Pösl, M., Hahn, M., Delling, G. 1997. "The Thickness of Human Vertebral Cortical Bone and Its Changes in Aging and Osteoporosis: A Histomorphometric Analysis of the Complete Spinal Column from Thirty-Seven Autopsy Specimens." *Journal of Bone and Mineral Research*, Vo. 12, No. 1
- [29] Kerrigan, J. 2020. "Experiments to Address Limitations in Biofidelity of Human Body Models for Autonomous Vehicles" Government/Industry Meeting, Washington, USA
- [30] Cavanaugh, J. M., Nyquist, G. W., Goldberg, S. J., King, A. I. 1986. "Lower Abdominal Tolerance and Response" 30th Stapp Car Crash Conference, SAE 861878, 41-63
- [31] Nusholtz, G. S., Kaiker, P. S., Lehman, R. J. 1988. "Steering System Abdominal Impact Trauma" UMTRI-88-19, Michigan, USA
- [32] Hardy, W. N., Schneider, L. W., Rouhana, S. W. 2001. "Abdominal Impact Response to Rigid-Bar, Seatbelt, and Airbag Loading." *Stapp Car Crash Journal*, Vol. 45
- [33] Howes, M. K., Hardy, W. N. 2015. "Evaluation of the Kinematic Responses and Potential Injury Mechanisms of the Jejunum during Seatbelt Loading" *Stapp Car Crash Journal*, Vol. 59, 225-267
- [34] Foster, C. D., Hardy, W. N., Yang, K. H., King A. I. 2006. "High-Speed Seatbelt Pretensioner Loading of the Abdomen." *Stapp Car Crash Journal*, Vol. 50, 27-51
- [35] Arun, M. W. J., Hadagali, P., Driesslein, K., Curry, W., Yoganandan, N., Pintar, F. A. 2017. "Biomechanics of Lumbar Motion-Segments in Dynamic Compression." *Stapp Car Crash Journal*, Vol. 61, 1-25
- [36] Belwadi, A., Yang, K. H. 2008. "Response of the Cadaveric Lumbar Spine to Flexion, with and without Anterior Shear Displacement." IRCOBI Conference, Bern, Switzerland
- [37] Chastain, K. L. 2021. "Characterization of the Mechanical Response of the Lumbar Spine: The Effect of a Compressive Axial Load." Master's Thesis for the University of Virginia
- [38] Tushak, S. K., Donlon, J. P., Gepner, S. D., Chebbi, A., Pipkorn, B., Hallman, J. J., Forman, J. L., Kerrigan, J. R. 2022. "Failure Tolerance of the Human Lumbar Spine in Dynamic Combined Compression and Flexion Loading." *Journal of Biomechanics*, 135, 111051
- [39] NHTSA, 2022. "Biomechanics Test Database" Internet: [<https://www.nhtsa.gov/research-data/research-testing-databases#/biomechanics>], Data Accessed September 19, 2022
- [40] Uriot, J., Potier, P., Baudrit, P., Trosseille, X., Petit, P., Richard, O., Compigne, S., Masuda, M., Douard, R. 2015. "Reference PMHS Sled Tests to Assess Submarining." *Stapp Car Crash Journal*, Vol. 59
- [41] ISO/TS 18571, 2014. "Road vehicles - Objective Rating Metric for Non-ambiguous Signals." International Organization for Standardization, Geneva, Switzerland
- [42] Gordon, C. C., Blackwell, C. L., Bradtmiller, B., Parham, J. L., Barrientos, P., Paquette, S. P., Corner, B. D., Carson, J. M., Venezia, J. C., Rockwell, B. M., Mucher, M., Kristensen, S. 2014. "2012 Anthropometric Survey of U.S. Army Personnel: Methods and Summary Statistics." U.S. Army Natick Soldier Research, Development and Engineering Center, Natick, Massachusetts, USA
- [43] Mohr, M., Abrams, E., Engel, C., Long, W. B., Bottlang, M. 2007. "Geometry of Human Ribs Pertinent to Orthopedic Chest-Wall Reconstruction." *Journal of Biomechanics*, 40, 1310-1317
- [44] Charpail, E., Trosseille, X., Petit P., Laporte, S., Lavaste, F., Vallancien, G. 2005. "Characterization of PMHS Ribs: A New Test Methodology." *Stapp Car Crash Journal*, Vol. 49, 183-198
- [45] Netter, F. H. 2007. "Netter Atlas of Human Anatomy 4th Ed." Elsevier

APPENDIX

Other Modifications and Validations

In addition to the model modifications of the abdomen and lumbar region, another four items were updated in THUMS Version 7 as shown in Table 1, Body Region - Others. The details of the updates are described below.

Head Model The head sizes were revised. The mean measured head dimensions [42] and THUMS dimensions for each body type (AF05, AM50, AM95) are shown in Table A-1. The head dimensions were adjusted to match the average size.

Rib Model Version 6 assumed uniform cortical bone thickness in all ribs. Version 7 considered the realistic distribution of cortical bone thickness [43] for the ribs (Figure 8). The fracture loads and deflection rates of the ribs (AM50, 4th rib) under bending loading that became closer to the test results [44] (Figure A-1).

*Table A-1.
Head geometry.*

	AF05			AM50		
	Measurement (Gordon, 2014)	THUMS V6	THUMS V7	Measurement (Gordon, 2014)	THUMS V6	THUMS V7
Breadth [mm]	140	142 (+ 2)	140 (0)	154	165 (+11)	154 (0)
Height [mm]	208	225 (+17)	208 (0)	238	262 (+24)	238 (0)
Length [mm]	178	183 (+ 5)	178 (0)	200	212 (+12)	200 (0)
Weight [kg]	-	3.7	3.4	-	5.4	4.6

	AM95		
	Measurement (Gordon, 2014)	THUMS V6	THUMS V7
Breadth [mm]	163	165 (+ 2)	163 (0)
Height [mm]	251	262 (+11)	251 (0)
Length [mm]	211	212 (+ 1)	211 (0)
Weight [kg]	-	5.4	5.3

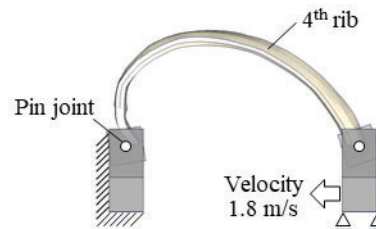
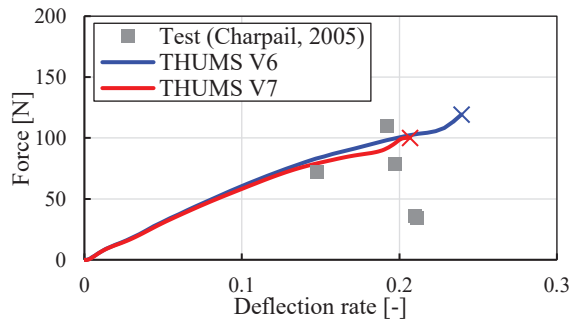
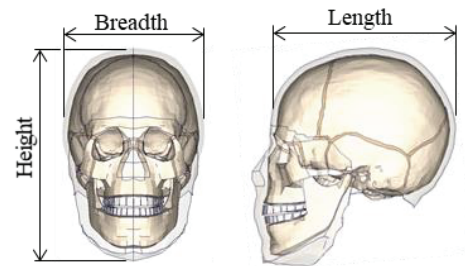


Figure A-1. Force vs. deflection rate curve during rib bending

Heart Model Version 7 more accurately represents the anatomical structure and characteristics of the heart. Figure A-2 shows the heart models of Version 6 and Version 7. The heart model of Version 6 was modeled as a single homogeneous structure. In Version 7, the septal wall, the connections with the great vessels, and the blood inside were separately represented [45]. The myocardium was modeled using hexa-elements with three or more elements in the thickness direction, and large blood vessels such as the aorta and vena cava were modeled using a single hexa-solid element. The material properties [23] were assumed to be hyperelastic. The blood was filled inside the heart and blood vessels with tetra-solid elements. The material properties of the blood were assigned with Elastic fluid model. The load response characteristics of the heart examined by applying a compressive load on a rigid table. The simulation result was found to be close to the test result (Figure A-3).

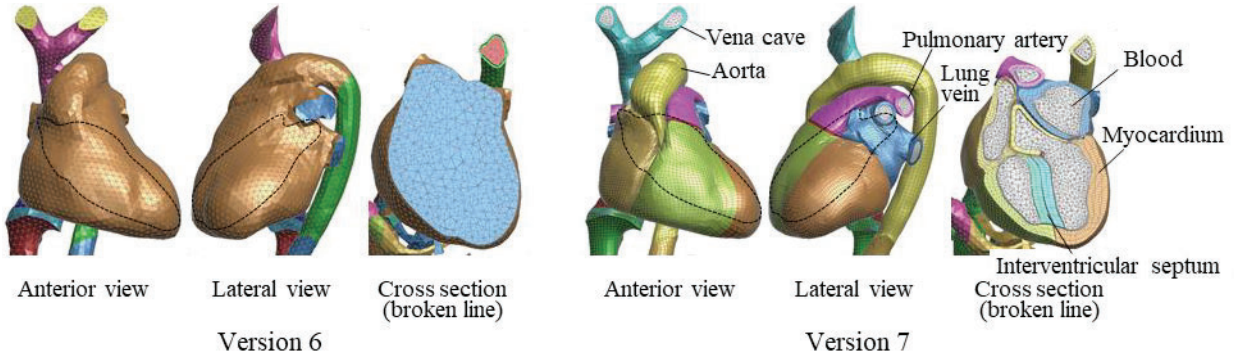


Figure A-2. Heart model.

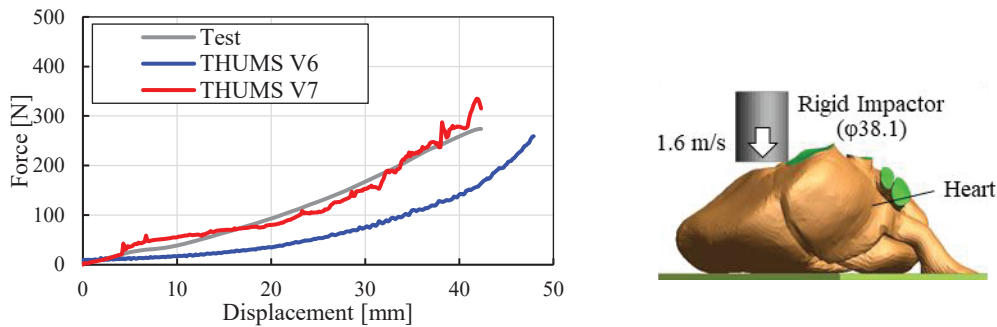


Figure A-3. Force vs. deflection rate curve in heart compression

Long Bone Model In Version 6, the inside part of the long bones (femur, tibia, fibula, and humerus) was assumed as cancellous bone. In Version 7, the internal marrow section was added to mimic the actual bony structure [45] (Figure A-4). The load-displacement characteristics of the femur in three-point bending are shown in Figure A-5. The load-displacement characteristics of the Version 7 femur were close to the test results [23].

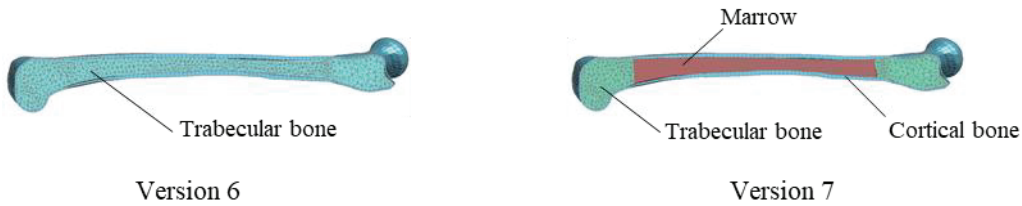


Figure A-4. Long bone model (Femur).

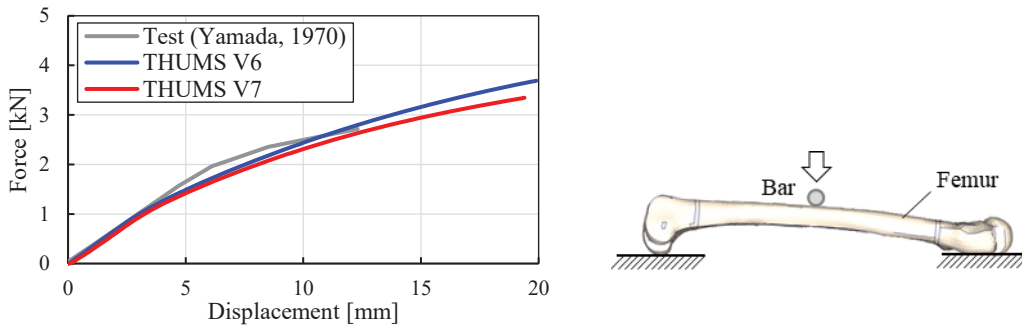


Figure A-5. Force vs. deflection rate curve during femur 3-point bending

QUANTITATIVE EVALUATION OF HUMAN BODY MODEL GRAVITY SETTLING

B. Wade von Kleeck

Wake Forest University School of Medicine

United States of America

Juliette Caffrey

Wake Forest University School of Medicine

United States of America

Jason Hallman

Toyota Motor North America R&D

United States of America

Ashley A. Weaver

Wake Forest University School of Medicine

United States of America

F. Scott Gayzik

Wake Forest University School of Medicine

United States of America

Paper ID: 23-0050

ABSTRACT

The simulated action of coupling a computational human body model to a vehicle seat, commonly referred to as model settling, is an essential, initial aspect of any crash simulation. There is a gap in knowledge related to the necessary duration of this activity to sufficiently couple the human model to the seat. In this study, THUMS v4.1 was gravity-settled in two postures, an upright driver and a reclined occupant, into a seat model. Simulations were performed using three seat foam stiffnesses, three friction coefficients and both with and without a constraint on the motion of the pelvis for a total of 18 simulations per posture. Each simulation was run for 800 ms, a time determined to be sufficiently long to identify a settled end state. In separate simulations, a 0.5g magnitude, 200 ms half sine wave pulse was applied to the seat in the backwards direction to measure coupling between the human body model (HBM) to the seat.

Model quality metrics were measured at the first four kinetic energy local maximums and local minimums to compare physically consistent time points between simulations. Kinetic energy, contact penetrations, change in HBM element quality, seated contact area and seat pressure were measured and compared to this settled end state. A pass/fail range was assigned to each metric. A pass was assigned if the value fell within ± 1 standard deviation of the average simulated end state value at 800 ms (contact area, seat pressure) or between the simulated end state value and the baseline THUMS value (contact penetrations, model quality, perturbation test). A passing time point for a simulation received a score of 1, a failing time point for a simulation received a score of 0. Scores for all simulations were added and normalized for each local maximum and local minimum, and the first time point to receive a score greater than 3 (out of 5) and pass the perturbation test was determined to be sufficiently settled.

The third kinetic energy local minimum was selected for the upright driver posture and third local maximum for the reclined occupant. Both have average gravity settling times of approximately 405 ms. The pelvis constraint appeared to contribute to a more rapid arrival at the long term settled state for the upright seated posture. Constraining the pelvis is not recommended for the reclined posture. The results suggested that for best practice a settling time of at least 400 ms is required to sufficiently couple the model to the seat in either posture.

INTRODUCTION

Finite element (FE) human body models (HBMs) are detailed models which may be used in the investigation of injury risk and vehicle safety. HBMs such as the Total Human Model for Safety (THUMS) and the Global Human Body Models Consortium (GHBMC) models have been used for pedestrian injury assessment [1] and occupant injury risk evaluation [2, 3]. Simulations of injury are highly complex, and the positioning of the HBM into a vehicle model may affect repeatability and accuracy of the resulting injury predictions [4, 5]. Typical vehicle crash simulation workflow involves a repositioning phase and a gravity settling phase before the crash simulation. Previous work has shown that optimal simulation time for repositioning is 100 ms followed by 30 ms of holding time [6]. This recommendation is consistent across a variety of postures and optimizes for simulation run time and element quality.

While model positioning can be achieved through numerous methods and crash simulation inputs are typically well defined, little attention has been paid to gravity settling. The interaction between the HBM and the seat is critically important as the degree of coupling between the HBM and the seat can influence model kinematics. A HBM that is too tightly coupled or insufficiently coupled to a seat will have unrealistic excursion in a simulated vehicle crash.

No industry standard exists for gravity settling prior to vehicle crash simulations. Gravity settling times between 100 ms and 1 s have been cited [7, 8], but gravity settling time is commonly not explicitly stated in publications. Longer gravity settling simulation time results in longer computation time and higher computation and storage costs. The goal of this design of experiments HBM gravity settling study is to determine best practices to gravity settle seated HBMs in the upright driver and reclined occupant postures.

METHODS

Models Used

The FE models used in the gravity settling simulations were one of the National Crash Analysis Center (NCAC) full-scale vehicle models [9], slightly modified to increase simulation speed, and the Total Human Model for Safety (THUMS AM50) v4.1 50th percentile male HBM [10]. The THUMS model was positioned into two postures using best practices that optimized mesh quality and simulation time per methods in Costa et al. 2020 [6]. An upright driver posture (**Figure 1A**), [11] and a 53° seatback angle reclined occupant posture [12] (**Figure 1B**) were used. . In the upright driver posture, seat position and seat angle were matched to values used in Reed, et al. 2002 [11]. In the reclined occupant posture, the seat back angle was based off of the position used in Reed et al., 2019 [12], with the seat positioned to avoid intersections with the THUMS foot and the front vehicle wall.

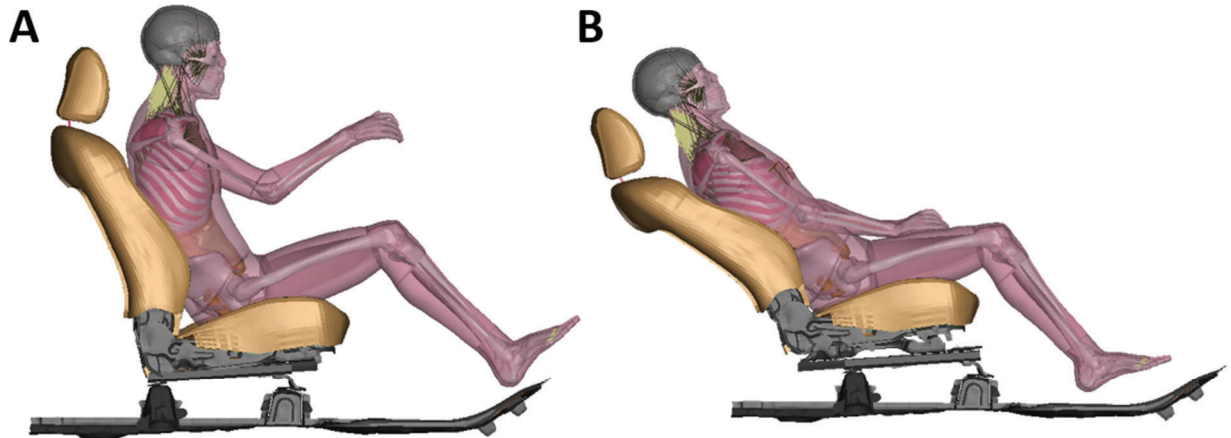


Figure 1: Upright driver posture (A) and reclined occupant posture (B). The THUMS model was positioned in a 130 ms simulation, with 100 ms of repositioning time and 30 ms of holding time.

Simulations

To quantify settling over a range of potential vehicle inputs, 18 test cases were simulated for each posture: 3 seat friction coefficients * 3 seat stiffnesses * 2 constraint definitions for pelvis motion. Three values of friction coefficient that span a large range of potential seat and clothing material combinations were used: 0.2, 0.5 and 0.8 [13-15]. Three seat stiffness multipliers were used: 0.1, 1.0 and 10.0. These were used to scale the y-axis of the load curve for the seat foam material model, and spanned a wide range to account for a variety of seat foam materials available [16].

Simulations were conducted with and without a constraint on pelvis motion. Simulations without constraint moved only under the load of gravity. Simulations with constraint used single point constraints on each pelvis node to limit the pelvis to move only along the vector of the initial THUMS to the target NCAC vehicle H-Point. The NCAC vehicle H-point was determined from a matching New Car Assessment Program (NCAP) oblique offset crash test (National Highway Traffic Safety Administration, NHTSA No: RB5137).

Additional Constraints

For each simulation, several constraints were applied to make the model settle in a physically realistic manner. In both postures, the head was constrained to prevent rotation about the C7/T1 joint Y-axis. This maintained neck posture, preventing the head from slouching forward. In the upright driver posture, the hands were positioned to their final position on the steering wheel, and were point constrained during settling. In the reclined occupant posture, the hands were positioned to touch the upper thigh. This was the desired posture, but to avoid undesired arm and shoulder kinematics the hands were allowed to move along the sagittal plane (e.g. along the thigh length), but motion was constrained normal to the plane. This allowed for natural arm movement during gravity settling, but prevented the hands from falling down the side of the leg.

Simulation Matrix

With the combination of three friction coefficients, three stiffness multipliers and two pelvis constraints, a total of 36 simulations were run (18 simulations for each posture). Each simulation was run for 800 ms of simulation time, a time determined in preliminary simulations to be sufficient to reduce kinetic energy of the HBM to near zero. All simulations were run on equivalent hardware on a high-performance computing cluster using LS-Dyna (v.11.0, ANSYS, Canonsburg, PA).

Data Extraction

Kinetic energy of the HBM, and the contact penetrations, contact area, seat pressure and perturbation displacement were extracted using LS-PrePost v4.8.18 (ANSYS, Canonsburg, PA). Distortion index, a measure of HBM element quality, was measured using ANSA (ANSYS, Canonsburg, PA) and Matlab (Mathworks, Natick, MA).

Kinetic Energy Features

Kinetic energy was measured in the THUMS HBM parts only, with total kinetic energy reported. To maintain consistency across the physical features of settling, the first four local maximums and local minimums of the kinetic energy traces were extracted (**Figure 3**). These were used to measure the other model features at times that were kinetically consistent, but may not be consistent in simulation time.

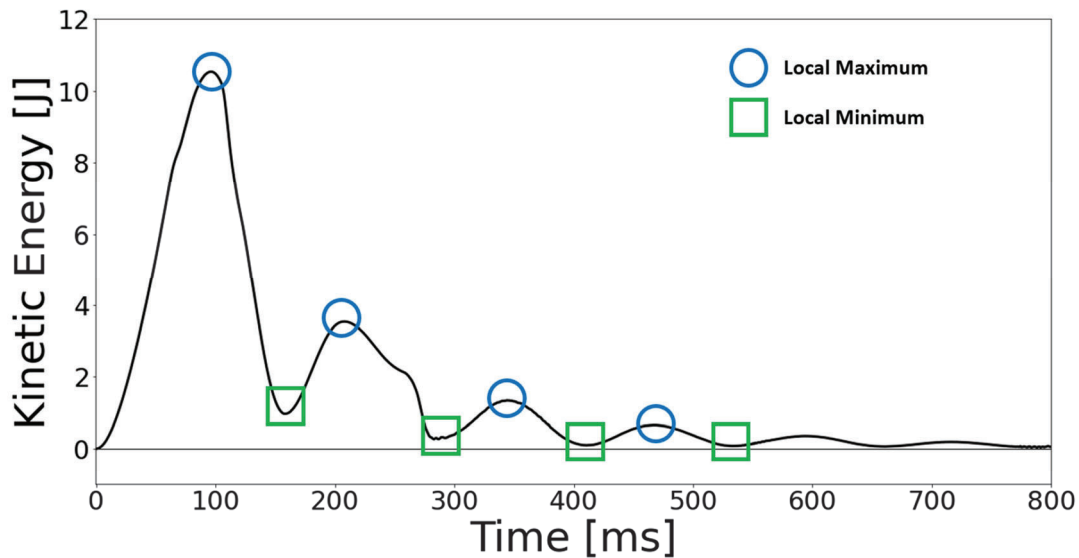


Figure 2: Kinetic energy (KE) features are the first four local maximums and local minimums. Example kinetic energy plot from an upright driver simulation.

Contact Penetrations

Contact penetrations were measured at each kinetic energy feature for each contact defined in the THUMS HBM (skin, right leg, left leg, organs, right arm, left arm, head, pia sagittal-falx and body). A cutoff threshold of 0.0376 mm (1% of average element length) was applied to exclude small penetrations that do not significantly contribute to model quality. The mean contact penetration length and the 95th percentile contact penetration length were measured.

Contact Area

The HBM-to-seat contact area was measured using the nodal force outputs from the seat contact. Each seat shell element that had two or more of its nodes with a force greater than zero was considered to be in contact with the seat model. Elements with all four nodes with non-zero force were fully in contact, elements with only two or three nodes with non-zero force were counted as partially in contact. The full area of each full contact element was measured and half the area of each partially contacted element was measured.

Seat Pressure

Seat pressure induced by the HBM was measured from simulation d3plot data in LS-PrePost. A subset of elements from the seat pan and seat back that fully encompassed the extent of the contact area of the seat were selected. The average pressure of the elements in this region was measured.

Distortion Index

A HBM quality metric called the distortion index was used to measure how model quality changed over time. This metric was explained in detailed in Costa et al., 2021 [6] and is explained briefly here. The distortion index quantifies the whole model element quality by assigning a score for each element and summing over all elements to give a score for the HBM. The score for each element is based on the value of several measurements of element quality (such as skew or Jacobian) and their difference from the element's ideal value. A value of 0 is given for a perfect element, and 1 is given for exceeding specified criteria for each measure of element quality. The average score of each element's quality metric scores are summed over the whole model to give a total score. This score can then be used to quantify changes in element quality, with higher numbers having poorer element quality.

Perturbation Test

An additional subset of simulations were run to measure the coupling between the HBM and the seat. The simulation was a perturbation test of the settled model at the eight kinetic energy features as well as at the simulation end time, 800 ms. The model was allowed to settle to its specified time, after which an acceleration pulse was applied to the seat in the positive X-direction (**Figure 6**). The pulse was a 200 ms half sine wave with a 0.5g magnitude, similar to perturbation pulses used in human subject experiments [17-19]. Relative displacement of the THUMS H-Point to a node on the rear of the seat was measured. Zero relative displacement would indicate that the HBM was fully coupled to the seat, while 65 mm of relative displacement (acceleration pulse twice integrated) would indicate no coupling between the HBM and the seat. The perturbation test was run for each kinetic energy feature (four KE local maximums and four KE local minimums) and the simulation end state (800 ms) in all three seat stiffness values (0.1x, 1.0x and 10.0x) and one seat friction coefficient (0.5) for each posture.

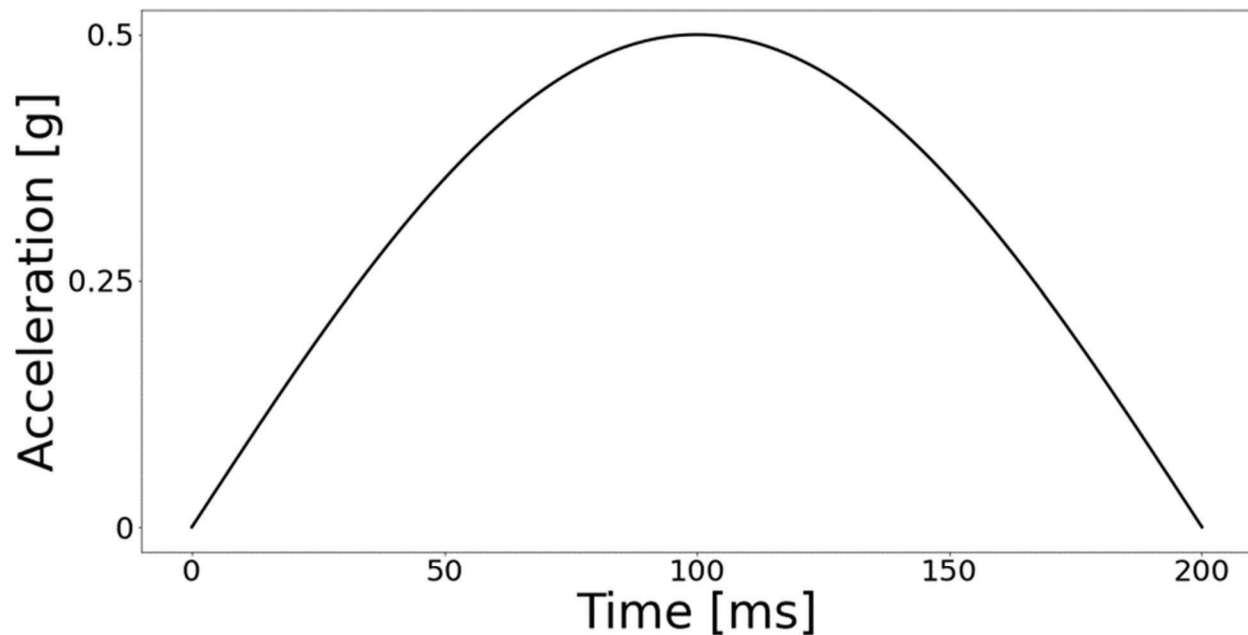


Figure 3: The pulse applied in the perturbation test, where acceleration is applied to the seat in the negative X-direction after gravity settling.

Scoring and Target Criteria

To determine whether the pelvis should be constrained or unconstrained, the time for kinetic energy to be consistently below 10% of the peak kinetic energy was measured. The constraint (with or without pelvis constraint) with the lower average time to be consistently below 10% peak kinetic energy for each posture was determined to

reach equilibrium faster, and therefore reach an end state faster. Only the constraint with the lower time to be consistently below 10% peak kinetic energy was used in further analysis.

To identify the ideal settling time, by way of kinetic energy feature, each of the above values (distortion index, contact penetrations, perturbation test, contact area and seat pressure) were assigned a score of 1 or 0 based on their proximity to the average end of simulation value (average value at 800 ms simulation time). Each metric was scored at each kinetic energy feature for the 9 simulations (3 seat stiffnesses, 3 friction coefficients and 1 constraint for each posture) to identify the highest scoring time point.

For metrics independent of the seat (contact penetrations and distortion index), the score was based on whether the value fell within the range of the baseline THUMS value and the simulation end point value (800 ms settling time). A score of 1 was assigned if it fell within this range, a score of 0 was assigned if it fell outside of this range. For metrics dependent on the seat (contact area and seat pressure), the score was based on whether a value fell within ± 1 standard deviation of the average end of simulation value (Figure 7). For the perturbation test, a score of 1 was assigned if a value was less than or equal to the end time point (800 ms) perturbation test's relative hip displacement and a score of 0 was assigned if it was greater than the relative hip displacement.

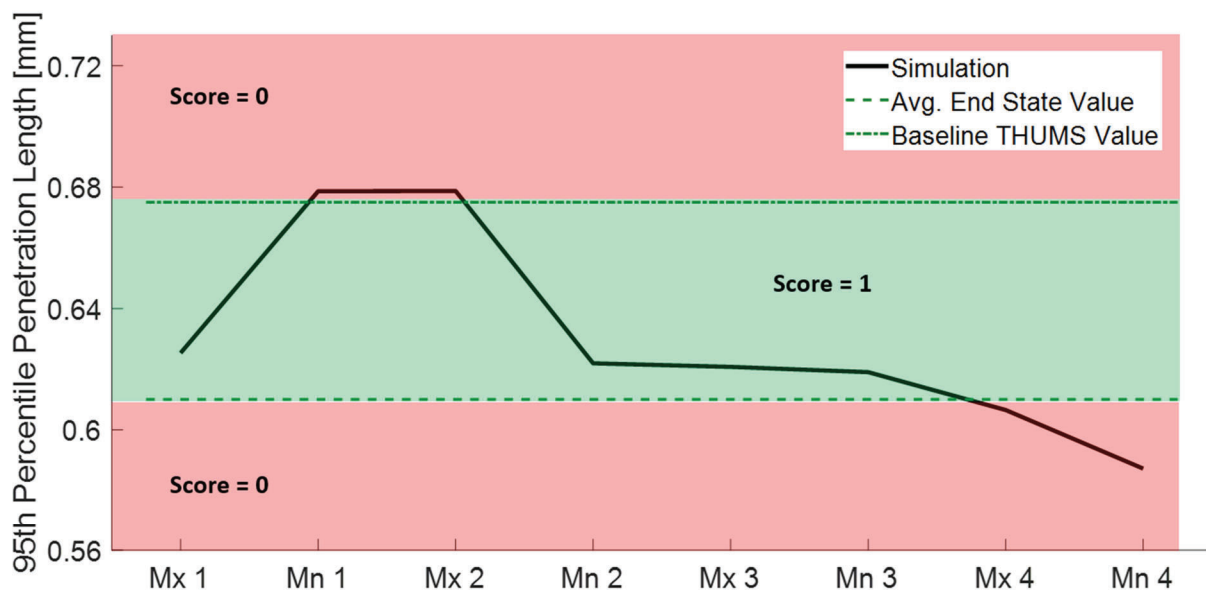


Figure 4: Example scoring of contact area for a single simulation. Local maximums 1 and 3 fall outside of ± 1 standard deviation of the mean end state (800 ms) contact area and receive scores of zero. Local minimums 1, 2 and 4 and local maximum 4 fall within of ± 1 standard deviation of the mean end state (800 ms) contact area and receive a score of 1. (Mx is local maximum and mn is local minimum).

For each metric and each time point, the total score was normalized by the number of simulations run for that metric. This was performed to weight all of the metrics equally. At each time point, the normalized score of each metric was summed to give a score for the kinetic energy feature. The ideal time point was the first time point that both scored in the perturbation test and had a total score greater than or equal to 3. This enabled selection of a settled model that best approximated a fully settled state at a shorter simulation time.

RESULTS

Upright Driver Posture

Pelvis Constraint

For the upright driver posture, the average time to be consistently below 10% of peak kinetic energy was 530 ms in the unconstrained pelvis simulations and 390 ms in the constrained pelvis simulations. The constrained pelvis simulations were selected for the upright driver posture analyses, as applying this constraint improved settling time.

Scoring

To avoid overweighting contact penetrations, the scores for mean penetration length and 95th penetration length were averaged to give a single score for contact penetrations called the penetration score. Individual normalized metric scores can be seen in **Figure 5**. For example, at the kinetic energy local maximum 1 (Mx1) no simulation was within ± 1 standard deviation of the average end state contact area, so it received a score of 0. At the kinetic energy local minimum 3 (Mn3), four of the nine simulations had contact areas within this range, giving a score of 4/9. The internal HBM metrics (distortion index and penetration score) are generally stable, having higher scores throughout all kinetic energy features. The external metrics (contact area, seat pressure and perturbation test) are more variable, but have a slight trend of increasing with more settling time.

Both kinetic energy local minimum 3 and local maximum 4 have a passing score ≥ 3 , and also were consistently below 10% of the peak kinetic energy in the perturbation test. Thus, for the upright driver posture, local minimum 3 is recommended to achieve HBM-to-seat coupling that meets the target criteria for metrics of HBM mesh quality and HBM-to-seat interaction. This is a settling time of 402 ± 21 ms.

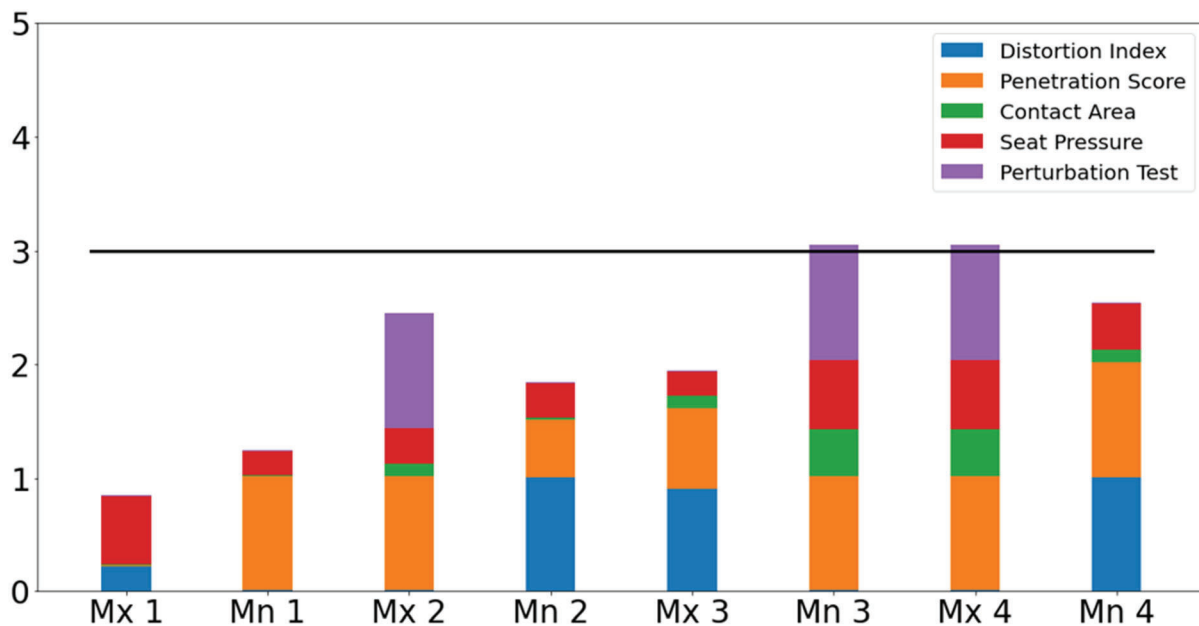


Figure 5: Normalized scores for each metric at each kinetic energy feature time point (max: Mx, min: Mn) for the upright driver posture simulations with pelvis constraint. Higher scores indicate better settling performance. Kinetic energy local minimum 3 (Mn3) is the first time point to meet the target criteria (≥ 3). Black line is a score of 3, passing.

Reclined Occupant Posture

Pelvis Constraint

For the reclined occupant posture, the average time to be consistently below 10% peak kinetic energy was 290 ms in the unconstrained simulations and 410 ms in the constrained pelvis simulations. The unconstrained pelvis simulations were selected for the reclined occupant posture analyses, as not applying a constraint improved settling time.

Scoring

As in the upright driver posture, mean penetration length and 95th percentile penetration length scores were averaged to give a penetration score. The normalized metric scores can be seen in **Figure 6**. The internal HBM metrics are generally stable, having higher scores throughout all kinetic energy features. The external metrics are more variable, but have a slight trend of increasing with time. From kinetic energy local maximum 3 onward, the reclined occupant posture has a score of 3 or above, and kinetic energy local maximum 3 through kinetic energy

local maximum 4 score were consistently below 10% of the peak kinetic energy in the perturbation test. Thus, for the reclined occupant posture, the third kinetic energy maximum is recommended to achieve HBM-to-seat coupling that meets the target criteria for metrics of HBM mesh quality and HBM-to-seat interaction. This is a settling time of 405 ± 67 ms.

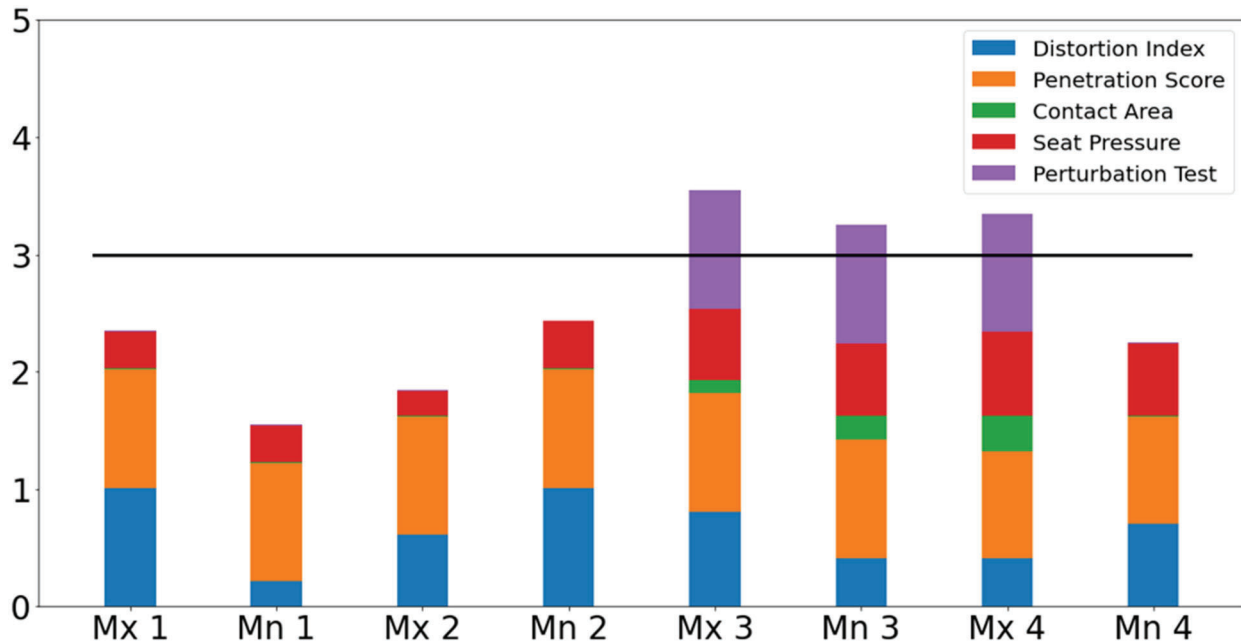


Figure 6: Normalized scores for each metric at each kinetic energy feature time point (max: Mx, min: Mn) for the reclined occupant posture simulations without pelvis constraint. Higher scores indicate better settling performance. Kinetic energy local maximum 3 (Mx3) is the first time point to meet the target criteria (≥ 3). Black line is a score of 3, passing.

DISCUSSION

The goal of this work was to use model agnostic, repeatable methods to establish best practices for gravity settling HBMs. For the two postures examined, a gravity settling time of approximately 400 ms was sufficient to settle the model into the seat. This was determined by comparing earlier time points in a simulation to a later time point with negligible kinetic energy. This indicates that an earlier time point for gravity settling can save computational cost with little to no effect on model performance. By further comparing earlier time points to a later time point in a perturbation test, earlier time points can be tested for target suggest levels of HBM-to-seat coupling.

In the upright driver case, results indicate that using a constraint on the motion of the pelvis and gravity settling for roughly 400 ms yielded results similar to a much longer settling time. For the reclined occupant, using no pelvis constraint yielded improved results based on the metric presented, and gravity settling for roughly 400 ms was similar to a much longer settling time. Both of these were tested across a combination of seat parameters, and both postures had similar or superior model quality metrics than the simulation's final 800 ms state. These settling times also exhibited similar coupling to the seat as the simulation's final state.

Poor coupling of an HBM to a seat can yield unrealistic simulation results, so particular attention was paid to the perturbation test in this study. The pulse used was similar to pulses used in human subject observation in the literature [17, 18]. Requiring that the selected time points pass the perturbation test ensures that the time points are adequately coupled to the seat and saves computational cost. Relative to the simulated end point, the selected time points save an average of 21.5 hours (43 hours to 800 ms versus 21.5 hours to 405 ms) on the hardware used.

The differences in the recommendations for the pelvis constraint of each postures raises the question of what is the best practice in gravity settling. Without a large combination of postures, H-point targets, and seat models it would be difficult to test, however one explanation is that the precision of the H-point definition influences the outcome. The upright driver posture H-point was based on physical testing and therefore is well quantified. However in the reclined occupant posture the H-point target was not experimentally derived. The H-point target was based on the upright driver posture and adjusted for the seat pan movement. In this case, using the pelvis constraint was found to increase the settling time. It also resulted in different H-point trajectories than not using a pelvis constraint. While a true target H-point is unknown, it is likely that the final H-point in the unconstrained posture is more realistic. It was also determined that in the absence of a known target, it was best to let the physics of the simulation dictate the location of the H-point. These results suggest that the best practice in selecting pelvis constraints when settling is to use a constraint when the target H-point is well defined, and not use a constraint when a target H-point is not experimentally defined or measured.

Limitations

Several limitations exist in this work. One is that only two postures were examined, and that both were symmetric. These postures were selected for their broad applicability across a span of seat back ranges and broad use in driver and occupant seated postures. Another limitation of this work was the use of a single HBM and seat. The results of this study are specific to the THUMS AM50 and NCAC seat model, however the methods are model agnostic and can be repeated for other HBMs and seats. While only one seat was used, a wide range of seat stiffnesses and seat friction coefficients were used to represent a diverse range of seats.

CONCLUSIONS

In this study gravity settling simulations were performed to identify settling times with results similar to long duration gravity settling simulations. Gravity settling simulations using the THUMS HBM in an upright driver posture and a reclined occupant posture in a NCAC seat were run for 800 ms under combinations of seat stiffness (0.1x, 1x and 10x baseline stiffness) and friction coefficients (0.2, 0.5 and 0.8). The utility of constraints on the motion of the pelvis were also investigated. The simulations were investigated at 8 kinetically identical time points for metrics of model quality and coupling to the seat and evaluated against the baseline HBM and final end state of the settling simulation. Recommendations for pelvis constraint were made based on the time to reach 10% of the peak kinetic energy. In the upright driver posture the pelvis constraint reduced that time and we recommend using the constraint. In the reclined occupant posture the pelvis constraint reached 10% of the peak kinetic energy more slowly than without it, and it is not recommended. This is likely due to the H-point not being experimentally defined in the reclined occupant posture. Based on the scores of each posture, a gravity settling time of approximately 400 ms is recommended, as it was found to be optimal based on performance relative to the final end state and simulation time. Because a wide range of seat foam stiffnesses and seat friction coefficients were tested, gravity settling for 400 ms is likely sufficient for most postures.

ACKNOWLEDGEMENTS

The Wake Forest University team gratefully acknowledges the support of the Toyota Collaborative Safety Research Center and Toyota Motor Corporation. This work was facilitated by our regular collaboration with Mitsutoshi Masuda, Shigeki Hyashi, Yoshiki Takahiri, Haruthosi Motojima and Takeshi Yamamoto.

REFERENCES

1. Watanabe, R., et al., *Research of the Relationship of Pedestrian Injury to Collision Speed, Car-type, Impact Location and Pedestrian Sizes using Human FE model (THUMS Version 4)*. Stapp Car Crash Journal, 2012. **56**: p. 269-321.
2. Kato, D., et al. *Development of Human-Body Model THUMS Version 6 containing Muscle Controllers and Application to Injury Analysis in Frontal Collision after Brake Deceleration*. in IRCOBI. 2018.
3. Zhao, J., et al., *A Human Body Model Study on Restraints for Side-Facing Occupants in Frontal Crashes of an Automated Vehicle*. SAE Technical Paper, 2020. **2020-01-0980**.
4. A, Piqueras-Lorente, et al. *Kinematic Assessment of Subject Personification of Human Body Models (THUMS)*. in IRCOBI Conference. 2018.
5. T, A., K. Y, and E. A. *Influence of Posture Adjustment Methods for Human Body Models on Injury Prediction*. in IRCOBI Conference. 2019.
6. Costa, C., et al. *Effect of Postural Adjustment Methods on Mesh Quality and Simulation Time of Human Body Models*. in IRCOBI. 2021.
7. Klein, C., et al., *A Method for Reproducible Landmark-based Positioning of Multibody and Finite Element Human Models*, in IRCOBI. 2021.
8. Puta, I., et al., *Comparison of control strategies for the cervical muscles of an average female head-neck finite element model*. Traffic injury and prevention, 2019. **20**(52): p. S116-S122.
9. *2010 Toyota Yaris Finite Element Model Validation Detail Mesh*. 2016, George Mason University: Center for Collision Safety and Analysis.
10. *THUMS User Manual*. 2010.
11. Reed, M.P., et al., *A Statistical Model for Predicting Automobile Driving Posture*. Human Factors, 2002. **44**(4): p. 557-568.
12. Reed, M.P., S.M. Ebert, and M.L.H. Jones, *Posture and belt fit in reclined passenger seats*. Traffic injury and prevention, 2019. **20**(S1): p. S38-S42.
13. Verver, M., et al., *Aspects of seat modeling for seat comfort analysis*. Applied Ergonomics, 2005. **36**: p. 33-42.
14. Yoon, S. and A. Delevoeye, *A Study on the Coefficient of Dynamic Friction between Dummy and Seat by Test Method*, in IRCOBI. 2016: Asia. p. 90-91.
15. Kothari, V. and M. Gangal, *Assessment of frictional properties of some woven fabrics*. Indian Journal of Fibre & Textile Research, 1994. **19**: p. 151-155.
16. Patten, W., S. Sha, and C. Mo, *A Vibration Model of Open Celled Polyurethane Foam Automotive Seat Cushions*. Journal of Sound and Vibration, 1998. **217**(1): p. 145-161.
17. Arbogast, K., et al., *The effect of pretensioning and age on torso rollout in restrained human volunteers in far-side lateral and oblique loading*. Stapp Car Crash Journal, 2012. **56**: p. 443-467.
18. Seacrist, T., et al., *Evaluation of pediatric ATD biofidelity as compared to child volunteers in low-speed far-side oblique and lateral impacts*. Traffic injury and prevention, 2014. **15**(Suppl 1): p. S206-214.
19. Siegmund, G., D. Sanderson, and J. Inglis, *The effect of perturbation acceleration and advance warning on the neck postural responses of seated subjects*. Experimental Brain Response, 2002. **114**(3): p. 314-321.

INVESTIGATION ON EFFECTIVE APPROACHES OF BRAIN FE MODELING TO IMPROVE ITS VALIDATION PERFORMANCE ON BRAIN DEFORMATION DURING HEAD IMPACT

Noritoshi Atsumi

Yuko Nakahira

Masami Iwamoto

Toyota Central R&D Labs., Inc.

Japan

Paper Number 23-0094

ABSTRACT

The finite element (FE) model of the human brain is an effective tool for predicting brain strain during head impacts that can result in traumatic brain injury (TBI). Although many brain FE models have been proposed and updated upon thus far, it was unclear what kind of modeling approaches would critically contribute to improving the biofidelity of the models. This study investigated whether the implementation of material anisotropy of the brain tissue or the appropriate representation of the boundary conditions around the ventricle would affect the validation performance of modeling brain deformation during head impact. Axonal fiber tracts of the whole brain were extracted from diffusion-weighted images in the Amsterdam Open MRI Collection using tractography. The direction of the material axis in each element of the white matter of the previously developed human brain FE model was determined based on axonal fiber tracts. Incompressible fluid dynamics (ICFD), including perfusion pressure, was also applied to the intraventricular cerebrospinal fluid (CSF) of the model. Validation of the displacement and strain in the brain during head impact was performed based on cadaveric test data, wherein quantitative evaluation of validation accuracy was conducted using the CORrelation and Analysis (CORA) method. The CORA scores of the model were compared with those of the model with isotropic material or those of the model without ICFD. The difference in CORA scores for brain displacement was minimal among the models. On the other hand, the CORA scores for brain strain of the model with ICFD were higher than those without ICFD. However, CORA scores for the brain strain of the anisotropic model based on the axonal fiber tracts were similar to or lower than those of the isotropic model. Comparing CORA scores among the models indicated that introducing ICFD to the intraventricular CSF improved the validation performance of the brain FE model. However, implementing anisotropy of the white matter based on tractography at the element level does not necessarily improve the validation performance of the brain FE model. In addition, evaluating the validation accuracy of the brain FE model using brain displacement did not reflect the difference in the accuracy of predicting brain strain during head impact. A limitation of this study includes the spatial registration of axonal fiber tracts with the FE model using affine transformation. It would be more desirable to consistently conduct FE modeling and tract extraction so that the differences in brain geometry and axonal fiber pathways for each subject could be considered. The findings in this study indicate that the appropriate representation of the boundary condition around the ventricle using ICFD would affect the validation performance on the brain strain in the brain FE model rather than the accuracy of the description of the anisotropy at the element level. These findings may provide useful insights into modeling strategies of the human brain to predict TBI due to head impact associated with traffic accidents.

INTRODUCTION

Mild traumatic brain injury (mTBI) or concussions account for approximately 80% of traumatic brain injury (TBI) incidents, which can result from a numerous causes, including blunt trauma caused by falls, vehicular accidents, and collisions experienced in sports-related activities associated with angular acceleration of the head [1, 2]. As mTBI requires careful treatment and incurs large healthcare costs [3, 4], predicting and preventing the occurrence of mTBI in such situations is important.

The finite element (FE) model of the human brain is an effective tool for predicting deformations of brain tissues or axons during head impact. Many human brain FE models have been developed and continually updated in recent years [5–11]. Several strategies for improving the biofidelity of the human brain FE model comprise refining the representation of the anatomical structure, including the gyrus or limbic system; application of the constitutive model describing the anisotropy and viscoelasticity of the brain tissue; explicit implementation of the axonal fiber tracts; and consideration of the dynamics of the intracranial cerebrospinal fluid (CSF). However, it was unclear what kind

of modeling approaches would critically contribute to improving the biofidelity of the brain FE model. In addition, despite the suggested possibility of using brain or axonal strain to predict mTBI [5, 12–14], only a few models provide their validation performance with respect to the brain strain during head impact [8, 9, 11].

In this study, the axonal fiber orientation extracted from tractography was applied in the direction of the material axis in a previously developed human brain FE model [15]. By comparing the validation scores to those of the brain FE model and considering intraventricular fluid dynamics using incompressible fluid dynamics (ICFD) [11], we investigated whether the implementation of material anisotropy of brain tissue or the appropriate representation of the boundary conditions around the ventricle may affect the validation accuracy of the brain deformation.

MATERIALS AND METHODS

Extraction of Axonal Fiber Tracts

Diffusion-weighted images (DWI) and T1-weighted images (T1WI) required for the extraction of axonal fiber tracts were obtained from the pre-processed Amsterdam Open MRI Collection (AOMIC) dataset [16]. The spatial resolution of DWI is $2.0 \times 2.0 \times 2.0 \text{ mm}^3$, whereas that of T1WI is $1.0 \times 1.0 \times 1.0 \text{ mm}^3$. The b-values of DWI, which represent the diffusion intensity, were 0 and $1,000 \text{ s/mm}^2$. These two values are required to separate the white matter tissue from the rest of the brain compartment in DWI using the difference in the response functions of fiber orientation distribution. Based on the published tutorials of tractography [17], MRtrix v3.0.0 [18, 19] and dependent software, including FSL (FMRIB Software Library) [20], FreeSurfer [21], and Advanced Normalization Tools (ANTs) [22] were utilized to extract two million axonal fiber tracts across the whole brain. After extracting the tracts of the whole brain, structural connectivity was derived for each subject based on the number of axonal fiber tracts. Structural connectivity refers to the degree of connection between any two regions, when the cortical and subcortical parts of the whole brain are divided into several functional and anatomical regions. Ideally, the average tract data across the subjects should be introduced into the brain FE model. However, as the geometry of the brain differs among subjects and the extracted axonal fiber tracts are specific to each subject, deriving average tracts were not possible. Therefore, in this study, the subject with the smallest variance in structural connectivity was selected from all the subjects ($n = 216$) in the AOMIC dataset. Figure 1 shows the axonal fiber tracts extracted from the DWI data of the selected subject, in which the T1WI was overlaid; only a representative 20,000 tracts out of two million tracts are shown.

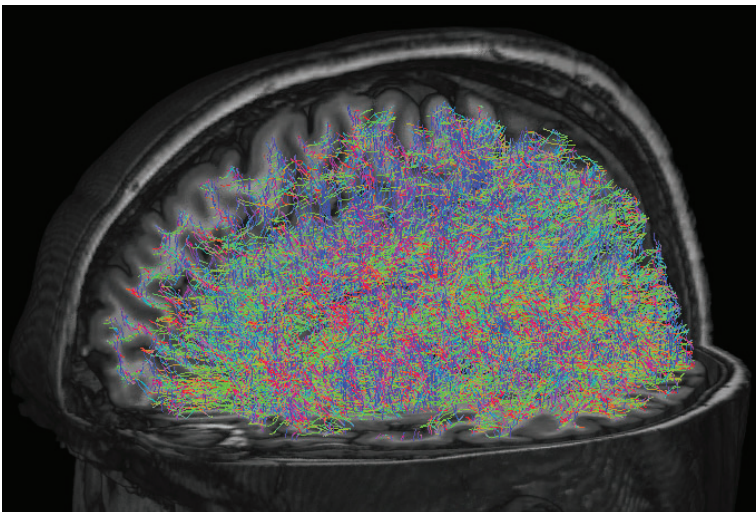


Figure 1. Axonal fiber tracts (color) extracted from DWI with overlaid T1WI (grayscale). Only a representative 20,000 tracts are shown here.

Human Brain FE Model

A previously developed human brain FE model [11, 15] was used in this study. The left side of Figure 2 shows an overview of the model. The model has a well-described anatomical structure, including the cerebrum, corpus callosum, thalamus, basal ganglia, fornix, cerebellum, dura mater, falx, tentorium, midbrain, pons, and medulla oblongata using hexahedral solid elements. The pia mater and arachnoid were modeled using shell elements. The model contained 48,313 solid elements and 13,032 shell elements. The interface between the brain and dura mater was modeled using a layer of solid elements with shared nodes.

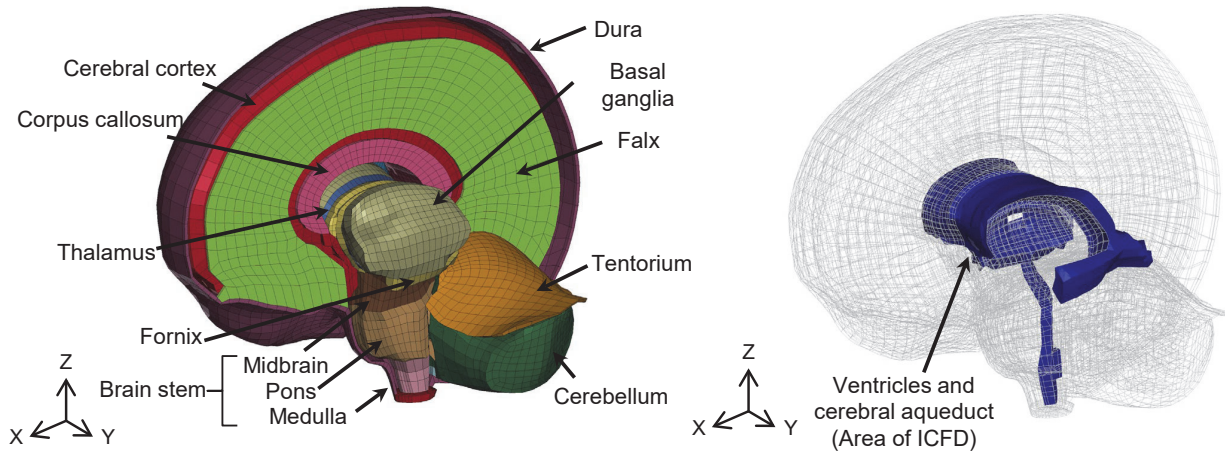


Figure 2. (left) Human brain FE model used in this study. (right) The area in which ICFD was applied.

The material properties in each part of the brain FE model followed those of the previous model [11]. A constitutive model utilized in the brain parenchyma appropriately describes the anisotropy in white matter, strain-rate dependency, and characteristic features of the unloading process [15, 23]. In this study, the material axes in each solid were determined based on the orientation of the extracted axonal fiber tracts. First, the coordinates of each fiber tract were obtained at 1 mm intervals using *tckresample* and *tckconvert* commands in MRtrix. Then, spatial registration of the coordinates of the tracts toward FE model was performed using affine transformation. As the DWI obtained from the AOMIC dataset covered the brainstem and cerebellum incompletely, the tracts in these regions were interrupted in the middle. Therefore, affine transformation was applied to align the outermost points of the top, bottom, left, right, front, and rear, based on the coordinates of tracts belonging to the cerebral part. An overview of axonal fiber tracts registered with the brain FE model is shown in the left part of Figure 3. Next, each vector of the registered tracts was checked if it had passed through each solid element of the cerebral part of the FE model. The average value of the vectors to be passed then was set as the material axis of the solid element. The right side of Figure 3 shows a conceptual diagram of the procedure. It is not possible to distinguish the starting or ending side from the extracted axonal fiber tracts. Therefore, even if the axial directions of the tracts are similar, they may cancel each other when averaged, depending on the direction of the vectors. To address this, the directions of each vector were unified based on the following equations:

$$\mathbf{v} = \begin{cases} \mathbf{v} & (\text{prod}(\mathbf{v}) \geq 0) \\ -\mathbf{v} & (\text{prod}(\mathbf{v}) < 0) \end{cases} \quad \text{Equation (1)}$$

The symbol \mathbf{v} is a three-dimensional vector corresponding to the direction of the tracts. Function $\text{prod}(\cdot)$ derives the product of the vector components. The material axes for each element are defined using the keyword `*ELEMENT_SOLID_ORTHO` in LS-DYNA (LSTC, USA).

To introduce fluid dynamics into the intraventricular CSF, the ICFD option of LS-DYNA was used, as in a previous study [11]. ICFD was applied to the lateral ventricle, third ventricle, fourth ventricle, and cerebral aqueduct of the brain FE model, indicated in blue in the right part of Figure 2. When a closed space is provided by surface shell elements defined as the boundary, the ICFD solver in LS-DYNA automatically generates a fluid volume mesh inside

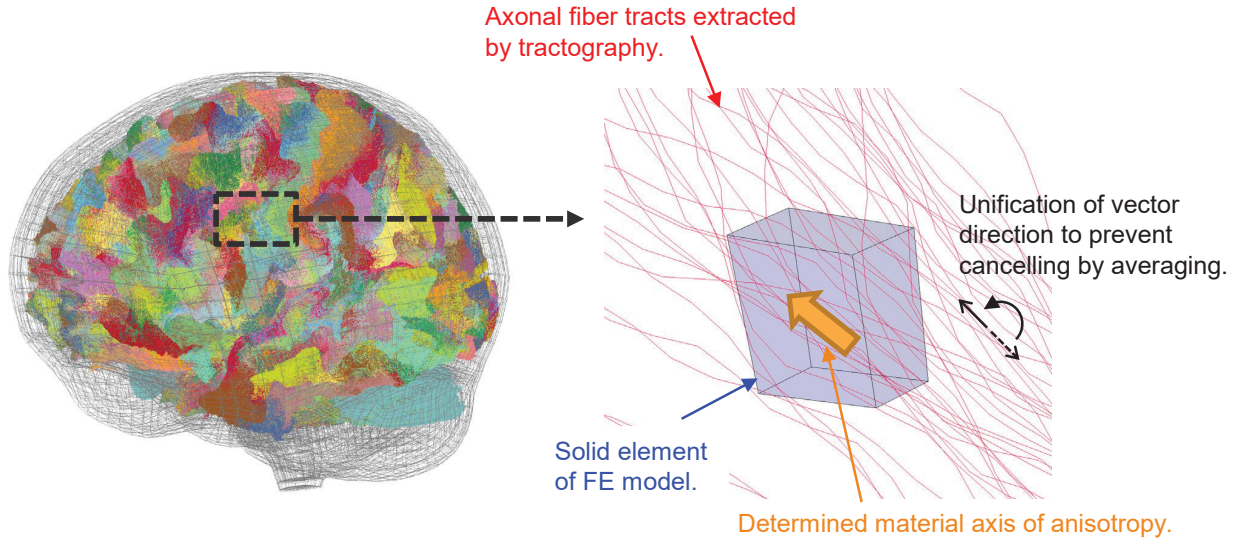


Figure 3. (left) Axonal fiber tracts registered with the brain FE model. (right) Determination of the material axis of each solid element.

the space at the start of the analysis. The boundary condition between the fluid and structure was a non-slip condition, and three boundary layer meshes were defined. In addition, intracranial perfusion pressure was considered. Based on the experimental setting in the PMHS test performed by Hardy et al. [24], an initial pressure of 10.3 kPa was applied to the area of ICFD. The fluid-structural interaction was solved in a weak coupling, that is, the solid and fluid solvers separately proceeded with the calculations using individual time steps, and the interpolated displacements and forces at the boundary between the structure and fluid were passed to each other [25]. The time step for solving the ICFD was 1.0×10^{-5} s, whereas that for the structure was 8.96×10^{-8} s in this study. All FE analyses were conducted using the LS-DYNA R11.1.0 SMP with double precision.

Validation Setting

The validation protocol of the FE model followed that of a previous study [11]. PMHS test data on brain deformation during head impacts, which were originally obtained by Hardy et al. [24] and subsequently reanalyzed with respect to the strain calculation by Zhou et al. [26, 27], were used. Three representative tests were performed. C288-T3 was an occipital impact test resulting in forward rotation of the head with a peak angular acceleration of 24.2 krad/s^2 (Figure 4(a)). C380-T1 was a parietal impact test resulting in right lateral flexion with a peak angular acceleration of 5.1 krad/s^2 (Figure 4(b)). C380-T2 was an occipital impact test resulting in the left rotation of the head with a peak angular acceleration of 5.1 krad/s^2 (Figure 4(c)). In these experiments, the displacements of each of the seven neural density targets (NDT) in the two clusters (C1 and C2) embedded in the head of the PMHS with respect to its center of gravity (CG) were measured using a high-speed biplanar X-ray system during head impact [24]. The cluster strain was calculated from the relative displacements of the NDTs in each cluster. To simulate the experiments, a cluster model comprising eight tetrahedral elements was prepared (Figure 4(d)) First, simulations for each case using the brain FE model were performed to calculate the displacements of the nodes closest to each NDT. Subsequently, the history of the displacements of the nodes was input to the corresponding NDT in the cluster model. Finally, the cluster strain was calculated by averaging the Green–Lagrange strain of each element in the cluster model. The four tetrahedral elements in C2 were not included in the cluster strain calculations for C380-T1 and C380-T2 because of lack of data for the 9th NDT of C2.

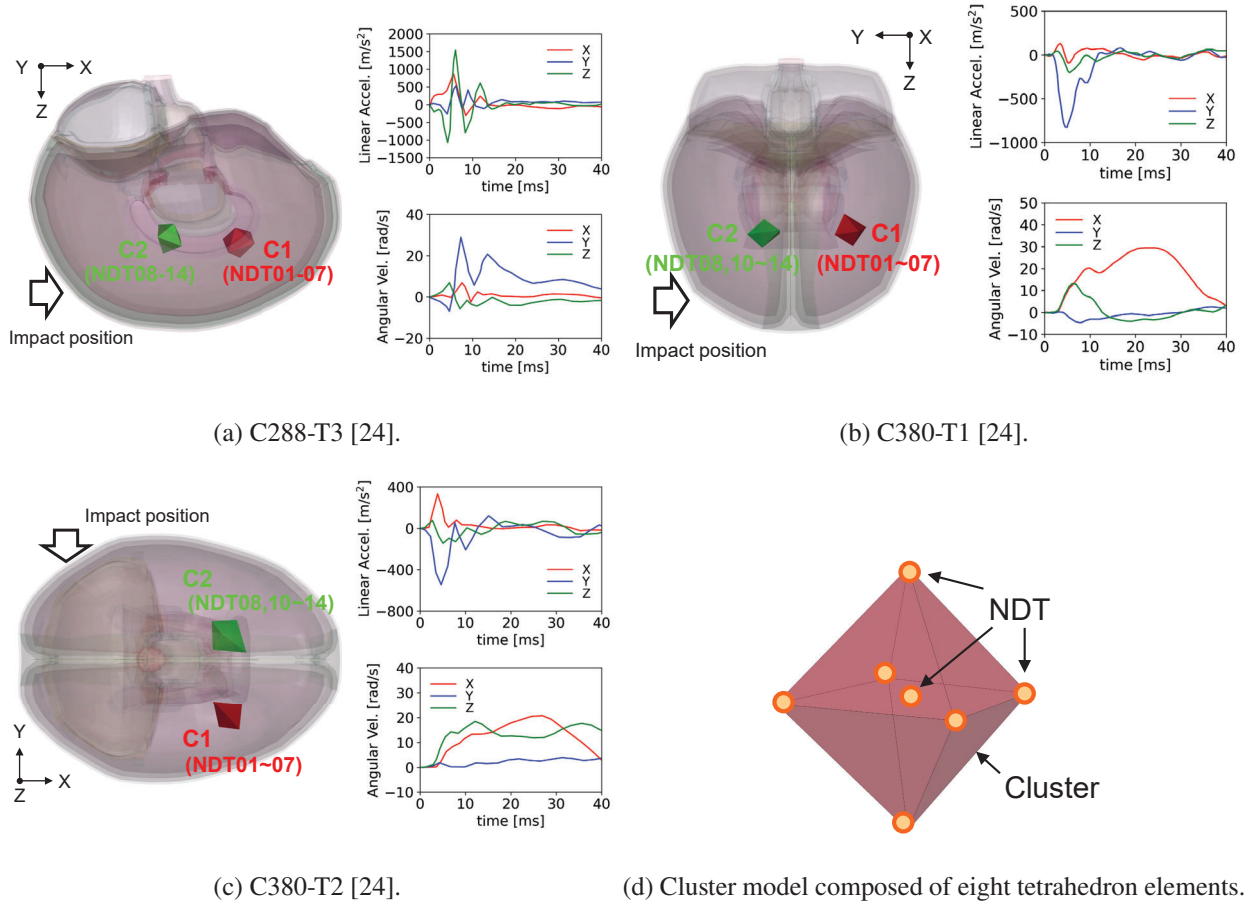


Figure 4. Validation setting.

To compare the influence of different modeling approaches on the validation results, four different models shown in Table 1 were prepared. In Models A and B, the constitutive model with isotropic parameters, which was identified against gray matter, was also applied to white matter. On the other hand, the anisotropic constitutive model was utilized for the white matter in Models C and D following the introduction of the axonal fiber tracts as the direction of material axis described above. The intraventricular CSF in Models A and C was modeled using viscoelastic solid elements according to Mao et al. [6], whereas those in Models B and D were described using ICFD with perfusion pressure based on a previous study [11].

Table 1.
List of models compared in this study.

	Material property of brain parenchyma	Modeling approach of intraventricular CSF
Model A	isotropic	viscoelastic solid elements [6]
Model B	isotropic	ICFD with perfusion pressure [11]
Model C	anisotropic based on tracts	viscoelastic solid elements [6]
Model D	anisotropic based on tracts	ICFD with perfusion pressure [11]

The validation results of the displacements of NDTs and the strain of each cluster were quantitatively evaluated based on the CORrelation and Analysis (CORA) method [28, 29]. The CORA method assesses the degree of correlation between a pair of time-history curves using two sub-methods: the corridor method and the correlation method. However, the corridor method was not activated, and the recommended setting was used in this study, referring to the work of Giordano and Kleiven [30]. The CORA score ranges from 0 to 1, with closer to 1 indicating a better match.

The sliding scales of CORA are defined as follows: “Unacceptable”:0.0-0.26, “Marginal”:0.26-0.44, “Fair”:0.44-0.65, “Good”:0.65-0.86, “Excellent”:0.86-1.0 [31].

RESULTS

As a typical result, comparisons of the histories of the displacements in NDTs belonging to each cluster for C380-T1 between the experimental data [24] and the simulation results using the brain FE models were shown in Figures 5 and 6, respectively (for C288-T3 and C380-T2, see Figures A1-A4 in Appendix). The displacements in the direction of the X-axis in NDT01, 05, 06, Y-axis in NDT01, 04-06, 12, and Z-axis in NDT06, 08-14 of Models B and D were larger than those of Models A and C. However, no noticeable difference in the overall trends of the displacement of NDTs was observed among the models.

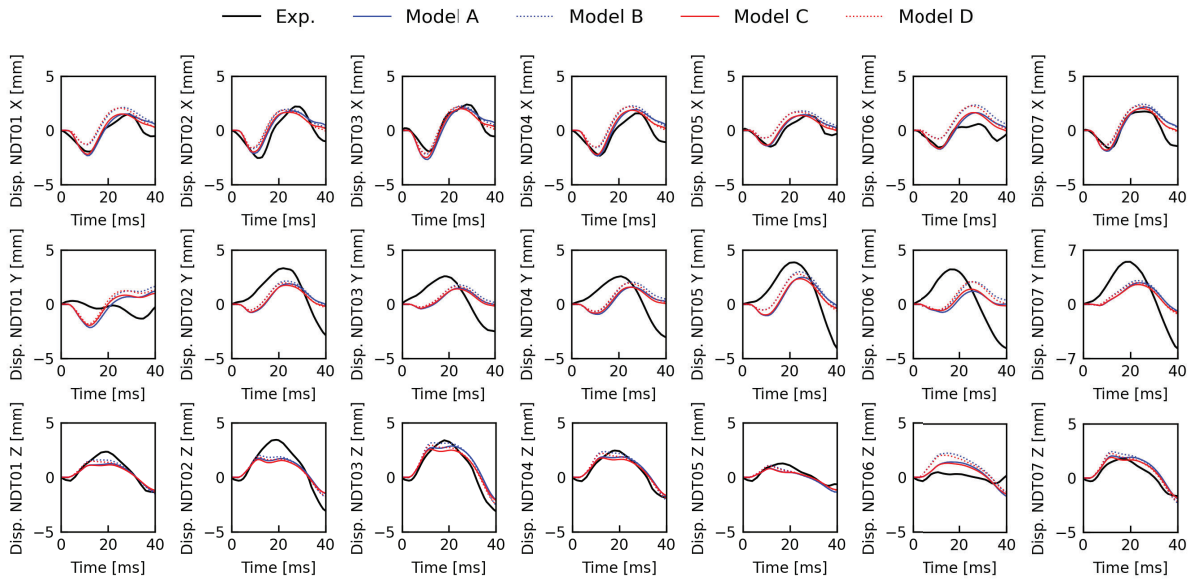


Figure 5. Comparisons of the histories of displacements in NDTs belonging to C1 for C380-T1 between the PMHS test data [24] and the simulation results.

Figure 7 shows the comparisons of the histories of the maximum principal strain (MPS) and maximum shear strain (MSS) in both clusters for C380-T2 between the reanalyzed data [27] and simulation results using the brain FE models (for C288-T3 and C380-T1, see Figures A5 and A6 in the Appendix). The peak strain values in C1 were higher for Models B, A, D, and C, in this order. In contrast, for C2, the order was Models B, D, A, and C. In addition, Models A and C and Models B and D had similar waveforms in both clusters.

Tables 2 and 3 show comparisons of the CORA scores on the displacement of NDTs and strain in clusters for each test, respectively. The values indicated in Table 2 are the average scores of displacements in the 14 NDTs of both clusters, whereas those in Table 3 are the average scores of MPS and MSS in both clusters. For comparison, the CORA scores reported by Li et al. [8], who proposed a detailed and personalizable (ADAPT) head model, are also provided in these tables. From Table 2, the scores on the displacements in NDTs for C380-T1 and C380-T2 were almost equivalent among the four brain FE models. The scores on the displacements in NDTs for C288-T3 using Models B and D were slightly higher than those using Models A and C. However, the difference in scores was insufficient to cross the sliding scale of CORA. The CORA scores for the NDT displacements in this study were comparable to those in the ADAPT head model [8].

Conversely, the CORA scores on the strain of the clusters varied considerably among the models, as shown in Table 3. Model C resulted in the lowest CORA scores in all the tests. For C380-T1 and C380-T2, the CORA scores for the cluster strain in Models A, B, and D were almost equivalent. In contrast, the scores for C288-T3 using Models B and D were higher than those using Models A and C. The highest average score of CORA in the three tests was found in

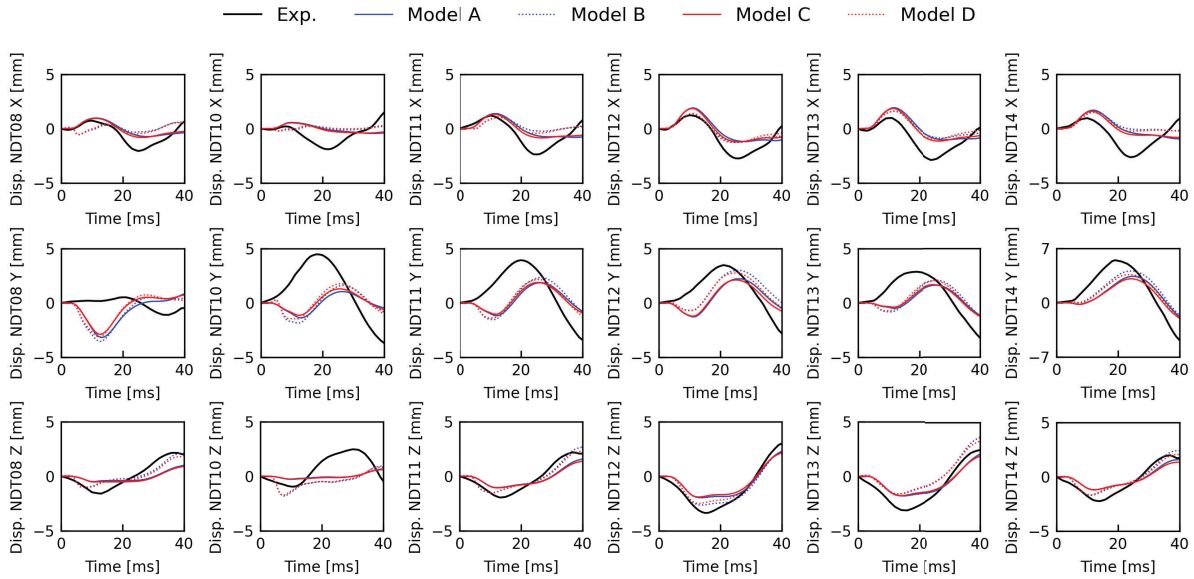


Figure 6. Comparisons of the histories of displacements in NDTs belonging to C2 for C380-T1 between the PMHS test data [24] and the simulation results.

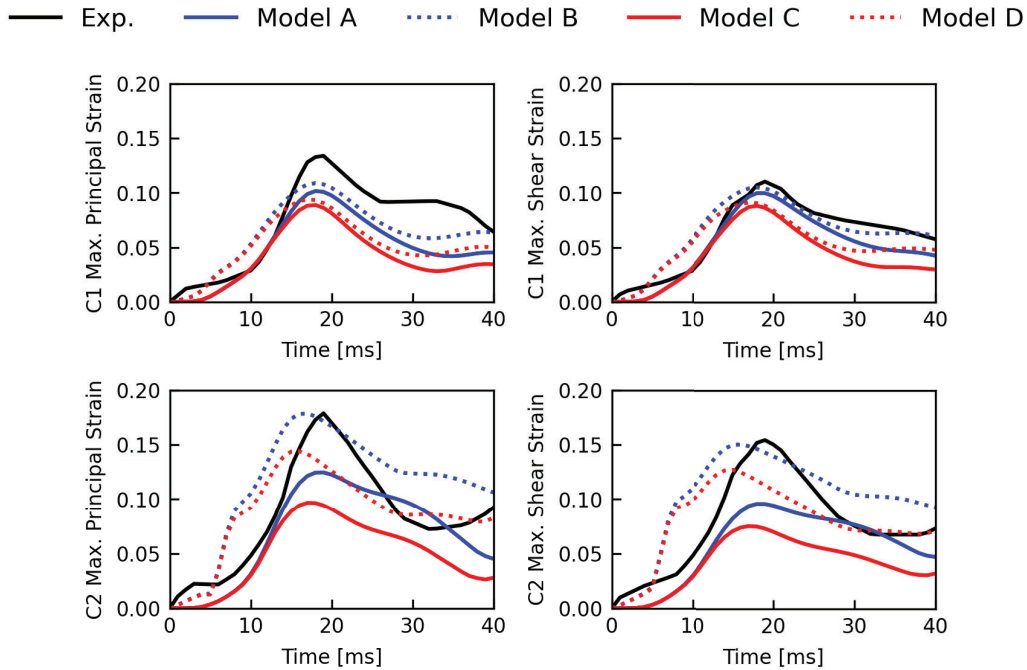


Figure 7. Comparisons of the histories of strain in C1 and C2 for C380-T2 between the PMHS test data [24, 27] and the simulation results.

Model D. In C288-T3 and C380-T2, the CORA scores for the cluster strain in Models B and D were higher than those in the ADAPT head model [8].

Table 2.
Comparisons of averaged CORA score on the displacement of all NDTs.

	Model A	Model B	Model C	Model D	ADAPT [8]
C288-T3	0.574 (Fair)	0.634 (Fair)	0.565 (Fair)	0.620 (Fair)	0.588 (Fair)
C380-T1	0.676 (Good)	0.688 (Good)	0.688 (Good)	0.694 (Good)	0.694 (Good)
C380-T2	0.558 (Fair)	0.571 (Fair)	0.538 (Fair)	0.550 (Fair)	0.549 (Fair)
Ave.	0.603	0.631	0.597	0.621	0.610

Table 3.
Comparisons of averaged CORA score on the strain of both clusters.

	Model A	Model B	Model C	Model D	ADAPT [8]
C288-T3	0.648 (Fair)	0.904 (Excellent)	0.626 (Fair)	0.890 (Excellent)	0.742* (Good)
C380-T1	0.820 (Good)	0.809 (Good)	0.751 (Good)	0.836 (Good)	0.877* (Excellent)
C380-T2	0.866 (Excellent)	0.900 (Excellent)	0.779 (Good)	0.904 (Excellent)	0.793* (Good)
Ave.	0.778	0.871	0.719	0.877	0.804

* Averaged scores of MPS and MSS only from C1 for ADAPT model.

DISCUSSION

This study provides quantitative comparisons of validation performance on the displacement and strain in the brain among the brain FE models based on different modeling approaches with respect to the anisotropy of the brain tissue and boundary conditions around the ventricle. As shown in Table 2, the CORA scores for NDT displacement were almost equivalent among the models. In other words, both the implementation of the material axis in the brain tissue based on the axonal fiber tracts and the application of ICFD to the intraventricular CSF had minimal effect on the validation performance of the displacement in the brain. However, as shown in Table 3, the application of ICFD resulted in improved CORA scores on cluster strain. This trend is consistent with that reported in a previous study [11]. However, implementing the material axis based on axonal fiber tracts with the present method does not necessarily improve the CORA scores on cluster strain. These findings suggest that the appropriate representation of the boundary condition around the ventricle using ICFD affects the validation performance of strain in the brain more than the accuracy of the description of anisotropy at the element level. In addition, evaluating the validation performance of the brain FE model using NDT displacements could not reflect the difference in the accuracy of predicting brain strain during head impact. This is consistent with findings in previous studies that validation solely based on relative brain–skull displacements does not infer biofidelity of strain in the model [9] and that validation against brain strain data is recommended [8, 9].

To describe the material axis of anisotropy in the white matter, previous studies have provided methods that apply fractional anisotropy (FA) values extracted from diffusion tensor images (DTI) to the brain FE model [7, 14, 32, 33]. These methods can implement the distribution of the degree of anisotropy in the whole brain because the constitutive models in their studies include parameters associated with the FA value. However, the validation of these models was performed only against the displacement of the brain tissue, and it was unclear whether the implementation of anisotropy actually contributed to improving the validation performance on brain strain. As the constitutive model of the brain parenchyma used in this study did not include the parameter associated with the FA value, the current study only determined the directions of the material axis in each element of the white matter based on the axonal fiber tracts extracted using tractography. Nevertheless, even if we introduce a parameter that describes the distribution of the degree of anisotropy into the current constitutive model, the material properties in regions where the number of axonal fibers is relatively small would only approach isotropic. Considering the current result that the difference in CORA values due to the implementation of ICFD is larger than that due to anisotropy, it can be inferred that the effect of introducing DTI-based FA distribution on the improvement in validation performance of the brain strain will be smaller than the contribution of the boundary condition.

A possible reason why the introduction of anisotropy based on tractography did not improve the validation performance of the brain strain is that the reduction to the element level does not represent the mechanical properties of axonal fibers continuously leading across the brain parenchyma. Recently, Zhou et al. [34] stated that downsampling process in the introduction of the axonal fiber direction extracted from DTI into the FE models could cause some loss of fiber orientation information in each voxel, which compromised the accuracy of tract-related strain, particularly for the model including resolution mismatch between the mesh and voxel. Although their approach did not include the mechanical influence of axons on the deformation of solid elements because the axons were modeled using null material [34], their suggestion would be consistent with the findings of the current study. In other words, the reduction of the extracted tracts to the element level could result in a reduction in the effect of the directional distribution of individual axons on the local deformation of the brain parenchyma.

Another way to introduce axonal fiber tracts into the brain FE model is to implement the tracts explicitly as one-dimensional beam elements embedded in the solid elements proposed by Garimella et al. [35] and Wu et al. [36]. This approach has the potential to achieve a more detailed prediction of mTBI by computing the strain on the axonal fiber itself and associating it with functional impairments in the brain. However, in this approach, the beam and solid elements in the cerebral part of the model represent neurons and surrounding glial cells, respectively. Thus, determining the material parameters and assigning the mass distribution in each part are key issues in properly predicting the local deformation in the brain.

A limitation of this study is related to the procedure of registration of the extracted axonal fiber tracts into the brain FE model. As in a previous study [7], the registration between them was simply performed using an affine transformation. Thus, the FE model and extracted fiber tracts were each based on data from different subjects. Li et al. [8] proposed a morphing approach using a hierarchical image registration pipeline to develop a subject-specific brain FE model that consistently accounts for the geometry and corresponding axonal fiber tracts in the individual brain. Such a modeling approach would be effective for better evaluation of individual mTBIs. Another limitation is the modeling approach for the interface between the brain and dura mater so-called pia-arachnoid complex (PAC) layer, which consists of the arachnoid trabeculae and CSF. In this study, the PAC layer was modeled by not applying ICFD but using viscoelastic solid elements with shared nodes, following previous research [11]. Further experimental or numerical studies are needed to investigate the influence of CSF behavior and perfusion pressure in the PAC layer on brain deformation, thus validating the performance of the brain FE models.

CONCLUSIONS

In this study, we examined the effectiveness of the implementation of the material axis based on the axonal fiber tracts and fluid dynamics of CSF using ICFD on the validation performance of brain deformation in the brain FE model. The results suggested that the appropriate representation of boundary conditions around the ventricle, including ICFD, would affect the validation performance of strain in the brain more than the accuracy of the description of anisotropy at the element level. In addition, evaluating the validation performance of the brain FE model using NDT displacements does not necessarily guarantee the validation accuracy to predict brain strain during head impact. The findings of this study would provide useful insights into modeling strategies of the brain FE model for better prediction of mTBI.

ACKNOWLEDGMENTS

We thank Dr. Hiroyuki Sakai for valuable advice in introducing tractography. We also thank Editage (www.editage.jp) for English language editing.

REFERENCES

- [1] Smith, D.H., Nonaka, M., Miller, R., Leoni, M., Chen, X.H., Alsop, D., & Meaney, D.F. 2000. "Immediate coma following inertial brain injury dependent on axonal damage in the brainstem". *J. Neurosurg.*, Vol. 93, pp. 315–322.
- [2] Narayana, P.A. 2017. "White matter changes in patients with mild traumatic brain injury: MRI perspective". *Concussion*, Vol. 2, pp. CNC35.
- [3] Miller, G.F., DePadilla, L., & Xu, L. 2021. "Costs of nonfatal traumatic brain injury in the United States, 2016". *Med. Care*, Vol. 59, pp. 451–455.

- [4] Shinoda, J. & Asano, Y. 2013. “Neuroimaging of patients with impairments of executive brain function due to traumatic brain injury”. *Japanese J. Neurosurg.*, Vol. 22, pp. 842–848.
- [5] Kleiven, S. 2007. “Predictors for traumatic brain injuries evaluated through accident reconstructions.”. *Stapp Car Crash J.*, Vol. 51, pp. 81–114.
- [6] Mao, H., Zhang, L., Jiang, B., Genthikatti, V.V., Jin, X., Zhu, F., Makwana, R., Gill, A., Jandir, G., Singh, A., & Yang, K.H. 2013. “Development of a Finite Element Human Head Model Partially Validated With Thirty Five Experimental Cases”. *J. Biomech. Eng.*, Vol. 135, pp. 111002.
- [7] Sahoo, D., Deck, C., & Willinger, R. 2014. “Development and validation of an advanced anisotropic visco-hyperelastic human brain FE model”. *J. Mech. Behav. Biomed. Mater.*, Vol. 33, pp. 24–42.
- [8] Li, X., Zhou, Z., & Kleiven, S. 2021. “An anatomically detailed and personalizable head injury model: Significance of brain and white matter tract morphological variability on strain”. *Biomech. Model. Mechanobiol.*, Vol. 20, pp. 403–431.
- [9] Zhao, W. & Ji, S. 2020. “Displacement- and Strain-Based Discrimination of Head Injury Models across a Wide Range of Blunt Conditions”. *Ann. Biomed. Eng.*, Vol. 48, pp. 1661–1677.
- [10] Zhou, Z., Li, X., & Kleiven, S. 2020. “Biomechanics of Periventricular Injury”. *J. Neurotrauma*, Vol. 37, pp. 1074–1090.
- [11] Atsumi, N., Nakahira, Y., & Iwamoto, M. 2021. “Human brain FE modeling including incompressible fluid dynamics of intraventricular cerebrospinal fluid”. *Brain Multiphysics*, Vol. 2, pp. 100037.
- [12] Viano, D.C., Casson, I.R., Pellman, E.J., Zhang, L., King, A.I., & Yang, K.H. 2005. “Concussion in professional football: brain responses by finite element analysis: part 9”. *Neurosurg.*, Vol. 57, pp. 891–916.
- [13] Sahoo, D., Deck, C., & Willinger, R. 2015. “Axonal strain as brain injury predictor based on real-world head trauma simulations”, *Proceedings of the IRCOBI conference.* , No. IRC-15-30, pp. 186–197.
- [14] Giordano, C. & Kleiven, S. 2014. “Evaluation of Axonal Strain as a Predictor for Mild Traumatic Brain Injuries Using Finite Element Modeling”. *Stapp Car Crash J.*, Vol. 58, pp. 29–61.
- [15] Atsumi, N., Nakahira, Y., Tanaka, E., & Iwamoto, M. 2018. “Human brain modeling with its anatomical structure and realistic material properties for brain injury prediction”. *Ann. Biomed. Eng.*, Vol. 46, pp. 736–748.
- [16] Snoek, L., van der Miesen, M.M., Beemsterboer, T., van der Leij, A., Eigenhuis, A., & Steven Scholte, H. 2021. “The Amsterdam Open MRI Collection, a set of multimodal MRI datasets for individual difference analyses”. *Scientific Data*, Vol. 8, pp. 1–23.
- [17] “B.A.T.M.A.N.: Basic and Advanced Tractography with MRtrix for All Neurophiles”. <https://osf.io/fkyht/>.
- [18] “MRtrix3”. <https://www.mrtrix.org/>.
- [19] Tournier, J.D., Smith, R., Raffelt, D., Tabbara, R., Dhollander, T., Pietsch, M., Christiaens, D., Jeurissen, B., Yeh, C.H., & Connelly, A. 2019. “MRtrix3: A fast, flexible and open software framework for medical image processing and visualisation”. *NeuroImage*, Vol. 202, pp. 116137.
- [20] “FSL (FMRIB Software Library)”. <https://fsl.fmrib.ox.ac.uk/fsl/fslwiki>.
- [21] “FreeSurfer”. <https://surfer.nmr.mgh.harvard.edu/>.
- [22] “ANTs (Advanced Normalization Tools)”. <http://stnava.github.io/ANTs/>.
- [23] Atsumi, N., Nakahira, Y., Iwamoto, M., Hirabayashi, S., & Tanaka, E. 2016. “Constitutive Modeling of Brain Parenchyma Taking Account of Strain Rate Dependency with Anisotropy and Application to Brain Injury Analyses”, *SAE Tech. Pap.* , No. 2016-01-1485.
- [24] Hardy, W.N., Mason, M.J., Foster, C.D., Shah, C.S., Kopacz, J.M., Yang, K.H., King, A.I., Bishop, J., Bey, M., Anderst, W., & Tashman, S. 2007. “A study of the response of the human cadaver head to impact.”. *Stapp Car Crash J.*, Vol. 51, pp. 17–80.

- [25] Livermore Software Technology Corporation (LSTC). 2014. “ICFD theory manual: Incompressible fluid solver in LS-DYNA”.
- [26] Zhou, Z., Li, X., Kleiven, S., Shah, C.S., & Hardy, W.N. 2018. “A Reanalysis of Experimental Brain Strain Data: Implication for Finite Element Head Model Validation”. *Stapp Car Crash J.*, Vol. 62, pp. 293–318.
- [27] Zhou, Z., Li, X., Kleiven, S., & Hardy, W.N. 2019. “Brain Strain from Motion of Sparse Markers”. *Stapp Car Crash J.*, Vol. 63, pp. 1–27.
- [28] Gehre, C., Gades, H., & Wernicke, P. 2009. “Objective rating of signals using test and simulation responses”, *Proceedings of the 21th ESV Conference.* , No. 09-0407.
- [29] Gehre, C. & Stahlschmidt, S. 2011. “Assessment of dummy models by using objective rating methods”, *Proceedings of the 22nd ESV Conference.* , No. 11-0216.
- [30] Giordano, C. & Kleiven, S. 2016. “Development of an Unbiased Validation Protocol to Assess the Biofidelity of Finite Element Head Models used in Prediction of Traumatic Brain Injury”. *Stapp Car Crash J.*, Vol. 60, pp. 363–471.
- [31] The International Organization for Standardization (ISO). 1999. “Road vehicles — Anthropomorphic side impact dummy — Lateral impact response requirements to assess the biofidelity of the dummy”, *ISO/TR 9790:1999.*
- [32] Wright, R.M. & Ramesh, K.T. 2012. “An axonal strain injury criterion for traumatic brain injury”. *Biomechanics and Modeling in Mechanobiology*, Vol. 11, pp. 245–260.
- [33] Ganpule, S., Daphalapurkar, N.P., Ramesh, K.T., Knutsen, A.K., Pham, D.L., Bayly, P.V., & Prince, J.L. 2017. “A Three-Dimensional Computational Human Head Model That Captures Live Human Brain Dynamics”. *Journal of Neurotrauma*, Vol. 34, pp. 2154–2166.
- [34] Zhou, Z., Wang, T., Jörgens, D., & Li, X. 2022. “Fiber orientation downsampling compromises the computation of white matter tract-related deformation”. *J. Mech. Behav. Biomed. Mater.*, Vol. 132, pp. 105294.
- [35] Garimella, H.T., Menghani, R.R., Gerber, J.I., Sridhar, S., & Kraft, R.H. 2019. “Embedded Finite Elements for Modeling Axonal Injury”. *Ann. Biomed. Eng.*, Vol. 47, pp. 1889–1907.
- [36] Wu, T., Alshareef, A., Giudice, J.S., & Panzer, M.B. 2019. “Explicit Modeling of White Matter Axonal Fiber Tracts in a Finite Element Brain Model”. *Ann. Biomed. Eng.*, Vol. 47, pp. 1908–1922.

APPENDIX

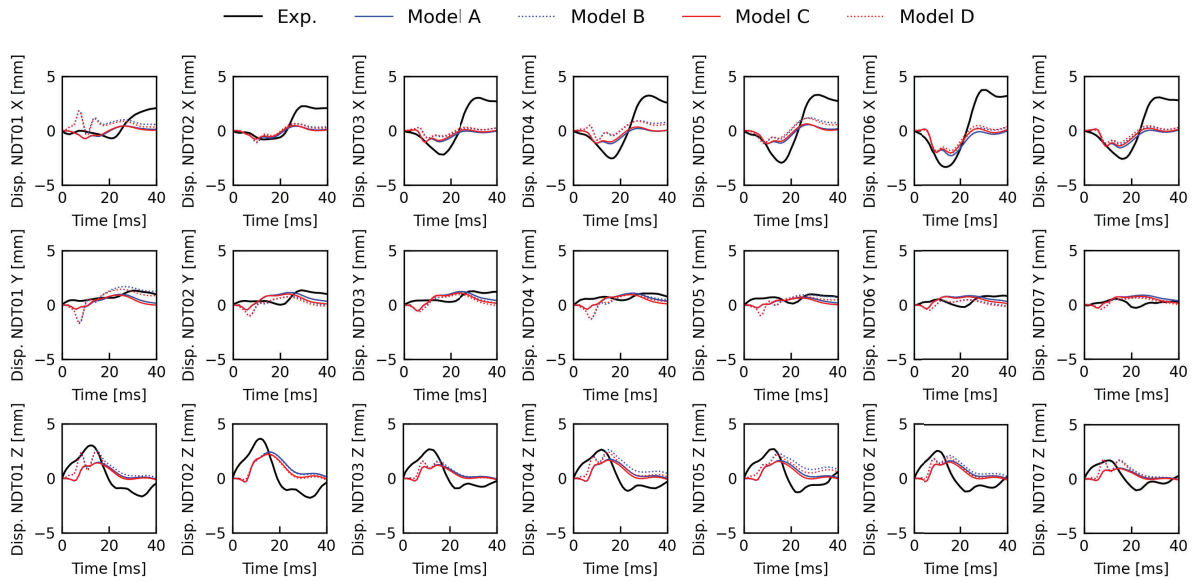


Figure A1. Comparisons of the histories of displacements in NDTs belonging to C1 for C288-T3 between the PMHS test data [24] and the simulation results.

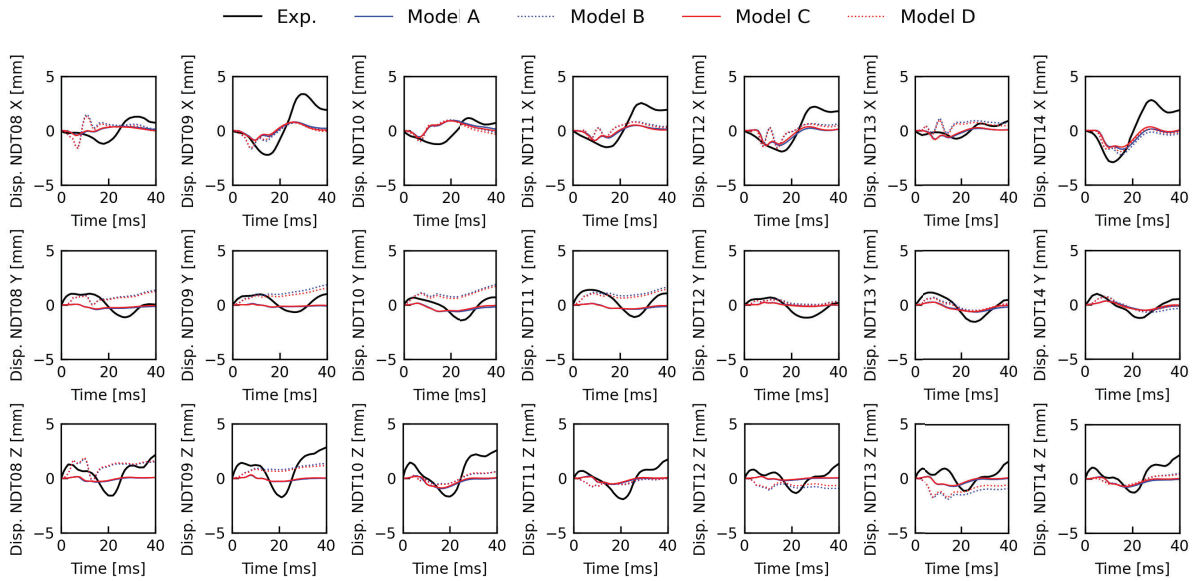


Figure A2. Comparisons of the histories of displacements in NDTs belonging to C2 for C288-T3 between the PMHS test data [24] and the simulation results.

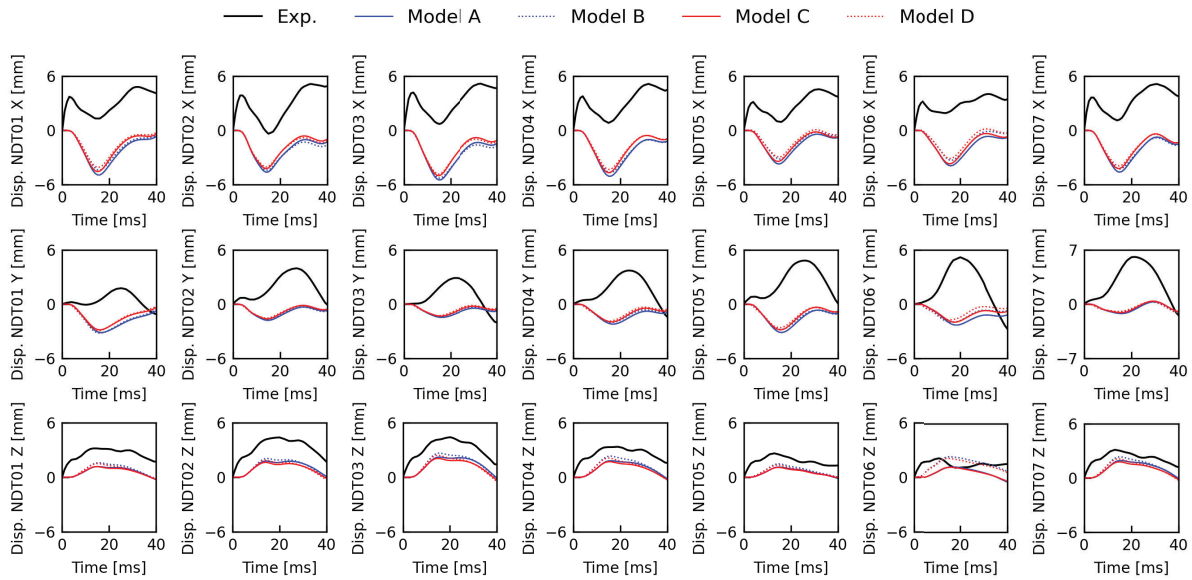


Figure A3. Comparisons of the histories of displacements in NDTs belonging to C1 for C380-T2 between the PMHS test data [24] and the simulation results.

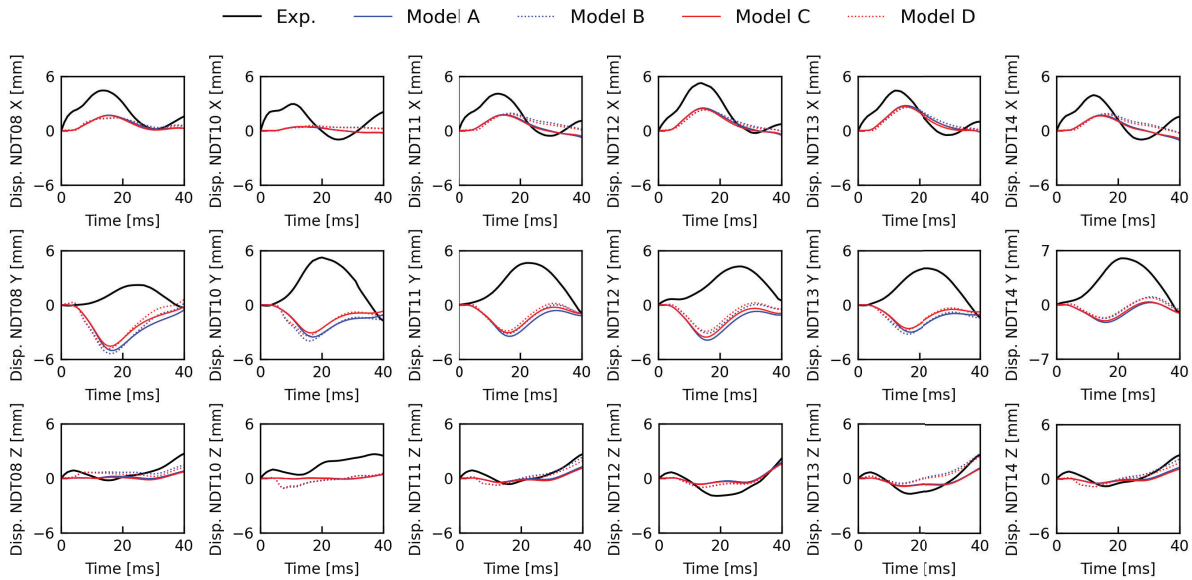


Figure A4. Comparisons of the histories of displacements in NDTs belonging to C2 for C380-T2 between the PMHS test data [24] and the simulation results.

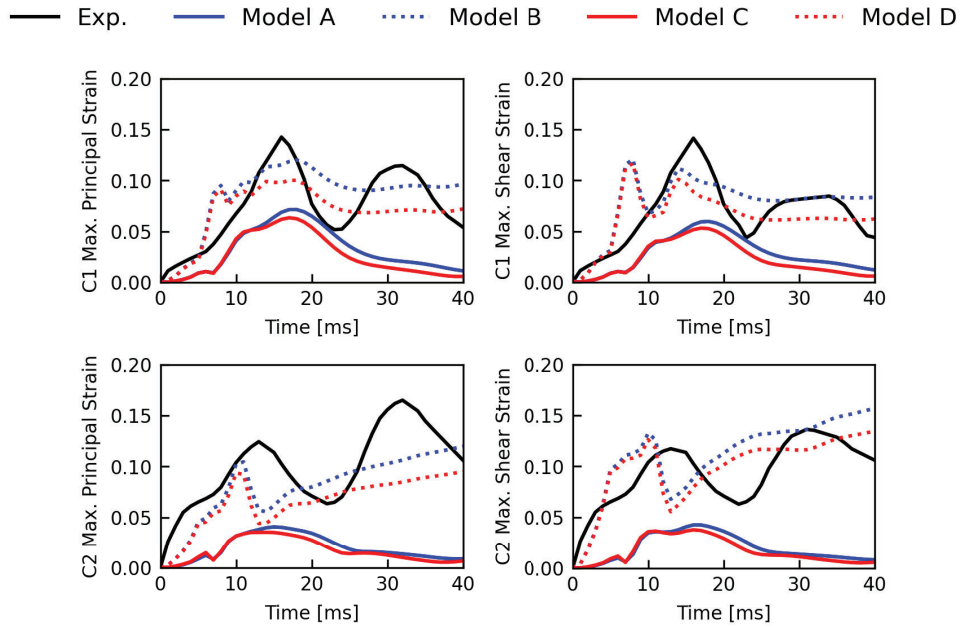


Figure A5. Comparisons of the histories of strain in C1 and C2 for C288-T3 between the PMHS test data [24, 27] and the simulation results.

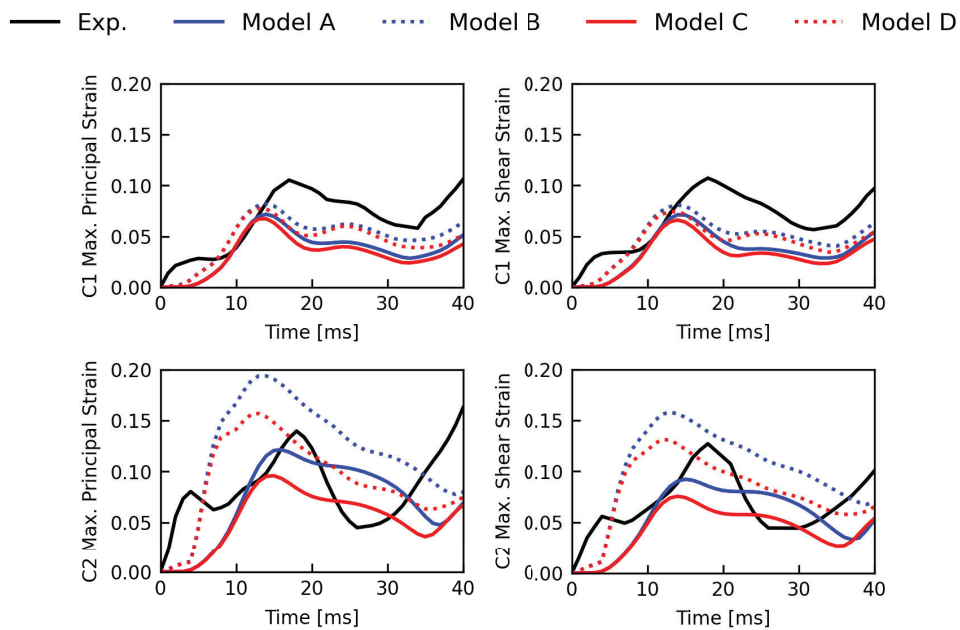


Figure A6. Comparisons of the histories of strain in C1 and C2 for C380-T1 between the PMHS test data [24, 27] and the simulation results.

PEER REVIEW PAPER

This paper has been peer-reviewed and published in a special edition of Traffic Injury Prevention 24(S1), by Taylor & Francis Group. The complete paper will be available on the Traffic Injury Prevention website soon. To access ESV Peer-reviewed papers click the link below
<https://www.tandfonline.com/toc/gcpi20/24/sup1?nav=toCList>

FIELD ASSESSMENT OF GM/ONSTAR OCCUPANT-BASED INJURY SEVERITY PREDICTION

Susan Owen

General Motors
USA

Stewart Wang, Peng Zhang

University of Michigan
USA

Paper Number 23-0123

ABSTRACT

Injury Severity Prediction (ISP) models provide emergency responders with a rapid assessment of potential serious injury for occupants in vehicle accidents around the globe. ISP models predict the need for high level trauma care so that appropriate Emergency Medical Services (EMS) can be dispatched as quickly as possible to improve patient outcomes. In 2020, OnStar implemented its first occupant-based ISP models which predict outcomes for specific seating locations.[1] Models were developed and validated with NHTSA NASS CDS [2] and CISS [3] data. This paper seeks to assess model performance in the field using vehicle-based crash data and real-world occupant outcomes. This study leverages data from a sample of over 1,500 Michigan Advanced Automatic Crash Notification (AACN) events involving over 1,700 front row occupants to assess model performance. Vehicles include model years 2013 to 2020 and span several segments, including passenger cars, SUVs, and light trucks. AACN telemetry data and ISP-predicted outcomes are compared to actual Injury Severity Scores (ISS) for transported occupants. For non-transport cases, police reported injury severities (KABCO scores) are also examined. Measures of sensitivity, specificity, and likelihood ratio are calculated. False negative cases are used to understand model limitations. A range of threshold values used to assess “high” injury risk are also explored to highlight potential tradeoffs. Statistical analyses show that front row occupant models predict ISS 15+ injuries with high levels of accuracy. Metrics compare occupant-based model performance to prior vehicle-based ISP formulations. This study demonstrates that models based on government-sampled data sets are producing reliable results in the field.

INTRODUCTION

For over 20 years, Automatic Crash Notification (ACN) and Advanced Automatic Crash Notification (AACN) have leveraged vehicle telemetry to assist Emergency Medical Services (EMS) in providing rapid response to vehicle accidents. Injury Severity Prediction (ISP) models support this effort by providing a rapid assessment of potential serious occupant injury. Specifically, such models predict the need for high level trauma care so that appropriate resources can be dispatched as quickly as possible to improve patient outcomes.

Recently, the National Expert Panel on Field Triage released an update to the U.S. field triage guidelines.[4] The guidelines are intended to identify research-based criteria for determining when a seriously injured person should be transported to a trauma center, where “serious injury” is aligned with having an Injury Severity Score (ISS) greater than 15. In addition to updating the guideline based on current research findings, the Expert Panel also focused on reducing the rate of under-triage cases (defined as incidents where a seriously injured person is transported to a non-trauma medical center for treatment). The Panel chose a positive likelihood ratio value of 2 as a threshold for identifying research-based factors that merited inclusion in the guidelines. “Vehicle telemetry data consistent with severe injury” [4] was retained as a factor in the updated guidelines, though the authors noted a need for studies focused on evaluating the use of telemetry for field triage.

In 2020, GM/OnStar implemented its first occupant-based ISP models which predict outcomes for specific seating locations.[1] Models were developed and validated with NHTSA NASS CDS [2] and CISS [3] data to predict the occurrence of serious injury outcomes in line with the Field Triage guidelines (i.e., models produce a “High” injury severity prediction if there is a 20% or higher probability of resulting in an ISS of 15+). This paper describes efforts to assess model performance in the field using vehicle-based crash data and real-world occupant outcomes. It also considers potential trade-offs between over- and under-triage based on reducing the threshold for triggering a “High” prediction.

METHODS

U.S. crash investigations documented in CDS and CISS data sets provide detailed information on passenger vehicle collisions, including data on both crash dynamics and occupant outcomes. While these data sets are valuable for building and validating ISP models, it is important to further assess model performance on current field vehicle populations. Such testing ensures performance levels are maintained for actual delta-V inputs (rather than estimated values reported in CDS and CISS) and a broad spectrum of vehicle- and collision types (including late model year vehicles not represented in the latest NHTSA data sets due to lags in data reporting).

To conduct a large-scale field assessment of occupant-based ISP models, a broad set of Michigan AACN cases with calculated ISP scores were matched to available state UD-10 police reports, EMS data, and medical records. Researchers from the University of Michigan Hospital summarized medical outcomes, identifying potential comorbidities and other factors beyond the scope of ISP models. Due to a small number of second-row occupants with severe injury (less than 5 cases), analysis focused on first-row occupants only. When possible, ISP predicted injury severity was compared to actual ISS score to assess model performance using a confusion matrix and associated statistical metrics of sensitivity, specificity, and positive likelihood ratio.

Although crashes must meet a deployment threshold to trigger an AACN event, they represent a range of crash severities. Many cases do not involve EMS transport and not all occupants receive medical treatment. For cases without noted transport, it is impossible to know if occupants elect to seek treatment on their own for sustained injuries, either through a hospital or other medical provider. If hospital records cannot be located, the only available data on potential injury is captured in police-reported KABCO scores. Previous research has shown that KABCO scores can vary dramatically from medically assessed ISS values.[5] For purposes of this study, cases are thus separated into two groups: “matched” cases which include hospital-based occupant ISS scores, and “unmatched” cases which only have KABCO score assessments of occupant injury. For the unmatched set, KABCO scores of “K” and “A” are used to represent cases with severe injury. While it would be cleaner to consider only cases with actual ISS scores, this would bias analysis results by ignoring most cases for which the ISP models are relied upon to accurately identify potential severe injury.

In addition to validating the field performance of occupant-based ISP models, the current study compares their performance to the prior vehicle-based ISP model.[6] In this model, a “High” risk of severe injury is assessed at the vehicle level based on aggregated information about all occupants. In the field, OnStar Emergency Advisors in contact with vehicle occupants determine whether there are any female occupants or any occupants over age 55 and can recalculate ISP findings accordingly. For the current study, age and gender are used to evaluate these parameters when available. The resulting prediction of whether a vehicle is likely to have any occupant with ISS greater than 15 is compared to the maximum first row occupant injury level. Performance metrics for the vehicle-level predictions are compared to those for occupant-based predictions to evaluate any potential loss of predictive power in shifting to more granular models.

Finally, analysis to quantify the tradeoff between over- and under-triage is conducted by lowering the threshold for classifying an occupant as having a “High” probability of severe injury. Shifting from a 20% threshold to a 5% threshold in 5% increments, model sensitivity and specificity are re-evaluated at each level. The resulting plot reveals the increase in over-triaged occupants (who may be sent unnecessarily to a high level trauma center) associated with capturing previously under-triaged occupants.

RESULTS

AACN Cases

The data set for this analysis included a large sample of vehicles that experienced non-rollover AACN events in Michigan between June 2014 and June 2021. 604 vehicles had AACN data matched to police reports, EMS, and hospital records for at least one occupant, while 965 vehicles were in the “unmatched” set that included only AACN and police report data. Vehicles spanned model years 2013 to 2020, with the majority (99%) from 2014 to 2019 and about half from model years 2016 and 2017. Aside from removing predicted rollover cases (for which ISP is not calculated due to the complexity of non-horizontal forces), no filters were applied to AACN cases based on crash

type or severity. A variety of vehicle types and sizes were included in the data set, spanning passenger cars (15%), SUVs (53%), and light trucks (32%).

Model Results

Quantitative summaries Table 1 summarizes model performance for vehicle drivers (left front seat position) in matched cases in a confusion matrix based on predicted outcome and actual ISS values. The sensitivity for these cases is 67%, specificity is 89%, and positive likelihood ratio is 6.

*Table 1.
Confusion matrix for left front occupants in matched cases*

		Predicted 20% probability of ISS 15+		
Actual ISS 15+	Yes	No	Row totals	
Yes	6	3	9	
No	57	477	534	
Column totals	63	480	543	

Table 2 summarizes right front passenger model performance for matched cases in a confusion matrix based on predicted outcome and actual ISS values. The sensitivity for these cases is 50%, specificity is 88%, and positive likelihood ratio is 4.

*Table 2.
Confusion matrix for right front occupants in matched cases*

		Predicted 20% probability of ISS 15+		
Actual ISS 15+	Yes	No	Row totals	
Yes	1	1	2	
No	13	97	110	
Column totals	14	98	112	

Table 3 provides driver model performance for non-matched cases based on police-reported KABCO scores. Assuming that “KA” values align with ISS values of 15+, these cases have a sensitivity of 46%, specificity of 98%, and positive likelihood ratio of 19.

*Table 3.
Confusion matrix for left front occupants in unmatched cases*

		Predicted 20% probability of ISS 15+		
KABCO in “KA”	Yes	No	Row totals	
Yes	5	6	11	
No	23	935	958	
Column totals	28	941	969	

Table 4 provides right front passenger model performance for non-matched cases based on police-reported KABCO scores. These cases have a sensitivity of 100%, specificity of 96%, and positive likelihood ratio of 26.

Table 4.
Confusion matrix for right front occupants in unmatched cases

Predicted 20% probability of ISS 15+			
KABCO in “KA”	Yes	No	Row totals
Yes	2	0	2
No	5	125	130
Column totals	7	125	132

When matched and unmatched cases are taken together, the driver model evaluates to a sensitivity of 55%, specificity of 95%, and a positive likelihood ratio of 10. The right front passenger model evaluates to a sensitivity of 75%, specificity of 93%, and a positive likelihood ratio of 10.

False negative cases Four front passengers in the matched data set were under-triaged, assessed with a “not high” ISP but found to have severe (ISS 15+) injury outcomes. Further examination revealed confounding factors beyond the scope of ISP models in three of the four cases:

1. A 60 year old driver experienced an apparent pre-crash medical event and had confounding co-morbidities that resulted in an ISS of 29 in a crash which evaluated the probability of high injury severity to be only 0.4%.
2. A 42 year old belted driver was struck by a falling object that came through the windshield, resulting in an ISS of 19. The associated crash was assessed to have probability of high injury severity of 0.5%.
3. A fatal 86 year old belted driver experienced an apparent pre-crash medical event and had confounding co-morbidities that resulted in an ISS of 17. The associated crash was assessed to have an ISP of 19.4%, just below the ISP “High” threshold.

In the unmatched data there appear to be 6 under-triaged drivers based on police-reported “KA” injury scores, four of which were listed as not being transported by EMS. Without further information, it is impossible to know if the assigned KABCO scores accurately reflected occupant injuries.

Comparison to vehicle-based ISP Table 5 provides a confusion matrix for the 1553 vehicle-based ISP assessments. Using this method, the sensitivity for these cases is 48%, specificity is 97%, and positive likelihood ratio is 15.

Table 5.
Confusion matrix for vehicle-based ISP applied to combined matched/unmatched cases

Predicted 20% probability of ISS 15+			
Any occupant ISS 15+ or “KA”	Yes	No	Row totals
Yes	12	13	25
No	50	1478	1528
Column totals	62	1491	1553

Over- Vs. Under-Triage Tradeoff

As described above, analysis was conducted to explore over- vs. under-triage tradeoffs by setting the threshold for “High” ISP evaluation below the current 20% level. Figure 1 shows the impact of dropping the threshold from 20% to 5% in 5-point increments. As expected, reducing the threshold probability causes more occupants to be classified as “High” risk, and thus reduces the amount of under-triage while also increasing the amount of over-triage. The

positive likelihood ratio falls from 10 at the 20% threshold to just under 4 at the 5% threshold. While moving the threshold from 20% to 5% allowed the algorithm to drop the under-triage (false negative) group from 10 occupants to 5, it did so at substantial cost – more than tripling the over-triage (false positive) group from 100 occupants to 379.

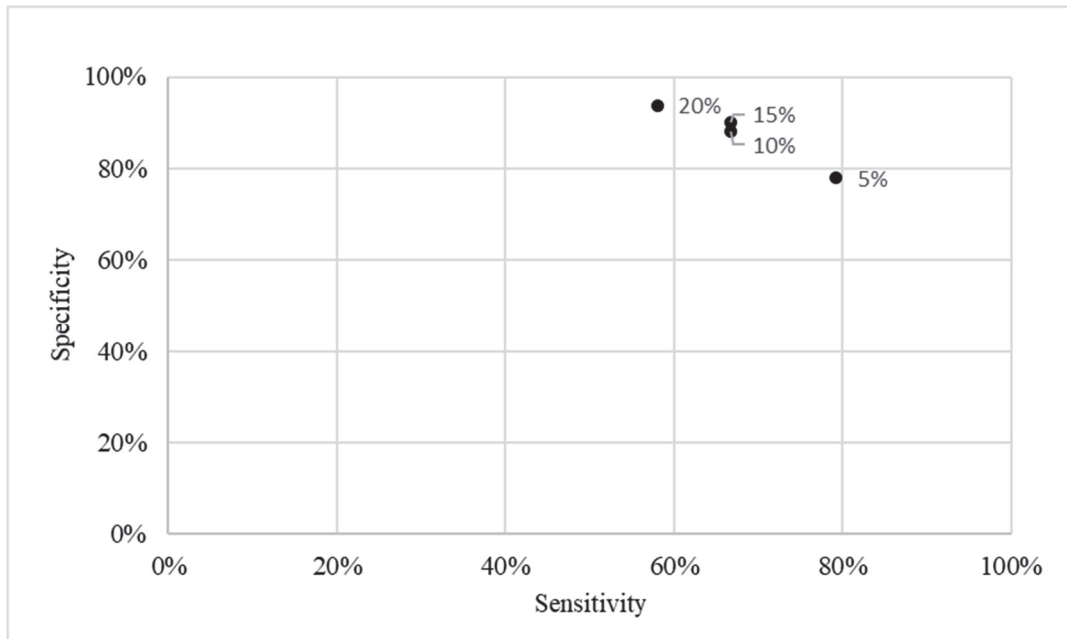


Figure 1. Performance tradeoff associated with lowering the threshold for front row HIGH ISP from 20% to 5%.

DISCUSSION AND LIMITATIONS

The analysis of cases in this study provides a field-based assessment of occupant-based ISP models for front row outboard occupants. Additional models for second row occupants have been fit, validated, and implemented, but limited populations of seriously injured second row occupants make it difficult to capture meaningful statistics on model performance. The cases were pulled from a broad sample of Michigan AACN crashes due to accessibility of police report, EMS, and medical outcome data. While the cases span several model years, vehicle platforms, and crash severities, they may not be representative of the overall US AACN crash population.

Based on this study, results demonstrate that occupant-based ISP model performance for front row passengers is strong. At the current 20% threshold, the positive likelihood ratio of 10 far exceeds the level specified in updated Field Triage Guidelines. Compared to the vehicle-based model, the front row occupant-based ISP models improve sensitivity (from 48% to 58%) with a slight degradation in specificity (from 97% to 94%). This performance is promising, given the potential value that occupant-based models provide – enabling OnStar to identify for EMS the number and location of severely injured occupants.

Work to monitor model performance in the U.S. is ongoing. Efforts to quantify 2nd row model performance continue as additional cases are collected and analyzed. Additional exploration of lowering the threshold for “High” probability of severe injury also continues. Tradeoffs need to consider the systemic costs of over- and under-triage. While the Expert Panel focused on potential improvements in occupant outcomes associated with reducing under-triage, recent NHTSA publications (e.g., [7]) highlight constraints in EMS resources that could be exacerbated by increasing levels of over-triage. Finally, research to quantify the effect of AACN/ISP on EMS response times and occupant outcomes is needed, but requires access to significant volumes of crash, EMS, and injury data not currently available in the US.

ACKNOWLEDGEMENTS

The authors acknowledge John Capp, Director of Vehicle Safety Technology, Strategy, & Regulations at GM, and Cathy Bishop, Senior Manager of Emergency Services at OnStar in their continued support for improved system safety, including post-crash emergency response.

REFERENCES

- [1] Owen SH, Joyner JW, Zhang P, Wang SC. Occupant-based Injury Severity Prediction. *Stapp Car Crash J.* 2021 Nov; 65:17-28.
- [2] Radja GA. National Automotive Sampling System – Crashworthiness Data System, 2015 Analytical User’s Manual. Report No. DOT HS 812 321. 2016 Sept. Washington, DC: National Highway Traffic Safety Administration.
- [3] National Center for Statistics and Analysis. Overview of the 2017 Crash Investigation Sampling System. *Traffic Safety Facts Research Note.* Report No. DOT HS 812 787. 2019, Sept. National Highway Traffic Safety Administration.
- [4] Newgard CD, Fischer PE, Gestring M, Michaels HN, Jurkovich GJ, Lerner EB, Fallat ME, Delbridge TR, Brown JB, Bulger EM. National Guideline for the Field Triage of Injured Patients: Recommendations of the National Expert Panel on Field Triage, 2021. *J Trauma Acute Care Surg.* 2022 Aug; 93(2):e49-e60.
- [5] Burdett B, Li Z, Bill AR, Noyce DA. Accuracy of Injury Severity Ratings on Police Crash Reports. *Trans. Res. Rec.* 2015 Jan; 2516(1):58-67.
- [6] Wang S, Kohoyda-Inglis C, Ejima S, MacWilliams J, Zhang P, Stacey L, Melocchi A, Gorman D, Kral J, Joyner J. Second Generation AACN Injury Prediction Algorithm: Development and Real-World Validation. 25th International Conference on Enhanced Safety of Vehicles. 2017; 17-0133.
- [7] Office of Behavioral Safety Research. Continuation of research on traffic safety during the COVID19 public health emergency: January – June 2021. Report No. DOT HS 813 210. 2021 Oct. National Highway Traffic Safety Administration.

PEER REVIEW PAPER

This paper has been peer-reviewed and published in a special edition of Traffic Injury Prevention 24(S1), by Taylor & Francis Group. The complete paper will be available on the Traffic Injury Prevention website soon. To access ESV Peer-reviewed papers click the link below
<https://www.tandfonline.com/toc/gcpi20/24/sup1?nav=toCList>

PEER REVIEW PAPER

This paper has been peer-reviewed and published in a special edition of Traffic Injury Prevention 24(S1), by Taylor & Francis Group. The complete paper will be available on the Traffic Injury Prevention website soon. To access ESV Peer-reviewed papers click the link below
<https://www.tandfonline.com/toc/gcpi20/24/sup1?nav=toCList>

PEER REVIEW PAPER

This paper has been peer-reviewed and published in a special edition of Traffic Injury Prevention 24(S1), by Taylor & Francis Group. The complete paper will be available on the Traffic Injury Prevention website soon. To access ESV Peer-reviewed papers click the link below
<https://www.tandfonline.com/toc/gcpi20/24/sup1?nav=toCList>

INJURY RISK ESTIMATION IN FAR-SIDE IMPACTS USING SMALL FEMALE AND AVERAGE MALE FINITE ELEMENT HUMAN BODY MODELS

Karan Devane

Bharath Koya

Ashley A. Weaver

F. Scott Gayzik

Biomedical Engineering,

Wake Forest University School of Medicine

USA

Fang-Chi Hsu

Department of Biostatistics and Data Science, Division of Public Health Sciences,

Wake Forest University School of Medicine

USA

Matthew Davis

Berkan Guleyupoglu

Elemance, LLC

USA

Paper Number 23-0149

ABSTRACT

Far-side crashes are the second-highest, after near-side impact crashes, cause of MAIS 3+ injuries to occupants for ΔV above 48 kph. The objective of this study was to estimate and compare injury risks between a small female and an average male occupant in far-side crashes using finite element human body models (HBM) in a simplified vehicle environment. To study far-side crashes, 126 simulations were conducted as a design of experiments (DOE) by varying lateral ΔV (10-50kph; 5kph increments), the principal direction of force (PDOF 50°, 60°, 65°, 70°, 75°, 80°, 90°), and occupant model. Occupant models used were the Global Human Body Models Consortium (GHBMC) 5th-percentile female (F05) and 50th-percentile male (M50) simplified models (-OS) with a modular detailed brain (+B). Overall skeletal structures are shared between the detailed and simplified models which allows the modular use of detailed parts in simplified models. Models were gravity settled and belted into a simplified vehicle model (SVM) modified for far-side impact simulations. The far-side SVM (FSVM) has both driver and passenger seats and door intrusion on the far side implemented. Acceleration pulses and vehicle intrusion profiles used for the DOE were generated by impacting a 2011 Camry vehicle model with a mobile deformable barrier model across the 7 PDOFs and 9 lateral ΔV 's in the DOE for a total of 63 additional simulations. The impacted surface of the Camry was instrumented to measure relative displacement into the vehicle to generate an intrusion profile. Injury risks were estimated for the head and chest (AIS2+; AIS3+) and abdomen and pelvis (AIS3+). Overall AIS3+ injury risk for each occupant was calculated using AIS3+ injury risk estimations for the head, chest, abdomen, and pelvis. A Wilcoxon signed-rank test was used to test for significant differences between estimated risks for F05-OS+B vs. M50-OS+B. Statistically significant differences between F05-OS+B and M50-OS+B were found for AIS2+ risk of head injury and AIS3+ risk of head, chest, and pelvis injury. No significant differences were found for AIS3+ risk of an abdominal injury and AIS2+ risk of chest injury. The overall risk of AIS3+ injury was higher for the M50-OS+B than the F05-OS+B in 84% of cases. Injury risk increased with an increase in lateral ΔV which was in agreement with studies found in the literature. An investigation of injury risks associated with far-side crashes was undertaken for both an average male and small female HBM. Differences observed in the estimated injury risks suggest that occupant size should be taken into consideration in safety system design. While this study used an FSVM with a rigid center console and dashboard, the relative differences between models were investigated. The effect of occupant size/sex on injury risk was highlighted by differences in overall injury risk for small female vs. average male HBMs. The study describes a method for simulating far-side crashes with an SVM that can include an estimation of intrusion.

INTRODUCTION

Even though 35% of side impact-related occupant injuries are due to far-side collisions [1] there are currently no regulatory tests for far-side scenarios in US-NCAP and the introduction of a far-side protocol in Euro-NCAP was in 2020 [2]. Analysis of real-world far-side crashes showed that the head and thorax are the two most frequently injured body regions followed by the abdomen [3]. The struck-side interior and the seatbelt are the first two contacting surfaces that cause injuries in far-side crashes [3, 4]. Currently, some vehicles may deploy all the side airbags so that a driver in a far-side crash could benefit from it but there are no countermeasures specifically designed to reduce injuries to far-side occupants. With the advancement in automotive technology, the far-side crash mode will become more relevant with highly automated vehicles (HAVs) with their non-standard seating configurations [5]. It is therefore necessary to develop different strategies to safeguard occupants in far-side crashes. Multiple studies have experimented with far-side events [6, 7], but their use for designing countermeasures is limited due to reduced boundary conditions. These studies did not take into account the effect of intrusion and/or deformable vehicle interiors. Experimental studies are expensive for performing parametric studies and it is not feasible to capture all the aspects of a real-world crash in laboratory tests.

On the other hand, computer simulations with finite element human body models (FEHBM) are one of the versatile tools for estimating injury risk in various scenarios as well as countermeasure development. Previous studies have demonstrated the use of FEHBMs for estimating injury risk in frontal, near-side, far-side, and rear impact events [2, 3, 5, 8-11]. Arun et al. studied occupant injuries and kinematics in far-side crashes using an occupant model in a full-scale vehicle model in 12 different scenarios [3], while Pipkorn et al. evaluated far-side airbags for reducing occupant injuries [2] by varying principal directions of force (PDOF). None of the studies so far has studied far-side crashes extensively using occupant models of different sizes and sexes, different PDOFs, and different impact velocities. All these variables affect injury risk to the occupant.

The objectives of this study were to estimate the injury risk in far-side impacts for small females and average males using FEHBMs, and then compare the results of the two models to check for differences in injury risk. The study used two FEHBMs representing small female and average male occupant models in a far-side simplified vehicle model (FSVM) in a parametric study by varying PDOF and lateral delta-V (ΔV).

METHODS

The Global Human Body Models Consortium small female (F05-OS+B v2.3) and average male (M50-OS+B v2.3) model with the detailed modular brain (from v6.0 detailed occupant models) were used in this study to simulate far-side crashes in an FSVM (Figure 1). A full-factorial design of experiment (DOE) was carried out using these two HBMs and varying lateral ΔV and PDOF. The lateral ΔV was varied in increments of 5 kph from 10 to 50 kph and seven different PDOFs (50°, 60°, 65°, 70°, 75°, 80°, and 90°) were used in the DOE. A total of 126 simulations were run as a part of the DOE. The acceleration pulses (longitudinal and lateral) and vehicle intrusion profiles for the DOE were generated by impacting a 2012 Toyota Camry model with a mobile deformable barrier (MDB) model at the 9 lateral ΔV and 7 PDOFs mentioned above to simulate a total of 63 far-side impact scenarios (Figure 2). The impacted surface of the Camry was instrumented to measure relative displacement into the vehicle to generate an intrusion profile, whereas vehicle acceleration pulses were measured using a seatbelt accelerometer attached to the floor at the bottom of the driver seat.



Figure 1. Far-side impact simulation setup with F05-OS+B model settled in a far-side simplified vehicle model

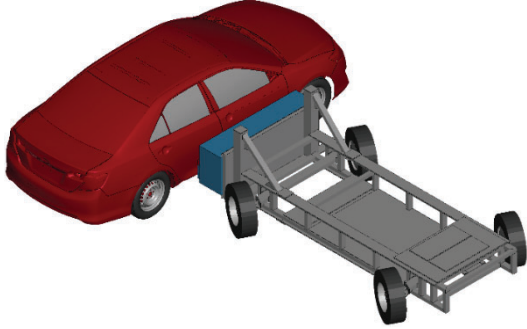


Figure 2. Toyota Camry-MDB far-side impact simulation setup

Each simulation with occupant models was run for 150 ms using LS-DYNA R10.2 (Ansys LSTC, Livermore, CA, USA). Both HBMs are instrumented to measure Head Injury Criterion (HIC), Brain Injury Criterion (BrIC), rib deflection, Combined Thoracic Index (CTI), abdominal force, and pubis force. All these injury metrics were used to estimate Abbreviated Injury Scale (AIS) 2+ and AIS3+ injury risk for the head and chest and AIS3+ injury risk for the abdomen and pelvis. The equations used for estimating all these injury risks were taken from previous studies (Table 1). Overall AIS3+ injury risk was calculated for each simulation using AIS3+ injury risk estimations for the head, chest, abdomen, and pelvis using the equation mentioned in Table 1. All the estimated injury risks for the M50-OS+B were compared to the F05-OS+B model injury risks. The matched-pair differences between the two models were checked for statistical significance using a Wilcoxon signed-rank test. R^2 was calculated to determine the proportion of variance of the estimate from one model that could be explained by the estimate from the other model using a linear regression model.

Table 1. Biomechanical risk curves used to determine model-based risk separated by body region, injury metric, and citation

Region	Metric	Equation	Citation
Head	HIC	$p(fracture) = \phi\left(\frac{\ln(HIC36) - \mu}{\sigma}\right)$ $AIS2+: \mu = 6.96352; \sigma = 0.84664$ $AIS3+: \mu = 7.45231; \sigma = 0.73998$	[12]
		$p(AIS2+) = \frac{1}{1 + e^{[(2.49 + \frac{200}{HIC}) - 0.00483 * HIC]}}$ $p(AIS3+) = \frac{1}{1 + e^{[(3.39 + \frac{200}{HIC}) - 0.00372 * HIC]}}$	[13, 14]
	BrIC	$p(AIS2+) = 1 - e^{-\left(\frac{BrIC}{0.602}\right)^{2.84}}$ $p(AIS3+) = 1 - e^{-\left(\frac{BrIC}{0.987}\right)^{2.84}}$	[15]
		$p(AIS2+) = 1 - \frac{1}{1 + e^{-(7.022 - (4.251 * BrIC))}}$ $p(AIS3+) = 1 - \frac{1}{1 + e^{-(8.549 - (4.251 * BrIC))}}$	[16]
Thorax	Rib Deflection	$p(AIS3+) = \frac{1}{1 + e^{(9.02937 - (0.03705 * (Age - 36.8232)) * Defl)}}$	[12]
	CTI	$p(AIS2+) = \frac{1}{1 + e^{(4.847 - (6036 * CTI))}}$	[17]
Abdomen	Abdominal Force	$p(AIS3+) = \frac{1}{1 + e^{6.04044 - (0.002133 * AbdForce)}}$	[12]
Pelvis	Pubis Force	$p(AIS3+) = \frac{1}{1 + e^{(9.7023 - (0.04678 * Age) - 0.0011 * Force)}}$	[12]
Overall	$P_{overall} = 1 - (1 - P_{head})(1 - P_{chest})(1 - P_{abdomen})(1 - P_{pelvis})$		

RESULTS

All 63 Camry-MDB and 126 simulations with two HBMs ran for 150 ms without any errors. The average solution times were 4 min/ms and 4.1 min/ms for M50-OS+B and F05-OS+B respectively. The results of the Wilcoxon signed-rank test and R^2 values of each injury risk comparison between the two models are reported in Table A1 in the appendix. The differences between the M50-OS+B vs. F05-OS+B model estimated injury risks were statistically significant ($p < 0.05$) except for the chest AIS2+ and abdomen AIS3+ injury risks. All the injury risks for the two models are cross-plotted in Figure 3 - Figure 8. All these figures include blue dots representing M50-OS+B injury risk on the x-axis and F05-OS+B model risk on the y-axis, a linear fit regression blue line for model risk points, and a black line of equivalence for reference. The closer all the dots are to the line of equivalence, the more similar the injury risk predicted by the two models. Also more points on the right of the line of equivalence the higher the M50-OS+B model estimated risk of injury and vice-versa. The M50-OS+B model estimated risks for all the body regions except the abdomen were higher than F05-OS+B. The overall injury risk was higher in 84% of cases for the M50-OS+B model. The BrIC-based head AIS2+ using Takhount et al. 2013 (Figure 5 left $R^2 = 0.95$) and chest AIS2+ (Figure 7 left $R^2 = 0.88$) injury risk were similar between the two models.

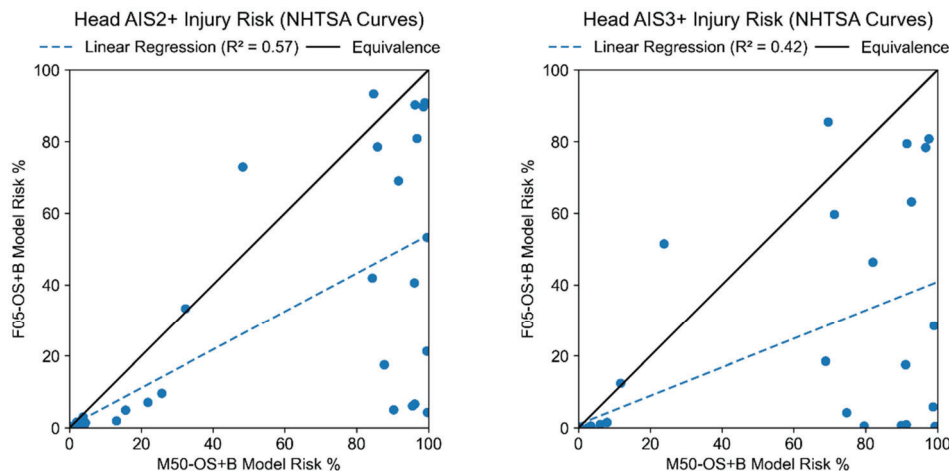


Figure 3. Cross-plot of the head injury risk (AIS2+: left, AIS3+: right) based on HIC using NHTSA curves [12]. M50-OS+B is on the x-axis and F05-OS+B is on the y-axis.

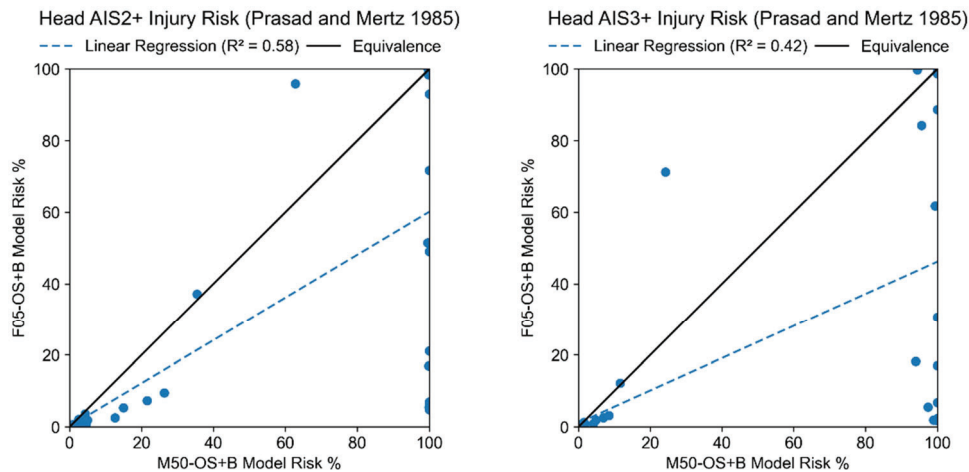


Figure 4. Cross-plot of the head injury risk (AIS2+: left, AIS3+: right) based on HIC using equations from Prasad and Mertz, 1985 [14]. M50-OS+B is on the x-axis and F05-OS+B is on the y-axis.

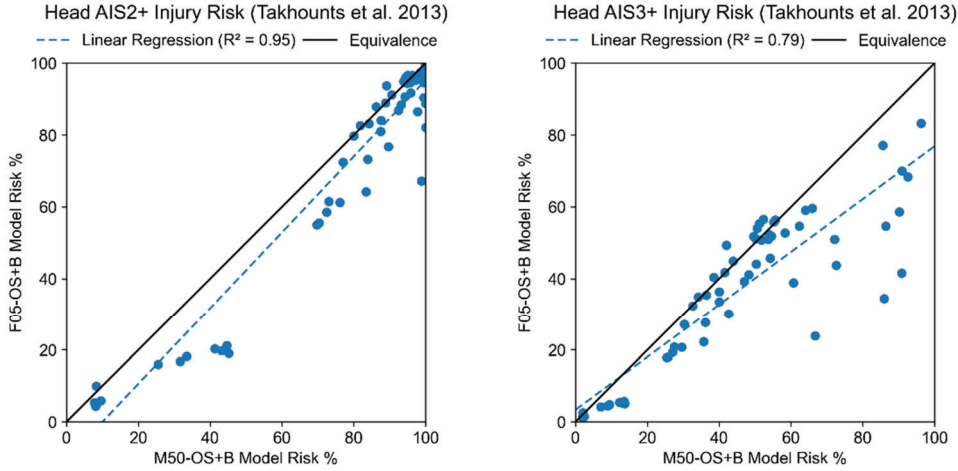


Figure 5. Cross-plot of the head injury risk (AIS2+: left, AIS3+: right) based on BrIC using equations from Takhounts et al. 2013 [15]. M50-OS+B is on the x-axis and F05-OS+B is on the y-axis.

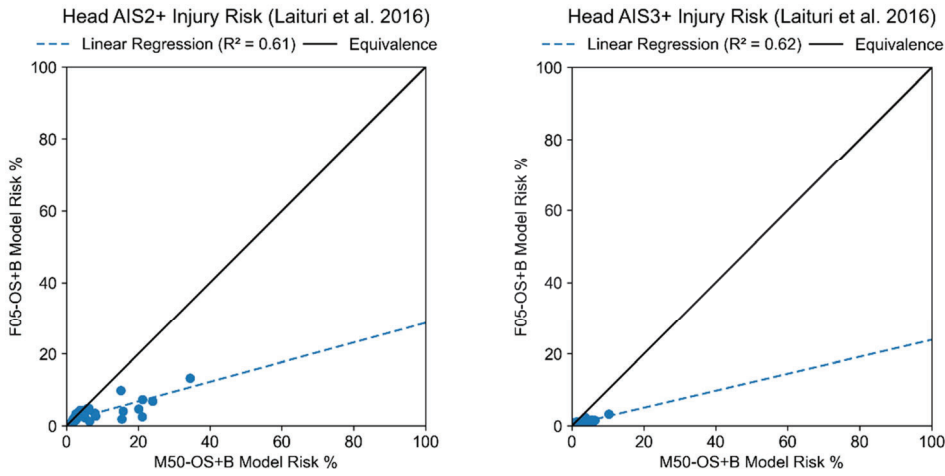


Figure 6. Cross-plot of the head injury risk (AIS2+: left, AIS3+: right) based on BrIC using equations from Laituri et al. 2016 [16]. M50-OS+B is on the x-axis and F05-OS+B is on the y-axis.

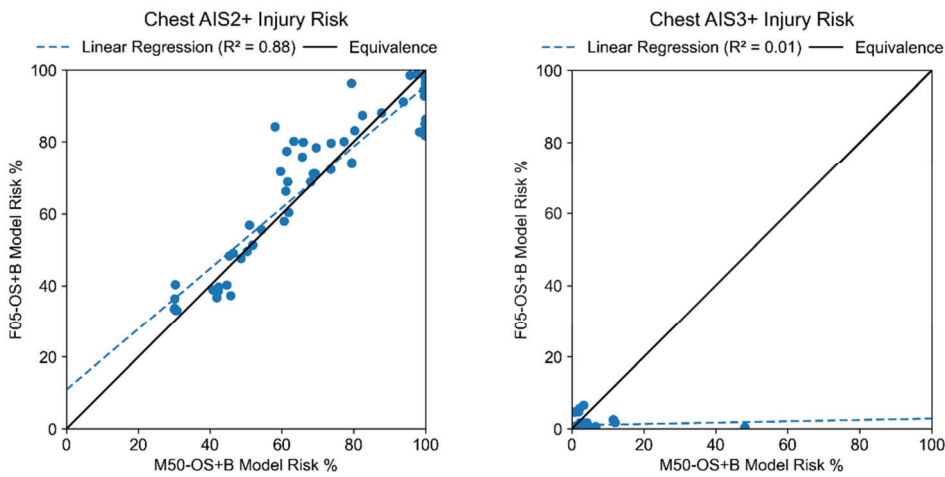


Figure 7. Cross-plot of the chest injury risk based on CTI (AIS2+: left) [17] and chest deflection (AIS3+: right) [12]. M50-OS+B is on the x-axis and F05-OS+B is on the y-axis.

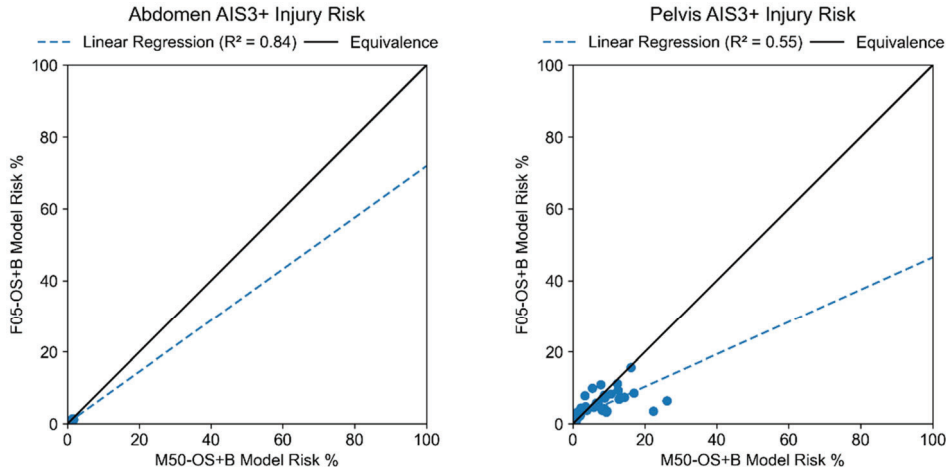


Figure 8. Cross-plot of the abdomen (left) and pelvis (right) AIS3+ injury risk based on abdomen and pubis force using equations from Kupp, 2004 [12]. M50-OS+B is on the x-axis and F05-OS+B is on the y-axis.

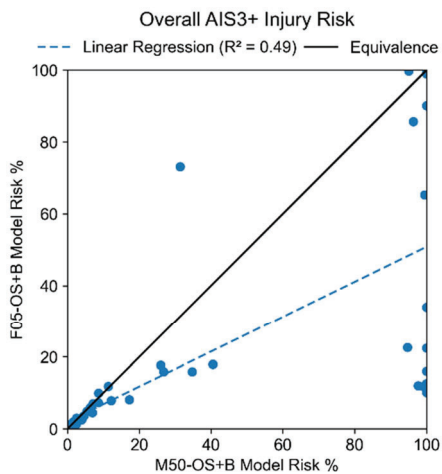


Figure 9. Cross-plot of the overall AIS3+ injury risk. M50-OS+B is on the x-axis and F05-OS+B is on the y-axis.

DISCUSSION

The objective of the current study was to simulate a variety of far-side impact scenarios using small female and average male occupant models and compare estimated injury risks. A total of 126 far-side crash simulations were simulated using two FEHBMs, 7 PDOFs, and 9 lateral ΔV s in an FSVM that included vehicle intrusion. Except for abdomen AIS3+ and chest AIS2+, the differences between all other injury risks were statistically significant ($p < 0.05$). The overall injury risk was higher in 84% of the cases for M50-OS+B than F05-OS+B suggesting the need for different countermeasures for different occupant sizes. A recent study by Klug et al. 2022 suggested that for robust assessment of vehicles in the virtual environment, a wide range of anthropometries should be considered. This study analyzed far-side crashes from multiple real-world crash databases from the US and Europe.

Due to the size differences between the two models the lateral motion was different. The male model had a higher lateral excursion in all the cases than the female model. Exemplar results of a far-side impact for ΔV of 50 kph at 90° PDOF at 5 different time points are depicted in Table A2 that shows higher lateral displacement for the male model. Both models contacted the far-side interior parts of the vehicle but the male model contacted more often than the female model. Shoulder seatbelt slippage may be one of the reasons for more lateral motion. With improved belt retention risk of injury will be lowered and this is one of the areas that need further investigation. The overall injury risk was increased with an increase in lateral ΔV but no trend was observed with a change in PDOF.

The study estimated AIS2+ and AIS3+ head injury risks using HIC and BrIC. In a previous study, AIS2+ head injury risk was estimated using the HIC-based Prasad and Mertz, 1985 [14] and BrIC-based Laituri et al. 2016 [16] equations which were better correlated with field-based injury risk data [18]. A similar study could be carried out in the future to compare all body region injury risks to real-world data using logistic regression equations from a literature study [19]. For both the models, head and chest injury risk were higher than injury risk for other body regions which was in line with what was reported by Digges and Dalmotas by analyzing real-world far-side crashes [4]. Although head and chest injury risks were in agreement with real-world injury incidence, the estimated abdominal injury risks were too low and needs further investigation. One of the reasons could be the use of a simplified vehicle model with a rigid center console and dashboard which may have affected occupant kinematics. Another limitation of the study was that the Camry-MDB impact for various PDOF was carried out by changing x- and y- velocities and keeping MDB's initial position the same for all the simulations rather than rotating it. This would have affected the intrusion profiles used in the study but the initial position was kept constant to reduce the number of variables between each simulation to improve comparisons between simulations. The intrusion profile was same for both the models in each case which allowed for relative differences to be studied within cases simulated.

CONCLUSIONS

This study employed a DOE approach with an FSVM incorporating intrusion to simulate and estimate injury risk for small females and average males in multiple far-side crash events. The injury risks increased with an increase in lateral ΔV . The average male had a higher risk of injury than a small female in all the body regions except the abdomen. The differences in injury risks between the male and female models were statistically significant. The effect of occupant size/sex on injury risk was highlighted by significant differences in overall injury risk for the small female vs. average male HBMs. Differences observed in the estimated injury risks suggest that occupant size/sex should be taken into consideration in safety system design.

ACKNOWLEDGEMENTS

This work was funded by the United States Council for Automotive Research (USCAR) under grant ID: 21-2262-USC. All simulations were run on the DEAC cluster at Wake Forest University with support from Stevens Cody and Adam Carlson.

DISCLOSURE STATEMENT

F. Scott Gayzik and Matthew Davis are members and Ashley A. Weaver is a consultant of Elemance, LLC., which distributes academic and commercial licenses for the use of GHBMCM-owned computational human body models.

REFERENCES

- [1] H. C. Gabler, K. Digges, B. N. Fildes, and L. Sparke, "Side impact injury risk for belted far side passenger vehicle occupants," *SAE transactions*, pp. 34-42, 2005.
- [2] B. Pipkorn *et al.*, "Occupant protection in far-side impacts," in *Proceedings of IRCOBI conference*, 2018, vol. 46, pp. 125-127.
- [3] M. W. J. Arun, S. Umale, J. R. Humm, N. Yoganandan, P. Hadagali, and F. A. Pintar, "Evaluation of kinematics and injuries to restrained occupants in far-side crashes using full-scale vehicle and human body models," *Traffic Injury Prevention*, vol. 17, no. sup1, pp. 116-123, 2016/09/12 2016, doi: 10.1080/15389588.2016.1197394.
- [4] K. Digges and D. Dalmotas, "Injuries to restrained occupants in far-side crashes," SAE Technical Paper, 2001.
- [5] Y. Kitagawa, S. Hayashi, K. Yamada, and M. Gotoh, "Occupant kinematics in simulated autonomous driving vehicle collisions: influence of seating position, direction and angle," SAE Technical Paper, 2017.
- [6] F. A. Pintar *et al.*, "Comparison of PMHS, WorldSID, and THOR-NT responses in simulated far side impact," *Stapp car crash journal*, vol. 51, p. 313, 2007.
- [7] R. Kent, J. Forman, D. Lessley, K. Arbogast, and K. Higuchi, "A parametric study of far-side restraint mechanics," in *Proc. Conference on the Enhanced Safety of Vehicles Paper*, 2013, no. 13-0381.
- [8] J. Broos and R. Meijer, "Simulation Method for Whiplash Injury Prediction Using an Active Human Model," in *Proceedings of the IRCOBI Conference*, 2016.

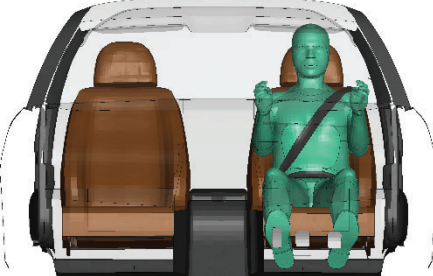
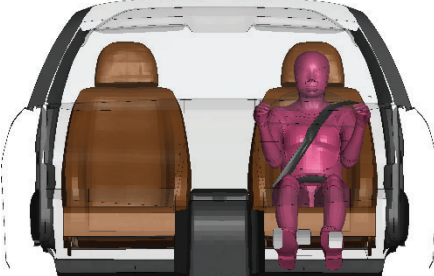


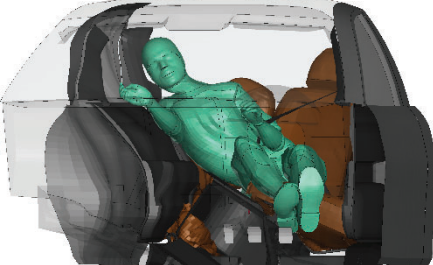
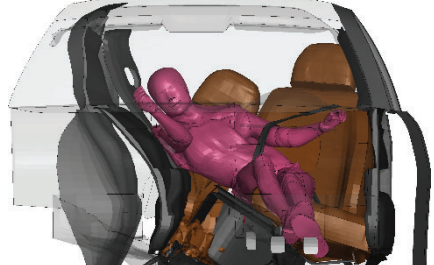
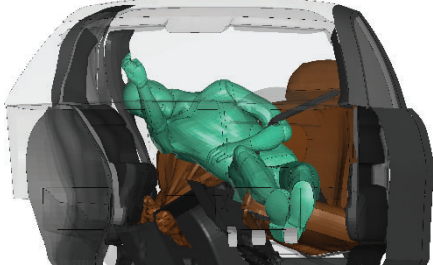



- [9] T. Ando, Y. Kitagawa, and A. Eggers, "Influence of Posture Adjustment Methods for Human Body Models on Injury Prediction," *Accident Reconstruction Journal*, vol. 30, no. 2, 2020.
- [10] W. B. Decker, D. A. Jones, K. Devane, M. L. Davis, J. P. Patalak, and F. S. Gayzik, "Simulation-based assessment of injury risk for an average male motorsport driver," *Traffic Inj Prev*, vol. 21, no. sup1, pp. S72-S77, Oct 12 2020, doi: 10.1080/15389588.2020.1802021.
- [11] W. B. Decker *et al.*, "Effect of body size and enhanced helmet systems on risk for motorsport drivers," *Traffic Injury Prevention*, vol. 22, no. sup1, pp. S49-S55, 2021/10/19 2021, doi: 10.1080/15389588.2021.1977802.
- [12] S. Kuppa, "Injury criteria for side impact dummies," *Washington, DC: National Transportation Biomechanics Research Center, National Highway Safety Administration, US DOT*, vol. 67, 2004.
- [13] H. J. Mertz, P. Prasad, and G. Nusholtz, "Head injury risk assessment for forehead impacts," *SAE transactions*, pp. 26-46, 1996.
- [14] P. Prasad and H. J. Mertz, "The position of the United States delegation to the ISO Working Group 6 on the use of HIC in the automotive environment," *SAE transactions*, pp. 106-116, 1985.
- [15] E. G. Takhounts, M. J. Craig, K. Moorhouse, J. McFadden, and V. Hasija, "Development of brain injury criteria (BrIC)," *Stapp car crash journal*, vol. 57, p. 243, 2013.
- [16] T. R. Laituri, S. Henry, K. Pline, G. Li, M. Frankstein, and P. Weerappuli, "New risk curves for NHTSA's brain injury criterion (BrIC): derivations and assessments," *SAE Technical Paper*, 2016.
- [17] F. Bandak *et al.*, "Development of improved injury criteria for the assessment of advanced automotive restraint systems: II," 1999.
- [18] K. Devane *et al.*, "Comparisons of head injury risk prediction methods to field data in far-side impacts," *Traffic Injury Prevention*, pp. 1-3, 2022, doi: 10.1080/15389588.2022.2124809.
- [19] Z. S. Hostetler *et al.*, "Injury risk curves in far-side lateral motor vehicle crashes by AIS level, body region and injury code," *Traffic Injury Prevention*, vol. 21, no. sup1, pp. S112-S117, 2020/10/12 2020, doi: 10.1080/15389588.2021.1880006.

APPENDIX A

Table A1. Results of statistical tests used for comparing model estimated injury risks

Injury Risk	Metrics Used	Linear Regression Parameters			Wilcoxon signed-rank p-value
		R ²	slope	intercept	
Head AIS2+ Injury Risk (NHTSA Curves)	HIC	0.57	0.54	0.42	0.000
Head AIS3+ Injury Risk (NHTSA Curves)	HIC	0.42	0.40	0.95	0.000
Head AIS2+ Injury Risk (Prasad and Mertz 1985)	HIC	0.58	0.60	0.14	0.000
Head AIS3+ Injury Risk (Prasad and Mertz 1985)	HIC	0.42	0.45	1.09	0.000
Head AIS2+ Injury Risk (Takhounts et al. 2013)	BrIC	0.95	1.06	-10.61	0.000
Head AIS3+ Injury Risk (Takhounts et al. 2013)	BrIC	0.79	0.74	3.34	0.000
Head AIS2+ Injury Risk (Laituri et al. 2016)	BrIC	0.61	0.27	1.29	0.000
Head AIS3+ Injury Risk (Laituri et al. 2016)	BrIC	0.62	0.24	0.31	0.000
Chest AIS2+ Injury Risk	CTI	0.88	0.85	10.89	0.774
Chest AIS3+ Injury Risk	Chest Deflection	0.01	0.02	0.95	0.000
Abdomen AIS3+ Injury Risk	Abdominal Force	0.84	0.72	0.16	0.656
Pelvis AIS3+ Injury Risk	Pubis Force	0.55	0.85	5.61	0.048
Overall AIS3+ Injury Risk	-	0.49	0.49	1.96	0.000

Table A2. Simulation snapshot for both models at various time

Time (ms)	M50-OS+B	F05-OS+B
0		
50		
75		
100		
150		

PEER REVIEW PAPER

This paper has been peer-reviewed and published in a special edition of Traffic Injury Prevention 24(S1), by Taylor & Francis Group. The complete paper will be available on the Traffic Injury Prevention website soon. To access ESV Peer-reviewed papers click the link below
<https://www.tandfonline.com/toc/gcpi20/24/sup1?nav=toCList>

INFLUENCE OF TIME CONSTANTS AND DIRECTIONAL INTERACTION OF A KINEMATICS-BASED BRAIN INJURY METRIC ON ITS PREDICTIVE CAPABILITY OF BRAIN STRAIN RESPONSE IN CAR CRASHES

Toshiyuki, Yanaoka

Honda R&D Co. Ltd.

Japan

Paper Number 23-0183

ABSTRACT

Among the studies focusing on criteria for brain injuries induced by the rotational motion of the head, one of the recent studies has compared the predictive capability of various injury criteria proposed by different studies, with the results showing that the best predictor depends upon specific impact configurations. This suggests the need for a more robust injury criterion across a variety of impact configurations with different duration of an impact event. The aim of this study is to investigate the effect of incorporating additional time constants and modifying directional interactions on the predicting accuracy of the physical model-based criterion called CIBIC (Convolution of Impulse Response for Brain Injury Criterion) proposed by the author's group.

A Maxwell model was parallelly added to the simplified physical model (standard linear solid) of the CIBIC criterion to improve the time-dependent responses. One simplest candidate formulation of the cross-terms was tried to replace the originally used root sum square to combine the three components of the strain. The Global Human Body Models Consortium (GHBMC) head/brain model was used to obtain the target response of the maximum principal strain (MPS). A step function with the magnitude of 10,000 rad/s² was used to optimize the spring and damping coefficients. The spring and damping coefficients were optimized by maximizing the CORA (CORrelation and Analysis) score. The modified CIBIC was further validated against the GHBMC model using a total of 256 time histories of the head rotational acceleration representing those of the four groups of load cases (occupants in full-frontal, oblique-frontal and side impacts as well as pedestrian impacts). The coefficient of determination calculated from the correlation of peak MPS and the average value of the CORA score were compared between the original and the modified CIBIC.

The modified CIBIC with the modified time constants was found to improve both assessment metrics for all of the four groups of the load cases, while both assessment metrics predicted by the modified CIBIC with the directional interaction was not improved.

The effect of the modifications shown by the modified CIBIC suggest that further consideration of the directional interaction is needed to develop a robust criterion, requiring thorough investigations on the method to combine the responses of the three axes.

INTRODUCTION

According to the Japanese accident statistics [1], the percentage of number of the fatalities sustaining the head injury as the major part of physical damage is 21.7% for motor vehicle occupants, 41.7% for 2-wheeled vehicle occupants, 58.2% for pedal cyclists and 53.3% for pedestrians. Since the respiratory and cardiovascular center is located in the brain [2], the traumatic brain injury (TBI) is the main causation of the death due to the head injury. Therefore, preventing the TBI is crucial to reduce the number of the fatalities in traffic accident.

The analysis on National Automotive Sampling System (NASS) Crashworthiness Data System (CDS) from 2010 to 2014 and Pedestrian Crash Data Study (PCDS) from 1994 to 1998 conducted by Takahashi et al. [3] showed that brain injury accounts for 78% and 81% of the head injuries sustaining Maximum Abbreviated Injury Scale (MAIS) in fatal occupant and pedestrian accidents, respectively. They classified the TBIs into three major categories based on the tissue failure and anticipated mechanisms; pressure and/or skull fracture (brain contusion, epidural hematoma), brain strain (subarachnoid hemorrhage, intracranial hemorrhage and diffuse axonal injury) and displacement relative to the skull (subdural hematoma). Category of the brain injuries primarily induced by the

strain are the most frequent in all of the categories for both vehicle occupants (81%) and pedestrians (78%). When considering the incompressible nature of the brain and the fact that the brain is surrounded by the closed skull, brain parenchyma can be deformed largely in rotational motion of the head compared to the translational motion of the head [4].

Head/brain FE models representing detailed structure of the brain and material properties were developed to investigate the brain injury mechanism and the predict the tissue level predictor (e.g. strain of the brain) [5 to 7]. Some studies focused on the brain injury criterion predicting the strain in the brain induced by the rotational motion of the head by using head/brain FE models [3, 8, 9 and 10]. In addition, these head/brain FE models allowed to compare the predicting capability of the brain injury criterion for the strain in the brain. Östh et al., [11] investigated the predicting capability of six injury criteria for the brain strain by using a head/brain FE model in such crash configurations as frontal impact, near-side impact, far-side impact and accident reconstruction using human body model. They found that the best criterion predicting the strain in the brain was different in each of the crash configurations. This result suggests that an injury criterion which can accurately predict the strain in the brain is needed regardless of the crash configurations.

The difference of the crash configuration makes the difference of the duration of the rotational acceleration to the head and the difference of the dominant input direction to the head. The time-dependent response predicted by the criterion is deemed important to predict the strain in the brain to cover a wider range of the duration of the rotational acceleration to the head. Therefore, in order to develop an injury criterion whose predicting accuracy of the strain in the brain is independent to the crash configuration, it may be needed to consider the time dependent response of the strain in the brain and directional interaction of the rotational input to the head. The physical model-based criterion called CIBIC (Convolution of Impulse Response for Brain Injury Criterion) proposed by the author's group [3] was developed by using one single standard linear solid model with one single time constant represented. Representation of an additional time constant may improve the prediction capability of the CIBIC. In addition, a highly three-dimensional shape and structure of the brain may require representation of a cross-term between the responses in different axes, which is not represented by the CIBIC. The aim of this study is to provide a preliminary insight into the effect of incorporating additional time constants and modifying directional interactions on the predicting accuracy of the CIBIC criterion.

METHODS

A Maxwell model was parallelly added to the simplified physical model (standard linear solid) of the CIBIC criterion to improve the time-dependent responses. The spring and damping coefficients of the modified physical model were determined to match the response calculated from the modified physical model with the strain response of the brain calculated using the 3D head/brain FE model when a step function was applied. Same as the development of the CIBIC criterion, the strain response for each axis calculated from the modified CIBIC criterion was represented by the form of convolution integral of the response of each axis when the step function was applied to the modified physical model. In order to investigate the effect of the directional interaction, one simplest candidate formulation of the cross-terms was tested to replace the originally used root sum square to combine the three components of the strain as the attempt for the first step. The effect of candidate modifications on the predicting accuracy was evaluated by comparing the correlation of the peak value between the strain response in the brain calculated from the criteria (CIBIC criterion and modified CIBIC criterion) and the strain response in the brain calculated using 3D head/brain FE model. Total 256 load cases including full-frontal, oblique-frontal, moving deformable barrier (MDB) side and pedestrian impact were used for the input to the criteria and the 3D head/brain FE model.

Identification of the coefficients of the modified physical model

Figure 1 shows the comparison of the physical model used in the CIBIC criterion and the modified CIBIC criterion. In order to match the condition in the development of the CIBIC criterion, the following use same thought as the CIBIC criterion; 1) representation of the displacement of the mass of the physical model, 2) applied acceleration to the physical model, 3) the mass of the physical model and 4) determination of the coefficients and scaling factor of the physical model. By considering the analogy, the displacement of the mass of the modified physical model

represents the strain of the brain, while acceleration applied to the bottom of the modified physical model represents the rotational acceleration applied to the head. The mass of the physical model was set to 1 kg for simplification. The coefficients K_0 , K_1 , K_2 , C_1 and C_2 were determined to match the strain response in the brain of the 3D head/brain FE model when applying a step function. Since the CIBIC criterion was developed by using the assumption that the rotational response of the 3D head/brain FE model was represented by an analogous linear viscoelastic model (generalized linear solid), there was difference in the dimension between the response calculated from the 3D head/brain FE model and the response calculated from the analogous linear viscoelastic model. The scaling factor was determined for each axis to compensate the difference of the dimension by dividing the peak value of the strain from the 3D head/brain FE model by the peak value of the displacement from the analogous linear viscoelastic model.

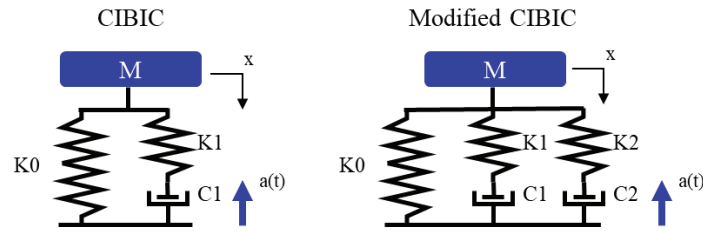


Figure 1. Comparison of the Physical model used for the CIBIC and modified CIBIC criterion

Global Human Body Model Consortium (GHBMC) head/brain FE model developed by Mao et al. [7] and shown in Figure 2 was used to obtain the target response of the strain in the brain for the determination of the coefficients and scaling factor and for the confirmation of predicting capability of the modified CIBIC criterion since this model is one of the most enhanced model. The skull, mandible and skin of the original GHBMC model was changed from deformable to rigid-body to obtain the strain response in the brain when the rigid body motion of the head was represented by the GHBMC model. Time histories of maximum principal strain (MPS) of all of the brain elements were obtained by applying time history data of the head rotational accelerations to the skull of the GHBMC head/brain FE model. Time history of the MPS in the brain (MPS_{brain}) for each load case was obtained from the time history of the MPS of the element indicating maximum of MPS in all of the brain elements over time.

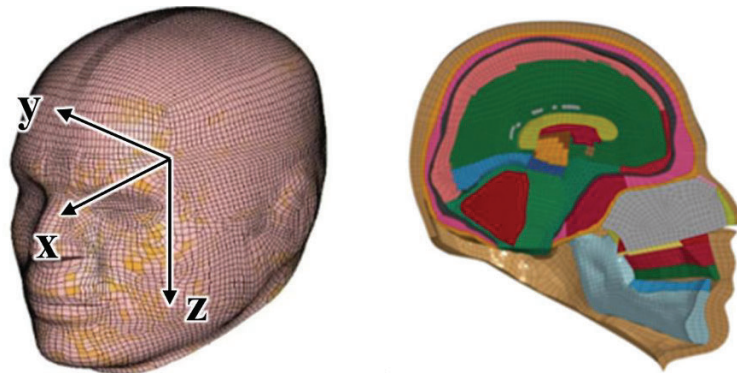


Figure 2. GHBMC head/brain model (left: local coordinate system used in this study, right: mid-sagittal section)

The coefficients and scaling factor of the modified physical model was determined for each of three axes separately. The input pulse to identify the coefficients and scaling factor of the modified physical model was a step function with $10,000 \text{ rad/s}^2$ and with 1ms duration, referring to the development of the CIBIC criterion. The coefficients of the modified physical model for each axis were optimized by maximizing the CORA (CORrelation and Analysis) score which evaluates the agreement of the time history defined by ISO/TS18571 [12]. In calculation of the CORA score, the MPS_{brain} time histories calculated from the modified physical model and the GHBMC head/brain model were normalized by their peak value to compensate the dimension difference since the rotational response of the

GHBMC model was represented by the translational response calculated from the analogous physical model. The response of the modified physical model when applying the step function input was calculated by using model-based simulation software, MATLAB/Simulink [13]. An optimization software (modeFRONTIER [14]) was used for the optimization of the coefficients by controlling the MATLAB/Simulink model on the optimization platform. The MOGA-II algorithm in the modeFRONTIER was used for the optimization of the coefficients. The scaling factor was determined such that the peak value of the MPS_{brain} time history calculated from the modified physical model is equal to that obtained from the GHBMC model.

Prediction of time history of MPS_{brain} by the modified physical model

In the CIBIC criterion, time histories of the MPS_{brain} for each axis were represented by the form of the convolution integral of the response of the physical model when applying the step function with 1ms duration. Same as the CIBIC criterion, the time histories of MPS_{brain} predicted by the modified physical model for x, y, and z axis input are represented by Equation 1, 2 and 3, respectively.

$$S_X = \int_0^t X(t - \tau)\alpha_x(\tau)d\tau \quad (\text{Equation 1})$$

$$S_Y = \int_0^t Y(t - \tau)\alpha_y(\tau)d\tau \quad (\text{Equation 2})$$

$$S_Z = \int_0^t Z(t - \tau)\alpha_z(\tau)d\tau \quad (\text{Equation 3})$$

Where S_X , S_Y and S_Z are the time histories of the MPS_{brain} predicted by the modified physical model for x, y, and z axis, respectively. And, $X(t)$, $Y(t)$ and $Z(t)$ are the response of the modified physical model when applying the step function for x, y and z axis, respectively. Furthermore, $\alpha_x(\tau)$, $\alpha_y(\tau)$ and $\alpha_z(\tau)$ are the input rotational acceleration for x, y and z axis, respectively.

Combining the strain responses of three axes calculated from the modified physical model

In order to investigate the effect of the directional interaction, in addition to the originally used root sum square to combine the three components of the strain shown in Equation 4, one formulation combining the responses for each axis was investigated as the first attempt. The additional formulation was expressed in the summation of the square of each axis and cross-terms between two axes to investigate the effect of consideration of cross-term in the simplest formulation (Equation 5).

$$MPS_{\text{brain}1} = \sqrt{S_X^2 + S_Y^2 + S_Z^2} \quad (\text{Equation 4})$$

$$MPS_{\text{brain}2} = \sqrt{S_X^2 + S_Y^2 + S_Z^2 + aS_XS_Y + bS_Y S_Z + cS_XS_Z} \quad (\text{Equation 5})$$

Where $MPS_{\text{brain}1}$ and $MPS_{\text{brain}2}$ are the MPS_{brain} calculated from the modified CIBIC (here after called the MPS_{brain} calculated from modified CIBIC-1 and 2, respectively). a, b and c are the coefficients for each cross-term. The coefficients for Equation 5 were optimized to maximize the CORA score of the MPS_{brain} response calculated from the modified CIBIC-2 against that calculated using GHBMC model when the step function with the magnitude of 10,000rad/s² and with the duration of 1 ms was applied to x, y and z axes simultaneously. The optimization was performed by using modeFRONTIER with MOGA-II optimization algorithm.

Evaluation of the improvement of the predicting accuracy

The effect of the modification on the predicting accuracy was evaluated in terms of the coefficient of determination (R^2) and the agreement of the time histories of MPS_{brain} .

ISO/TR19222 [15] evaluated the various brain injury criteria in terms of correlation of peak value of the MPS_{brain} using approximately 1,600 load cases including vehicle crash tests, vehicle sled tests and pendulum impact tests with various impact configurations. Of those load cases, the datasets of the time history of head rotational acceleration currently available in NHTSA crash test database [16] were used as the load cases for full-frontal (71 cases), oblique-frontal (49 cases) and MDB side (64 cases) impact configurations. The 72 results of the MADYMO

car-to-pedestrian impact simulations used in Takahashi et al. [3] were used as the loading condition for the pedestrian impact configuration due to the lack of the available head rotational acceleration data used in ISO/TR19222 [15]. Total 256 load cases were used for evaluation. The time duration after the main impact and rebound phase was excluded to eliminate the secondary head impact irrelevant to the crash configurations.

The correlation analysis of peak value of MPS_{brain} was performed between the GHBMC and each of the CIBIC criterion and the modified CIBIC criteria in all of the load cases along with each of four crash configurations. The CORA score of the each of CIBIC criterion and the modified CIBIC criteria against the GHBMC model was calculated for all of 256 load cases. The average values of the CORA score in all of the load cases along with each of four crash configurations were compared between the original and the modified CIBICs.

RESULTS

Identification of the coefficients of the modified physical model

Table 1 shows the five model parameters and scaling factor for each axis.

Table 1.
Five model parameters and scaling factor for each axis

Axis	K0 (N/m)	K1 (N/m)	C1 (Ns/m)	K2 (N/m)	C2 (Ns/m)	Scaling Factor for
X	2.09E+04	1.92E+04	3.35E+01	4.80E+04	8.33E+01	4.17
Y	1.43E+04	6.14E+04	2.89E+01	9.63E+04	7.02E+01	3.41
Z	1.68E+04	3.17E+04	4.57E+01	7.17E+04	2.71E+01	4.67

Combining the strain responses of three axes calculated from the modified physical model

Table 2 shows the optimized cross-term coefficients for Equation 5.

Table 2.
Three coefficients for the cross-term

Coefficients	a	b	c
$MPS_{\text{brain}2}$	0.132	0.034	0.629

Evaluation of the improvement of the predicting accuracy

Figure 3 through 7 show the correlation between the peak value of the MPS_{brain} from the GHBMC model and the criteria considered in this study (CIBIC, modified CIBIC-1 and 2) for the all of the load cases, full-frontal, oblique-frontal, MDB side and pedestrian impact configurations, respectively. Table 3 summarizes the coefficient of determination (R^2) for all of the correlation plots shown in Figure 3 through 7.

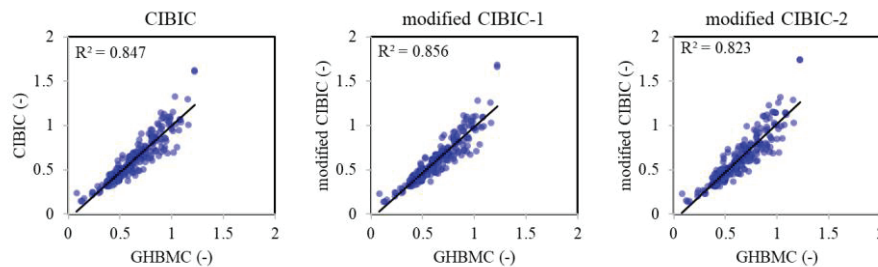


Figure 3. Correlation of the MPS_{brain} between the GHBMC and CIBIC/modified CIBIC (all of load cases)

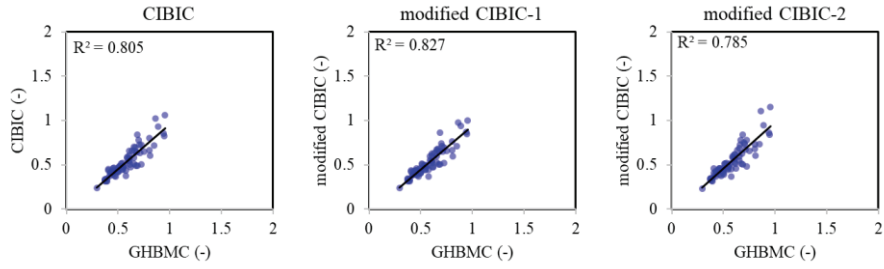


Figure 4. Correlation of the MPS_{brain} between the GHBMC and CIBIC/modified CIBIC (full-frontal)

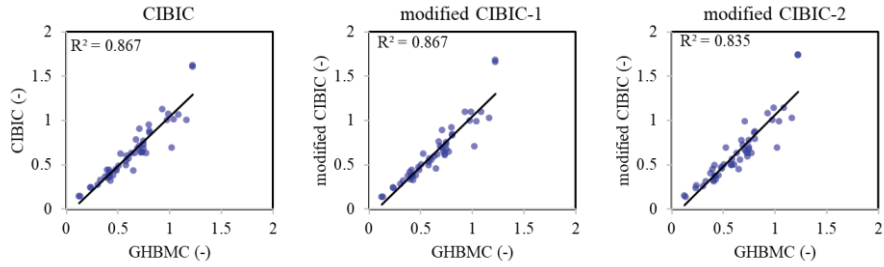


Figure 5. Correlation of the MPS_{brain} between the GHBMC and CIBIC/modified CIBIC (oblique-frontal)

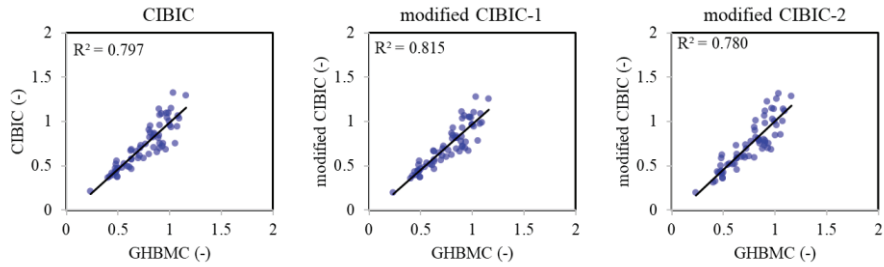


Figure 6. Correlation of the MPS_{brain} between the GHBMC and CIBIC/modified CIBIC (MDB side)

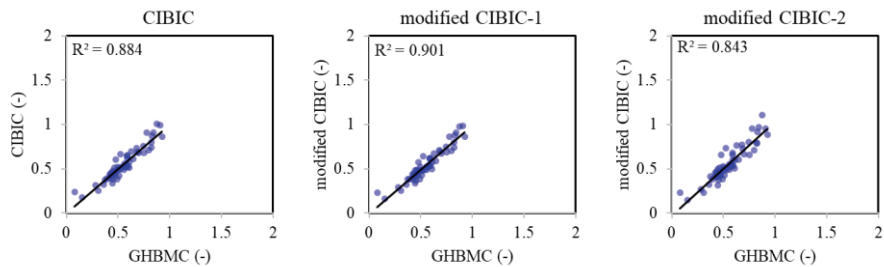


Figure 7. Correlation of the MPS_{brain} between the GHBMC and CIBIC/modified CIBIC (pedestrian)

Table 3.
Summary of coefficient of determination (R^2)

Load case	GHBMC v.s. CIBIC	GHBMC v.s. modified CIBIC-1	GHBMC v.s. modified CIBIC-2
All load cases	0.847	0.856	0.823
Full-Frontal	0.805	0.827	0.785
Oblique-frontal	0.867	0.867	0.835
MDB side	0.797	0.815	0.780
Pedestrian	0.884	0.901	0.843

Figure 8 compares the time history of the MPS_{brain} between calculated from GHBMC, calculated from the CIBIC criterion, calculated from modified CIBIC-1 and calculated from modified CIBIC-2. For the comparison of the time history, an exemplar load case was chosen for the each of full-frontal, oblique-frontal, MDB side and pedestrian impact configurations. For these three criteria, Table 4 shows the summary of the average value of the CORA score for all of the load cases along with each of the four crash configurations.

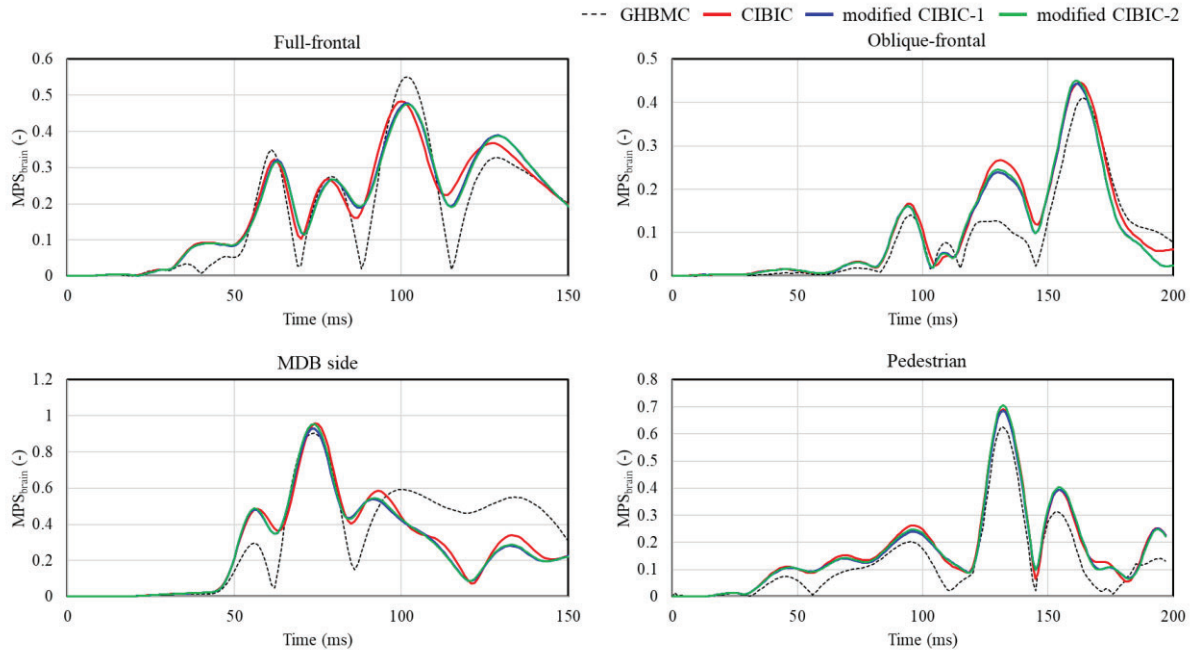


Figure 8. Comparison of the time history of the MPS_{brain} between GHBMC, CIBIC, modified CIBIC-1 and modified CIBIC-2

Table 4.
Summary of average value of the CORA score

Load case	GHBMC v.s. CIBIC	GHBMC v.s. modified CIBIC-1	GHBMC v.s. modified CIBIC-2
All load cases	0.736	0.739	0.730
Full-Frontal	0.741	0.743	0.741
Oblique-frontal	0.728	0.734	0.715
MDB side	0.657	0.658	0.645
Pedestrian	0.819	0.826	0.821

DISCUSSION

This study investigated the effect of the modification of the CIBIC criterion on the improvement of the predicting accuracy of the MPS_{brain} by changing the physical model of the CIBIC criterion and the formulation combining the response of the three axes. A Maxwell model was parallelly added to the physical model to improve the time-dependent responses. One exemplar formulation for combining the response of the three axes was used to clarify potential improvement in the directional interaction. As summarized in Table 3 and 4 for the coefficient of determination of peak value of the MPS_{brain} and the average value of the CORA score of the MPS_{brain} time history, respectively, the result of this study showed that the addition of the time constant tended to improve the predicting accuracy of the MPS_{brain} while consideration of the directional interaction by changing the combining formulation did not.

The improvement in the prediction capability by adding one time constant was 1.1% and 0.4% for the coefficient of determination of peak value of the MPS_{brain} and the average value of the CORA score of the MPS_{brain} time history in all of load cases. The small amount of improvements in the prediction capability and the high prediction capability of the original CIBIC criterion may suggest that the original CIBIC is already accurate enough, with such a simplified modeling, not to enhance its prediction capability significantly. The prediction capability was not improved with the introduction of the cross-term investigated in this study. Since only one formulation was investigated in this study, a future study needs to further investigate the influence of the formulation of combining responses in different axes.

CONCLUSIONS

The effect of one additional time constant in the simplified physical model and consideration of one exemplar cross-term on the predicting accuracy of the MPS_{brain} was investigated relative to the CIBIC criterion developed by the author's group. As a result, following were found:

- The improvements of the predicting accuracy by the modified CIBIC with one additional time constant considered in this study were 1.1% and 0.4% for the coefficient of determination of peak value of the MPS_{brain} and the average value of the CORA score of the MPS_{brain} time history in all of the load cases.
- An exemplar formulation to combine responses in different axes by introducing the cross-terms investigated in this study did not improve the predicting accuracy, requiring a more comprehensive study on the method to combine the response in three axes.

REFERENCES

- [1] National Police Agency. (2022, March 3). Table Number 2-4-2, Casualties by major part of physical damage and road user type. Traffic Accident Statistics, Annual Report 2021 (Serious accidents). https://www.npa.go.jp/publications/statistics/koutsuu/toukeihyo_e.html
- [2] Felten, D.L., O'Banion, M.K., Maida, M.S. 2016. "Netter's Atlas of Neuroscience (Third Edition)." <https://doi.org/10.1016/B978-0-323-26511-9.00011-4>.
- [3] Takahashi, Y. and Yanaoka, T. 2017. "A study of injury criteria for brain injuries in traffic accidents." In proceedings of the 25th ESV conference (Detroit, MI, USA, June 5-8), paper number 17-0040
- [4] Holbourn, A.H.S. 1943. "Mechanics of head injuries." *Lancet* 2. October 9: 438–41
- [5] Kleiven, S. 2007. "Predictors for Traumatic Brain Injuries Evaluated through Accident Reconstructions." *Stapp Car Crash J.* 51: 81-114
- [6] Takhounts, E.G., Ridella, S.A., Hasija, V., Tannous, R.E., Campbell, J.Q., Malone, D., Danelson, K., Stitzel, J., Rowson, S. and Duma, S. 2008. "Investigation of Traumatic Brain Injuries Using the Next Generation of Simulated Injury Monitor (SIMon) Finite Element Head Model." *Stapp Car Crash J.* 52: 1-31

- [7] Mao, H., Zhang, L., Jiang, B., Genthikatti, V.V., Jin, X., Zhu, F., Makwana, R., Gill, A., Jandir, G., Singh, A., Yang, K.H. 2013. "Development of a finite element human head model partially validated with thirty five experimental cases." *J Biomech Eng.*, 135(11): 111002
- [8] Takhounts, E.G., Craig, M.J., Moorhouse, K., McFadden, J. and Hasija, V. 2013 "Development of Brain Injury Criteria (BrIC)." *Stapp Car Crash J.* 57: 243-266
- [9] Yanaoka, T., Dokko, Y., Takahashi, Y. 2015. "Investigation on an injury criterion related to traumatic brain injury primarily induced by head rotation." *SAE International Technical Paper*, 2015-01-1439.
- [10] Gabler, L., Crandall, J. and Panzer, M.. 2019. "Development of a Second-Order System for Rapid Estimation of Maximum Brain Strain." *Ann Biomed Eng.* 2019 Sep; 47(9):1971-1981
- [11] Östh, J., Bohman, K. and Jakobsson, L. 2022. "Assessment of Brain Injury Criteria using Head Kinematics Data from Crash Tests and Accident Reconstructions." In proceedings of the IRCOBI conference 2022. paper number IRC-22-16
- [12] ISO. 2014. "ISO/TS 18571:2014 Road vehicles - Objective rating metric for non-ambiguous signals"
- [13] MathWorks. 2019. "MATLAB/Simulink." <https://jp.mathworks.com/products/simulink.html>
- [14] ESTECO SpA. 2022. "modeFRONTIER." <https://engineering.esteco.com/modefrontier/>
- [15] ISO. 2021. "ISO/TR 19222:2021 Road vehicles - Injury risk curves for the THOR dummy"
- [16] National Highway Traffic Safety Administration. "Vehicle Crash Test Database." <https://www.nhtsa.gov/research-data/research-testing-databases#/vehicle>

TEST METHOD FOR DEVELOPING UPDATED NECK BIOFIDELITY CORRIDORS FOR A SMALL FEMALE OCCUPANT

Corina Espelien
John Paul Donlon
Sydney Koerber
Sara Sochor
Kevin Kopp
Brian Overby
Jason Forman

University of Virginia, Center for Applied Biomechanics
USA

Paper Number 23-0197

ABSTRACT

The continued development and improvement of crash evaluation tools for a variety of anthropometries, especially the small female, call for experimental testing to generate anthropometric-specific biofidelity targets. The effect of active musculature on head and neck response in impact loadings cannot be ignored, but data from volunteer testing at impact severities performed in the 1960s and 1970s at the Naval Biodynamics Laboratory (NBDL) is limited to the male response. To generate biofidelity targets for the head and neck response of the small female that include the effect of active musculature, modern testing must rely on combining PMHS data from different anthropometries and retrospective analysis of the original NBDL testing outputs and other volunteer studies. This paper describes the methodology to replicate the original NBDL testing for small female and average male PMHS for the purpose of informing new biofidelity corridors for the 5th percentile female neck.

Publications related to the original testing were reviewed for qualitative and quantitative measures detailing the setup of the NBDL configuration. A custom buck with an upright seat (90° between seatpan and seatback), five-point rigid harness, footpan, and tether head support system was designed and fabricated for use with an acceleration sled. Of critical importance, the head and neck angle in the PMHS tests will be matched to NBDL initial positioning of -0.9° for head and 20.75° for neck. Two input pulse severities for frontal PMHS testing were chosen: a low severity at 3g peak acceleration and a moderate severity at 8g peak acceleration. These curves were chosen to avoid damage or injury to neck structures and to investigate the head and neck response at multiple severities. The boundary conditions on the sled will be measured via load cells and the PMHS kinematics will be measured through bone-mounted instrumentation packages and motion tracking arrays. This methodology will be used in experimental testing of small females and average males in the NBDL frontal impact condition.

INTRODUCTION

Crash evaluation tools, like anthropomorphic test devices (ATDs) or human body models (HBMs), often use tests performed at the Naval Biodynamics Laboratory (NBDL) as part of surrogate neck response validation [1–4]. The NBDL tests exposed volunteers to sled acceleration pulses in frontal and lateral impact loading conditions [5,6]. The resulting dataset is unique because it captured the effect of musculature by testing volunteers, but the severities of the exposures are likely non-repeatable in modern-day volunteer protocols. The NBDL volunteers were mid-size males of military age. Development of the THOR ATDs and introduction of programs to supplement physical crash tests with computational HBMs have highlighted the need for biofidelity targets for anthropometries outside of the average male response [7]. One of the anthropometries of interest is typically the small or 5th percentile female, especially for physical test surrogates (e.g., Test device for Human Occupant Restraint (THOR)-05F).

Translating the head and neck kinematic data from volunteer NBDL tests to the small female anthropometry has typically relied on equal-stress/equal-velocity scaling using ratios of mass and length scales between the original and target anthropometry [8]. The validity of this scaling method cannot be directly assessed, as modern small female volunteer tests at the NBDL severities are likely not possible. Small female post-mortem human surrogate (PMHS) testing replicating the NBDL configuration can potentially fill this gap, providing a translation bridge via mid-sized male PMHS tests performed in the NBDL configuration. Performing average male PMHS testing allows for a direct comparison of volunteer and PMHS male kinematics with matched anthropometry; performing small female PMHS

testing allows for a direct comparison of average male PMHS and small female PMHS kinematics and allows for an indirect comparison to average volunteer male kinematics.

This paper will describe an updated methodology to collect small female PMHS data in the NBDL condition for frontal impacts, and to generate biofidelity targets for small female head and neck response. Limitations of the original NBDL dataset, as well as implemented mitigations and remediations for the PMHS test series, are described. This test series will be the first to test small female PMHS in the NBDL test configuration.

METHODS

Accessing and Using the NBDL Data

Information on the NBDL dataset is documented in various conference proceedings, journal articles, and reports. There are several publications describing the original NBDL testing, including original methodology and preliminary results [5,6,9–12], subsequent testing and analyses [13–16], and summaries of the series as a whole [17,18]. It should be noted that similar volunteer testing to investigate the head and neck response was performed at Wayne State University [19–21]. While similar, the Wayne State tests differed from tests performed at the NBDL in terms of the sled system, boundary conditions, and instrumentation, as described by Ewing et al. 1973 [22].

Original NBDL data (e.g., kinematic curves) can be accessed via the National Highway Traffic Safety Administration (NHTSA) Biomechanics Database. For all NBDL tests, the head and upper neck kinematics were tracked with video and surface-mounted instrumentation, as well as the sled acceleration and velocity.

Reconstructing the NBDL Testing Environment

Acceleration system The NBDL testing was performed on an acceleration sled system, which was a modified version of the Wayne State Wayne Horizontal Acceleration Mechanism (WHAM) II system [10,11] and accelerated by a HYGE® accelerator [11]. Our new tests will be performed on a Seattle Safety Systems 1.2 MN ServoSled™ acceleration sled system (SESA sled).

On-board physical environment The physical NBDL testing environment is primarily described as an ‘upright seat with a rigid harness restraint’ [23]. For our new tests, a custom buck was designed and fabricated to replicate the NBDL environment, as shown in Figure 1. The buck includes a footpan (with 6 degrees of freedom (dof) load cell), seatpan (with 6 dof load cell), seatback (with upper and lower 6 dof load cells), shoulder and lap belt anchors, and an overhead tether system for head positioning. The seat was made of aluminum and the seatback consisted of two aluminum plates, separate from each other and separate from the seatpan. This design is intended for tests with small female surrogates (PMHS and THOR-05F) and average male surrogates (PMHS and THOR-50M) in both frontal and lateral impacts. To match positioning targets of the surrogates and restraint system across multiple anthropometries, there is adjustability of the footpan, seatback plates, b-pillars (shoulder belt anchors), and lap belt anchors. The instrumentation and measurement systems on the sled include buck accelerometers, the load cells mentioned above, a drop-release mechanism for the head-support tether system, and two on-board high speed cameras.

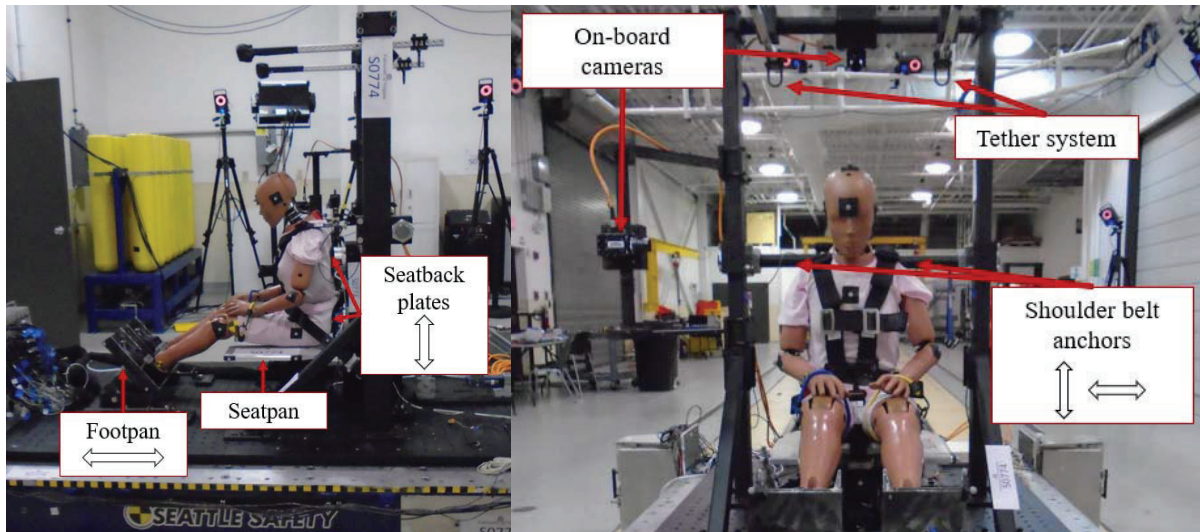


Figure 1. Lateral (left) and anterior (right) views of buck on sled with Hybrid III 5th ATD.

Restraint system A five-point harness (symmetric shoulder and lap belts, with center lap belt, connected through buckle near the umbilicus) was constructed based on that used in the NBDL tests. The harness can be adjusted to fit small females and average males. No pre-tensioning or load-limiting mechanisms were implemented in the restraint system. During positioning, the belts were tightened to a snug fit and the loads were recorded. To accommodate for potential differences with normal automotive seatbelt webbing, belt tension load gauges were tested with this webbing using a material test machine (Figure 2). The offset between the Instron load cell and belt gauge reading is used to correct belt gauge readings from sled tests to ensure accurate belt tension reporting. Lastly, the arms of the subject were restrained to avoid flailing or the arms contacting the head instrumentation packages and minimize obfuscating motion tracking markers.

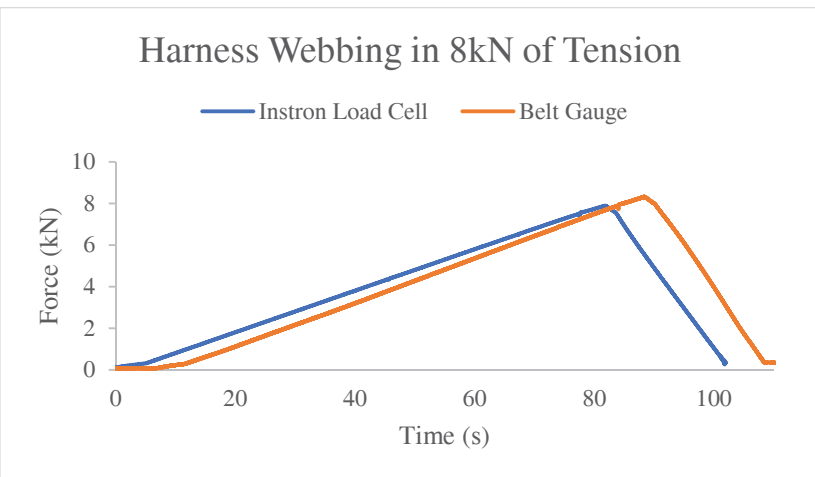


Figure 2. Harness webbing tensile test setup (left) and force time-history of Instron[®] uniaxial tensile tester load cell and supplemental belt gauge (right).

Initial positioning There is little quantified or measured detail on the initial positioning for individual NBDL runs, other than the initial positions recorded in the photos and videos. Preliminary qualitative comparisons were made to the original photos to ensure that the initial position is generally similar (Figure 3).

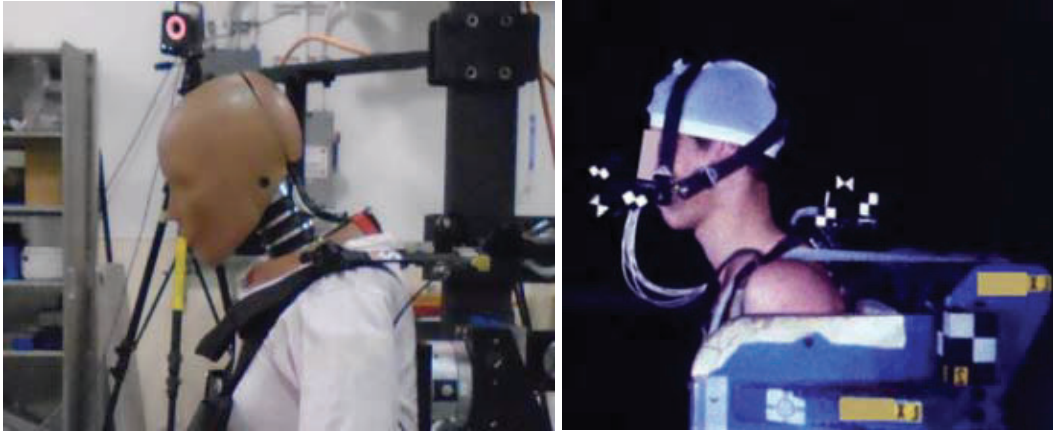


Figure 3. Qualitative comparison of upright postures of the Hybrid III 5th ATD (left) and NBDL volunteers (right; original image flipped for comparison) [16]. Note that although the head angle of the Hybrid III is different than the volunteer (due to the limited adjustability of the occipital condyles), the neck angle is relatively similar.

While no initial positioning was reported for the subjects and runs used to generate the sled pulses described in Table 3 of this paper’s results, NBDL did perform a sensitivity study regarding head and neck position on earlier subjects and test runs under 6g and 10g pulses [11]. The four categories of initial position were “neck up, chin up” (“NUCU”), “neck up, chin down” (“NUCD”), “neck forward, chin up” (“NFCU”), and “neck forward, chin down” (“NFCD”) (Figure 4). The photo targets of the surface-mounted instrumentation were transformed to anatomical origins of the head and T1, from which the head and neck angles relative to the global (lab) coordinate system were defined (Figure 5). The mean head and neck angles for thirteen subjects for two severities considered by Ewing et al. 1975 are listed in Table 1. The planned PMHS tests will be performed to match the “NUCU” condition; this position was used in later test runs, including the runs used to refine the target sled input pulses. Specifically, the mean of the head and neck angles from the 6g and 10g tests will be targeted (-0.9° for head, 20.75° for neck).

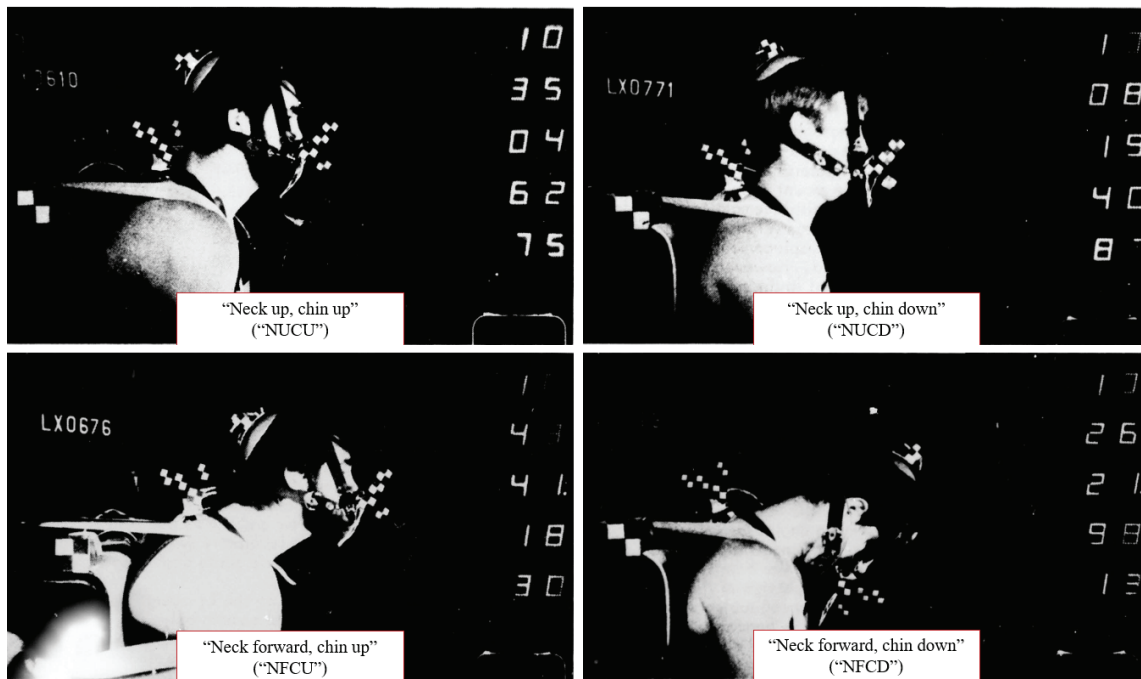


Figure 4. Initial positions considered in NBDL investigation [11].

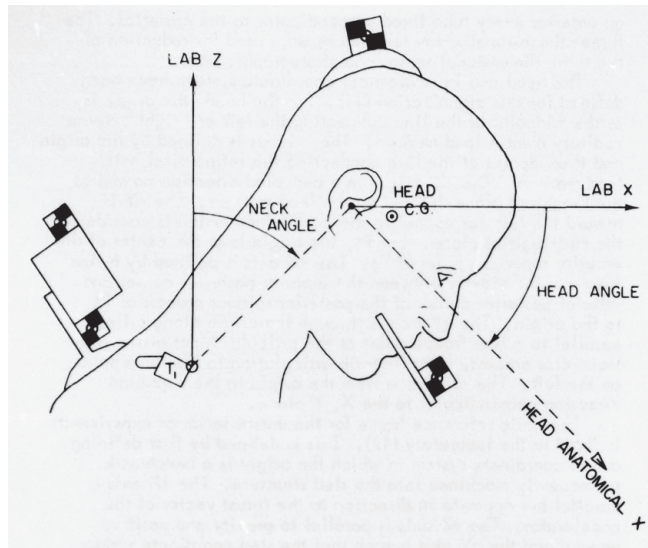


Figure 5. Definitions of head and neck angles for initial positions [11].

Table 1.

The mean (standard deviation) head and neck angles (degrees) for two severities of tests in different initial positions from $n = 13$ subjects.

	NUCU	NUCD	NFCU	NFCD
6g – head angle	-1.29 (7.15)	6.15 (11.02)	-3.74 (10.10)	66.04 (10.65)
6g – neck angle	20.22 (3.35)	12.19 (9.67)	43.29 (6.55)	79.13 (13.69)
10g – head angle	-0.48 (10.68)	6.87 (10.43)	4.32 (10.96)	64.18 (13.10)
10g – neck angle	21.28 (8.27)	12.90 (10.32)	45.07 (10.06)	74.08 (15.59)

To assist future validation work of ATDs and HBMs, detailed positioning measurements of the PMHS and restraint system will be documented. This includes head and neck positioning based on instrumentation mounts that are rigidly attached to the skull and T1 vertebra. Additionally, a pre-test static x-ray of the head and neck will be performed after final positioning to document the initial positions of the skull and vertebrae.

Reconstructing the NBDL Pulses

Pulse selection A variety of input pulses were considered representing multiple past volunteer tests, ranging from 3g to 15g peak accelerations present in the NBDL tests [17]. The original tests show that the neck response may be sensitive to input pulse severity [17]. Therefore, testing PMHS at multiple severities may be warranted. In addition to lower severities, impact severities should also be selected based on pulses that will generate maximal neck flexion (e.g., generate the most head and neck motion) to bound the extreme response. This desire for an extreme bound must also be balanced with the injury tolerance of the neck, ensuring that the tests do not damage structures related to neck flexion in a way that would adversely affect the biofidelity corridor (i.e. even the high-severity tests should ideally be non-injurious). To identify the potential threshold for injurious loading, previous sled tests with matched small female and average male PMHS performed at UVA were reviewed for neck injuries. Table 2 describes the examined tests and resulting injuries. In addition to these observations, PMHS tests in the NBDL configuration performed at the University of Heidelberg noted neck injuries in 9 of the 13 runs performed across 11g to 15g peak sled acceleration [15]. From this data, the possibility of neck injuries in small females restrained in a three-point load-limited automotive belt appears to increase around a peak sled input acceleration of 9g. For a small female restrained by a rigid five-point harness, the likelihood of injury could be similar, if not greater (due to the increased restraint of the torso). Therefore, to stay below an injurious threshold, the maximum input sled peak acceleration selected for our small female PMHS tests was 8g. To investigate the sensitivity of the head and neck response to input sled severity, an additional input sled pulse with a peak acceleration of 3g was also selected.

Table 2.
Noted neck injuries from previous PMHS testing with an automotive three-point belt.

Sample	Sled peak accel.	Sled Δ velocity	Restraint details	UVA Run ID: Reported neck injuries
n = 2 females	4g	10 km/h	3-pt belt No load-limiter	470: anterior longitudinal lig. disruption (likely due to prep)
n = 3 females	6g	20 km/h	3-pt belt 1.3 kN load-limiter	None
n = 10 female	9g	30 km/h	3-pt belt 2 kN load-limiter	210: right C5/C6 facet capsule tear 211: left C5/C6 facet capsule tear 213: right C3/C4 facet joint disruption/instability 374: bilat. C7/T1 facet capsule tear, inter/supra-spinous lig. disruption
n = 3 male	9g	30 km/h	3-pt belt 3 kN load-limiter	302: bilat. C7/T1 facet dislocation, ligament disruptions 303: right C7/T1 facet disruption, C7 body fx (flexion), ligament disruptions

For each PMHS, the 3g pulse will be run prior to the 8g run. To check for injuries between sled runs performed on the same PMHS, post-run x-rays and physical examinations will be performed. To check for injuries after the 8g run, CT and autopsy will be performed.

Limitations of Original NBDL Data and Implemented Changes

Subject anthropometry Test subjects in the NBDL series were male volunteers from the U.S. military. As mentioned previously, this study aims to supplement the existing knowledge of male volunteer response with average male and small female PMHS in the NBDL configuration.

Instrumentation uncertainties There are instrumentation uncertainties in the NBDL data regarding attachment, tracking, and timing. The head and neck kinematics have been corrected by video analysis previously in literature by Thunnissen et al. [16], used subsequently for development of THOR-50M neck biofidelity targets [1]. For this study, PMHS kinematic data of the head and T1 will be captured by accelerometers and angular rate sensors at 10,000 Hz and motion capture data at 1,000 Hz. Motion capture data will be acquired with an optoelectronic motion capture system consisting of 20 cameras (Vicon MXTM, VICON, Centennial, CO, USA) and four-marker arrays rigidly attached to the skull and T1. Acquired kinematic data will be transformed using rigid body mechanics and coordinate transformations at each time step to track the corresponding skeletal landmarks. This method has been used in previous PMHS sled test studies [12]. While the restraint system ideally couples the surrogate to the seat with minimal displacement of the pelvis and torso, there may be some forward excursion. A right and left string potentiometer attached to the seatback assembly will be attached to the pelvis to measure any forward pelvis excursion.

For ATD neck evaluation, the time-histories of the head resultant acceleration, head x- and z-axis motion, head angle, and neck angle as well as ‘head lag’ (head vs. neck angle) and ‘moment-angle’ (moment about the occipital condyles vs. head-neck angle), will be assessed. For the calculation of the moment about the occipital condyles (M_{OC_y}), the free body diagram in Figure 6 and Equation 1 are used, including terms for the mass and moment of inertia of the head (m_H and I_{yy}), the distance between the head center of gravity and the occipital condyles ($x_{OC} - x_{CG}$ and $z_{OC} - z_{CG}$), and the kinematics of the head (a_x , a_z , and α_y). If and when the chin contacts the chest, another force is introduced and the calculation in Equation 1 is no longer valid. Therefore, the time of chin-to-chest contact will be recorded (via contact switch) to define the cutoff of moment-angle curves used for neck biofidelity assessments.

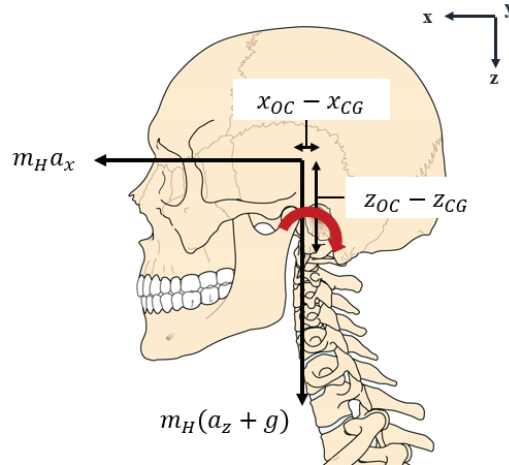


Figure 6. Free body diagram for calculation of the moment about the occipital condyles with forces and moment arms.

$$M_{OC,y} = I_{yy}\alpha_y - m_H a_x (z_{OC} - z_{CG}) - m_H (a_z + g)(x_{OC} - x_{CG}) \quad \text{Equation (1)}$$

RESULTS

Reconstructing NBDL Pulses

Two characteristic pulses were reconstructed at nominal peak accelerations of 3g and 8g by averaging the runs in Table 3. These nominal severities have a high sample size of runs in the original NBDL tests consisting of individual volunteers tested at all severities in similar initial positions, namely the “neck up chin up” (NUCU) position [17]. The resulting curves are shown in Figure 7. These curves were modified for input into our SESA sled software by left-shifting by 35 ms (to eliminate the initial zero acceleration portion of the curve), inverting, and extrapolating the curves, as needed to return to zero acceleration.

Table 3.

The run numbers from the original NBDL series used to generate the characteristic input pulses for our PMHS tests. The NBDL subject IDs, as well as the original NBDL run numbers (‘Ref #’ in NHTSA biomechanics database) are listed, with the NHTSA biomechanics database test number in parentheses.

Subject ID	Nominal 3g run(s)	Nominal 8g run(s)
H00118	LX3796 (1547)	LX3886 (1590)
H00120	LX3793 (1545)	LX3882 (1587)
H00127	LX3794 (1546)	LX3883 (1588)
H00131	LX3804 (1552) LX3840 (1570)	LX3894 (1594)
H00132	LX3805 (1553)	LX3997 (1649)
H00133	LX3798 (1549) LX3841 (1571)	LX3895 (1595)
H00134	LX3807 (1554) LX3842 (1572)	LX3890 (1593)
H00135	LX3808 (1555)	LX3898 (1596)
H00136	LX3809 (1559)	LX3901 (1597)

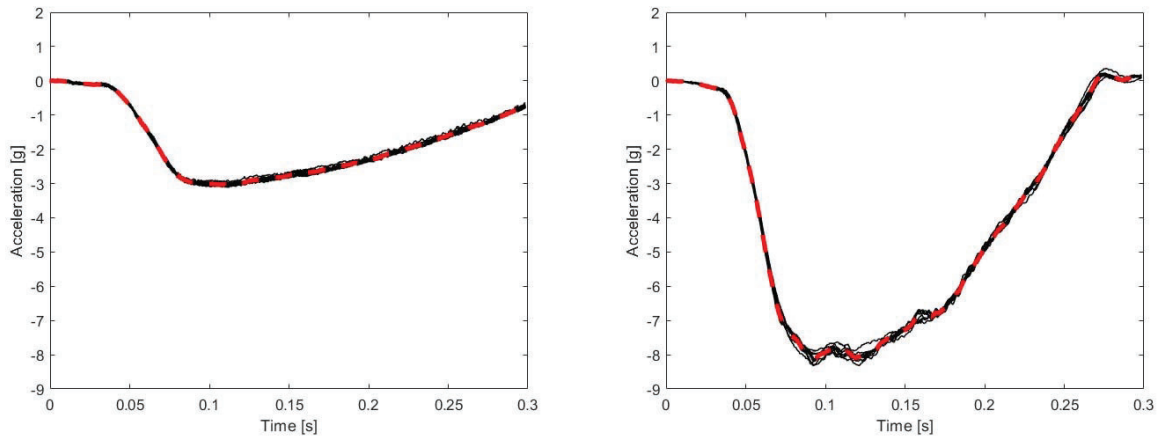


Figure 7. The original NBDL input sled pulses (black) and the averaged curves for PMHS tests (red) for the 3g (left) and 8g (right) severities.

Subject Anthropometry for Planned PMHS Tests

Table 4 describes the anthropometries of the planned PMHS tests to evaluate frontal neck flexion, which includes multiple small female PMHS and average male PMHS. The target mass and stature ranges for the small female subjects were 39-54 kg and 147-162 cm, respectively. Four of the subjects listed were over the mass target (of which one was within the target stature, two were on the border of the target stature, and one was over the target stature). The target mass and stature ranges for the mid-size males were 67-84 kg and 169-182 cm, respectively, to match reported anthropometry for NBDL volunteers [10,12,23]. All PMHS have been obtained and treated in accordance with the ethical guidelines established by the National Highway Traffic Safety Administration in Order 700-5, and all testing and handling procedures were reviewed and approved by the Institutional Review Board for Human Subjects Use established for the University of Virginia Center for Applied Biomechanics (Charlottesville, VA, USA).

*Table 4.
Planned PMHS IDs and anthropometries.*

UVA Subject ID	Sex	Age	Mass (kg)	Stature (cm)
982*	Female	78	63.0	170.2
1018	Female	77	61.2	162.6
1042	Female	75	49.9	160.0
1046	Female	69	58.0	162.6
1048	Female	71	42.6	165.1
TBD (pending)	Female	69	56.2	152.4
TBD (pending)	Female	84	45.4	165.1
1031	Male	76	76.6	172.7
1032	Male	72	74.4	177.8
1038	Male	62	67.6	177.8

*May be used as alternate if six small females cannot be acquired.

DISCUSSION

A critical review of the existing literature regarding the NBDL test series was performed. The limitations of the original testing motivated the current study and were addressed in the methodology proposed for PMHS tests. These improvements pertain primarily to an inclusive subject anthropometry, more robust instrumentation and data acquisition, and more thorough documentation of the methodology for reproducibility. Extensive consideration was given to replicating the original boundary conditions of the NBDL test series to allow for comparison between the

historical volunteer testing and the planned PMHS testing of small females and average males, especially regarding initial positioning of the head and neck.

In the NBDL test series, lateral and oblique impact loadings were also investigated. This paper only reviewed the frontal impact volunteer tests and discussed the planned methodology for the corresponding PMHS tests. The buck and test equipment described for the PMHS tests were designed explicitly for adjustment to lateral and oblique impact directions. Therefore, the same review, analysis, and matched PMHS testing can be performed to establish response corridors for the head and neck for other impact loading directions.

Understanding how to relate the outputs of the original NBDL tests series and the current PMHS test series is not trivial. There are several innate differences in the studies, especially regarding the surrogates used. To generate biofidelity corridors that include the effect of active musculature for a variety of anthropometries (e.g., small females), functional data analysis is being considered to explicitly examine the explanatory variables, such as surrogate type (volunteer vs. PMHS), anthropometry (e.g., sex, stature, mass), and pulse severity. By doing so, the effect of active musculature may be isolated and used to supplement the biofidelity targets from the PMHS tests.

CONCLUSIONS

A methodology was developed to test multiple anthropometries of PMHS in a replicated NBDL configuration, with a focus on generating head and neck biofidelity corridors for the small female that include the effect of active musculature. The modern test series will introduce improvements to the NBDL methodology to mitigate data and knowledge gaps from the original test series. By addressing the data gaps described, we aim to develop small female neck biofidelity corridors that are applicable in multiple scenarios, accounting for a range of severities and muscle activation levels, which can be used in the development of ATDs and HBMs.

ACKNOWLEDGEMENT

US Department of Transportation National Highway Traffic Safety Administration provided both technical and financial support via Contract No. 693JJ921F000180. The opinions, findings, and conclusions expressed in this publication are those of the authors and not necessarily those of the Department of Transportation or the National Highway Traffic Safety Administration. The United States Government assumes no liability for its contents or use thereof.

REFERENCES

1. Parent, D., Craig, M. & Moorhouse, K. Biofidelity Evaluation of the THOR and Hybrid III 50th Percentile Male Frontal Impact Anthropomorphic Test Devices. *Stapp Car Crash Journal* **61**, 227–276 (2017).
2. Wang, Z. J. Biofidelity Report of the THOR 5th Percentile Anthropomorphic Test Device. 165.
3. Elemance, LLC. *GHBMC M50-O Version 6.0 Users' Manual*. (2021).
4. Elemance, LLC. *GHBMC F05-O Version 5.1 Users' Manual*. (2020).
5. Ewing, C. L., Thomas, D. J., Beeler, G. W., Patrick, L. M. & Gillis, D. B. *Dynamic Response of the Head and Neck of the Living Human to —G_x Impact Acceleration*. <https://www.sae.org/publications/technical-papers/content/680792/> (1968) doi:10.4271/680792.
6. Ewing, C. L. *et al.* Dynamic Response of the Human Head and Neck to +G_y Impact Acceleration. in 770928 (1977). doi:10.4271/770928.
7. United States. Department of Transportation. National Highway Traffic Safety Administration. Office of Advanced Vehicle Safety Research. *Interim Report to Congress — Crash Test Dummies*. <https://rosap.nhtl.bts.gov/view/dot/64706> (2022).
8. Lee, E. L. *et al.* *Biomechanical Response Manual: THOR 5th Percentile Female NHTSA Advanced Frontal Dummy, Revision 2*. <https://rosap.nhtl.bts.gov/view/dot/43641> (2020).
9. Ewing, C. L., Smith, M. J., Beeler (Jr), G. W., Patrick, L. M. & Laboratory (U.S.), D. J. T. (Of the N. A. M. R. *Living Human Dynamic Response to -G_x Impact Acceleration: Accelerations Measured on the Head and Neck. II*. (Naval Aerospace Medical Research Laboratory, Naval Aerospace Medical Institute, Naval Aerospace and Regional Medical Center, 1970).
10. Ewing, C. L. & Thomas, D. J. *Human Head and Neck Response to Impact Acceleration*. <https://apps.dtic.mil/sti/citations/AD0747988> (1972).
11. Ewing, C. L. *et al.* *The Effect of the Initial Position of the Head and Neck on the Dynamic Response of the Human Head and Neck to -G_x Impact Acceleration*, . <https://apps.dtic.mil/sti/citations/ADA043031> (1975).

12. Ewing, L. *et al.* Effect of Initial Position on the Human Head and Neck Response to +Y Impact Acceleration. *SAE Transactions* **87**, 3151–3165 (1978).
13. Wismans, J. & Spenny, C. H. Head-Neck Response in Frontal Flexion. *SAE Transactions* **93**, 916–926 (1984).
14. Wismans, J., Philippens, M., van Oorschot, E., Kallieris, D. & Mattern, R. Comparison of Human Volunteer and Cadaver Head-Neck Response in Frontal Flexion. *SAE Transactions* **96**, 1323–1335 (1987).
15. Kallieris, D., Mattern, R., Wismans, J. S. H. M., & United States. National Highway Traffic Safety Administration. *Comparison of human volunteer and cadaver head-neck response in frontal flexion*. <https://rosap.ntl.bts.gov/view/dot/29928> (1988).
16. Thunnissen, J. G. M., Wismans, J. S. H. M., Ewing, C. L. & Thomas, D. J. Human Volunteer Head-Neck Response in Frontal Flexion: A New Analysis. *SAE Transactions* **104**, 3065–3086 (1995).
17. Spenny, C. H. & John A. Volpe National Transportation Systems Center (U.S.). *Analysis of Head Response to Torso Acceleration. Vol. I - Development of Performance Requirements*. <https://rosap.ntl.bts.gov/view/dot/11956> (1987).
18. Rife, J. P. *Impact acceleration and the human response: a history of the Naval Biodynamics Laboratory*. (U.S. Army Aeromedical Research Laboratory USAARL, 2018).
19. Mertz, H. J. & Patrick, L. M. Strength and Response of the Human Neck. in *Stapp Car Crash Conference Proceedings* vol. 15 207–255 (1971).
20. King, W. & Mertz, H. J. Human Impact Response: Measurement and Simulation. in (General Motors Research Laboratories, 1972).
21. Patrick, L. M. & Chou, C. C. *RESPONSE OF THE HUMAN NECK IN FLEXION, EXTENSION AND LATERAL FLEXION*. <https://trid.trb.org/view/61565> (1976).
22. Ewing, C. I. & Thomas, D. J. Torque versus angular displacement response of human head to -G_x impact acceleration. *Proceedings: Stapp Car Crash Conference* **17**, (1973).
23. Ewing, C. L. *et al.* The Effect of Duration, Rate of Onset, and Peak Sled Acceleration on the Dynamic Response of the Human Head and Neck. in 760800 (1976). doi:10.4271/760800.

THE SAFER HBM – A HUMAN BODY MODEL FOR SEAMLESS INTEGRATED OCCUPANT ANALYSIS FOR ALL ROAD USERS

Bengt Pipkorn^{1,2}, Lotta Jakobsson^{2,3}, Johan Iraeus², Jonas Östh^{2,3}

¹ Autoliv Research

² Chalmers University of Technology

³ Volvo Cars
Sweden

Paper Number 23-0242

SUMMARY

The development of the SAFER human body model (HBM) started in 2008 and is still ongoing. SAFER HBM is an omni-directional model that can be tuned and scaled (morphed) to correspond to humans of different age, sex, weight, and stature. The model can be positioned to the posture of occupants, pedestrians, bicyclists, motorcyclists etc to enable analysis of road users inside as well as outside the vehicle. SAFER HBM is capable of predicting human kinematics in evasive maneuvers (low-g) as well as in crashes (high-g). The capabilities also include injury risk predictions in crashes.

The model has been thoroughly validated and used in numerous studies. Some examples: The effect of reversible pre-tensioning of the diagonal belt on occupant kinematics and injury risk for pre-crash evasive maneuvers followed by a crash, the influence of different postures and anthropometries on occupant kinematics, and the injury reducing benefits of a helmet in bicyclist to car impacts have been evaluated. Based on results from these studies, the SAFER HBM is considered to be an efficient and biofidelic tool for development and validation of protection systems for road users inside and outside the vehicle.

INTRODUCTION

Development of road user protection systems in crashes requires human surrogate tools capable of evaluating the human response for a large variation of human characteristics and crash configurations, such as impacts from all directions. Road users include vehicle occupants, bicyclists, motorcycle riders and pedestrians, or very generally any human using the road transport system. The tools should optimally be able to mimic human responses during the pre-crash phase, such as for instance posture maintenance during braking, and in the crash to predict kinematics, loads, and injury risk irrespective of crash configuration.

Protection systems for car occupants have historically been developed by means of anthropometric test devices (ATD) as human surrogates in crash testing. The ATDs are mechanical models of the human body with the inherent difficulties of representing living tissue with metal and rubber materials. In addition, the ATDs have to be robust to enable repeated use and therefore the capability to predict human fracture by means of breakable parts is limited. Injury risk is predicted by means of global measures such as chest deflection for prediction of chest injury risk (Laituri et al. 2005) or force and moment for neck injury risk (Eppinger et al. 1999). Furthermore, the ATDs are developed to predict human kinematics and injury risk for a specific crash direction, such as frontal impact for the HIII and THOR ATDs or side impact for the WorldSID and SIDII. For evaluation of safety systems for other road users, only few ATDs have been developed. One such example is the POLAR dummy which was developed for pedestrian impact evaluations (Akiyama et al. 2001).

Mathematical human body models (HBMs) are tools that can overcome some of the limitations with ATDs and have proven to be valuable tools in injury biomechanics. The mathematical HBMs, can be built as anatomically accurate computer models from magnetic resonance imaging (MRI), computed tomography (CT) and other medical scanning techniques (Gayzik et al. 2009). The models can predict how the body's bones, organs and connective tissues react to external objects and forces. Using the Finite Element (FE) method, HBMs can also represent the actual human

anatomy and material properties in detail, and internal stresses and strains of tissues in the human body can be evaluated. As such, HBMs have the potential to have advantages over ATD models also for injury prediction. An HBM can be made omnidirectional by design and can therefore predict human kinematics and injury risk for all crash directions, including those that are in-between the pure frontal, side, and rear impacts, usually referred as oblique crashes. In the HBM the injury risk can be evaluated for specific anatomical structures, which makes it possible to address injury with physical parameters related the injury mechanism and at a detailed level, such as predicting rib fracture risk by means of predicted strain in the ribs in an HBM (Forman et al. 2012).

The development of HBMs started with development of individual human body parts, such as the lower extremity, thorax, neck, and head/brain. For instance, Kitagawa et al. (2001) developed a lower extremity FE model in order to elucidate injury mechanism of the ankle and tibia in frontal impacts. Aiman et al. (1999) developed a human head/brain FE model in order to estimate the brain/skull relative displacement magnitude due to blunt head impact. The models were used to understand local injury mechanisms. However, in real-world crashes, especially fatal ones, various types of loads on the occupants may often cause multiple injuries in several body parts. For examples, occupants contact components in the vehicles such as the steering wheel, windshield, side doors, instrumental panel and/or even an adjacent occupant during the crash sequence. As a result, occupants can sustain multiple injuries, one of which sometimes can be fatal. Therefore, it is important to simulate gross motion and overall multiple injuries of the human whole body at the same time.

The first FE whole body human model was developed by Huang et al. (1994). The model had a detailed geometrical representation of the rib cage, whereas the contour of the head, neck, shoulder, pelvis. and limbs were greatly simplified. A more detailed FE whole body human model was presented by Ruan et al. (2003). The model had a much more detailed geometric representation compared to the model described above. Its geometry was primarily based on the Visible Human Project, and the topographies from human body anatomical texts. Detailed head, neck, ribcage, abdomen, thoracic and lumbar spine, internal organs, pelvis, upper and lower extremities were simulated in this model. In the European project HUMOS (Robin, 2001) a finite element whole body human model in a driving seating posture was developed. The skin, bones, muscles as well as the main organs (lungs, heart, liver, kidneys, intestine etc.) were represented in detail in the model.

At the present, there are two major, available, occupant FE-HBM families: the Global Human Body Model Consortium (GHBM) models and the Total HUMAN Modes for Safety (THUMS) models. The GHBM includes 5th female, 50th male and 95th percentile male ‘detailed’ occupant models (Park et al. 2014; Davis et al. 2015; Davis et al. 2016) and ‘simplified’ occupant models Schwartz et al. (2015). THUMS comprises 5th female, 50th male and 95th percentile male models (Watanabe et al. 2012). In addition to these two commercial models, other initiatives to create Open Source (OS) license HBMs have been pursued. For instance, a 50th female HBM, the VIVA model was developed (Östth et al. 2017). A 50th percentile male model was created by morphing of the VIVA+ 50th percentile female model. An additional HBM is the SAFER HBM, which is the focus of the present paper. The evolution of the SAFER HBM from 2008 until today is summarized. The development, validation, morphing capability, as well as the capability of the model to represent all road users are discussed. Additionally, a ribcage subsystem response validation study, with focus on rib fracture prediction is included.

THE SAFER HBM

The overall objective with SAFER HBM, formulated in 2008 is to develop an “omnidirectional, tunable and scalable human body model capable of injury risk and biofidelic kinematics prediction in high-g as well as low-g events”. It means a tool that can be used for seamless integrated occupant analysis. Targeting this, several parallel research activities have contributed to taking steps towards fulfilling this objective. The development journey of the SAFER HBM is described in this chapter, with the development of the mid-size male model summarized in the first subchapter, including the steps from car occupant model to models for other road users. This is then followed by a summary of the developments of the injury prediction capabilities and a new study demonstrating the capability of SAFER HBM to predict rib fracture risk in oblique loading. The scaling and tuning (morphing) functionalities are addressed in the subchapter of morphing, whereafter its capability to address positioning, including postural control follows. Lastly, examples of the SAFER HBMs applications are summarized.

Design

The baseline SAFER HBM corresponds to a 50th percentile male, with a weight of 77 kg and stature of 175 cm (Schneider et al. 1983). The development of the model started with modifications to the THUMS v3, for instance material properties for low-g events (Östh et al. 2012) and the ribcage (Mendoza-Vazquez et al. 2013).

In the beginning of 2017 the SAFER HBM v8, or THUMS SAFER as it was then called, was created by major updates to the head and thorax of the model, see Figure 1. The Royal Institute of Technology FE head model (KTH model, Kleiven 2007) was integrated with the SAFER HBM. The KTH head model consists of 25,000 elements, of which approximately 4,000 are solid elements belonging to the brain which is compartmentalized and with specific material properties for the regions of the brain such as the white and gray matter, the corpus callosum, the cerebellum and the cerebrospinal fluid. The head model utilizes hyperelastic Ogden materials with Prony series viscoelasticity and has been validated with respect to Post Mortem Human Subject (PMHS) data for intracranial pressure as well as for frontal, occipital and lateral impacts (Kleiven and von Holst 2002a; Kleiven and von Holst 2002b; Kleiven and Hardy 2002; Kleiven 2006), and injury risk curves for mild traumatic brain injury in the form of concussion has been developed using accident reconstructions of NFL football head impacts (Kleiven 2007; Fahlstedt et al. 2022).

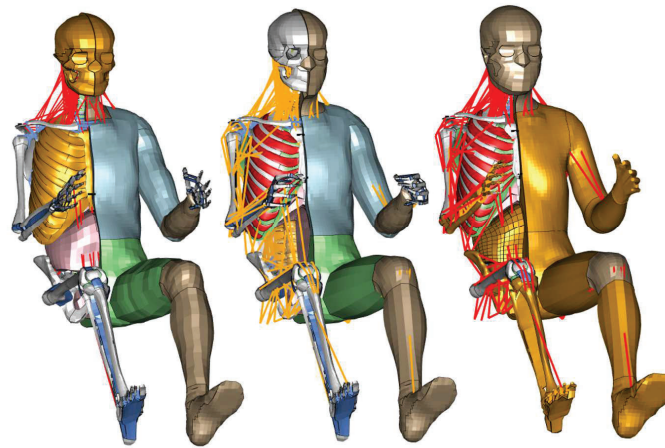


Figure 1. The three versions of the mid-size male SAFER HBM left to right; v8 (2017), v9 (2019) v10 (2020) with updates for each version highlighted in gold.

Additionally, for SAFER HBM v8 a detailed generic rib cage model was created based on a combination of in-vitro and in-vivo datasets (Iraeus et al 2020, Iraeus et al. 2019). Generic rib models were developed by defining elliptical cross sections along the rib center line. Cortical thickness, varying along and around each rib, was assigned based on the dataset presented by Choi et al. (2011). The ellipses were connected to define the periosteal and endosteal surfaces. Thereafter the ribs were meshed and morphed into the final shape based on a statistical ribcage model (Shi et al. 2014). Additionally, the sternum was re-modelled based on a geometry from another statistical shape model, (Weaver 2014). The parameters for the statistical model were adjusted to be representative of a male aged 40 years with a stature of 1,770 mm and a BMI of 25. The ribs were connected using three layers of solid elements representing the intercostal muscles (Figure 2). Validation of ribcage kinetic, kinematics and strain distribution were carried out at three levels of complexity: anterior-posterior rib bending tests; rigid impactor table-top test; and a 40km/h frontal sled test (Iraeus et al. 2019).



Figure 2. The new generic ribcage developed for SAFER HBM v8.

Further updates for the SAFER HBM were made in 2018, when the feedback postural control package (Östh et al. 2012b; 2015; Ólafsdóttir et al. 2019) developed for the model was integrated with the up until then passive HBM, creating the SAFER HBM v9 which can be used as both an active and a passive HBM through seamless control with switching parameters in the model. Feedback postural control is applied for the cervical and lumbar spine using a spatial tuning pattern for omni-directional control which was later validated for braking and lane change evasive maneuvers (Larsson et al. 2019). Soft tissue material updates were made to accommodate a combined active and passive model. For instance, the skin was converted from a linear elastic material to a non-linear material model using. Additional updates for v9 were updates of the lumbar and cervical spine, which was given new vertebral discs and ligaments, and for the cervical spine the facet joints were converted from shearing solids to sliding contact joints (Östh et al. 2020), and validation of the spinal properties were carried out with respect to functional spine unit properties, subsystem and whole-body responses in lumbar flexion-extension.

For version 10 of the SAFER HBM, created in 2020, the model had updates to the pelvis, head and brain, lower arm, and lower leg, plus the soft tissues around the torso were remeshed. The pelvis was updated based on a new statistical shape model (Brynskog et al. 2021). The KTH head model was also updated to a version also encompassing the brainstem. Additional updates were remeshing of the torso soft tissues, to create a continuous mesh over the shoulder and hip joints. The torso soft tissues were adapted to an average 50th percentile male shape (Reed and Ebert 2013; Pipkorn et al. 2021) and a major update of the contacts of the model was made to improve model reproducibility and computational efficiency (Östh et al. 2021). Furthermore, the radius, ulna, carpals, metacarpals, phalanges, and ligaments were replaced with a new model (Bayat and Pongiaporte 2020) with skeletal part based on medical images, and ligaments and joints based on literature. The radius, ulna and hand were positioned in a driving posture matching that of the existing lower arm in the SAFER HBM, and soft tissues and skin were added on top of the skeletal structure of the lower arms. The lower arm model was validated by means of impact tests (Forman et al. 2014; Dumas et al. 2003). In addition, the leg was updated. The mesh of the tibia, fibula, calcaneus, and talus of the lower legs were replaced by a pure hexahedral mesh representing the trabecular bone and a quadrilateral shell mesh representing the cortical bone. The updated lower leg geometry was based on CT-Scans from 5 females (Roberts 2020) rescaled to fit the 50th percentile male. The cortex of the intermediate bones, metatarsals and phalanges of the feet was modelled using rigid shells, replacing the original mesh, while the original ligaments and soft tissues of the lower legs were kept.

To enable evaluation of pedestrian safety the SAFER HBM v10 was positioned as a pedestrian in a walking gait (Figure 3). For bicyclist and motorcycle safety the feet of the SAFER HBM were positioned on the pedals and foot support respectively and the spine curvature was modified for the model to reach the handlebar. For the pedestrian posture the pelvis flesh was morphed to accommodate for the modification of pelvis shape when a human changing posture from a standing posture to a sitting.



Figure . The SAFER HBM v10 pedestrian

Injury Prediction

The SAFER HBM has the capabilities to predict injury risks by means of global measures such as cross-sectional forces. However, detailed biofidelic prediction of injury risk using injury metrics that are physically related to the injury mechanism is in focus. Such injury metrics can be used to predict injury risk equally well regardless of loading directions with the benefits that the same injury metric can be used to predict injury risk for all road users.

For the SAFER HBM, a strain-based probabilistic method to predict rib fracture risk with whole-body FE models was developed (Forman et al. 2012). An age-adjusted ultimate strain distribution based on cortical bone coupon testing (Kemper et al. 2005, Kemper et al. 2007) was used to estimate local rib fracture probabilities within SAFER HBM. These local probabilities were combined by means of a poisson binominal distribution to predict injury risk and severity within the whole ribcage. The strain based probabilistic rib fracture method was refined with new risk functions (Larsson et al 2021). The capability of the probabilistic rib fracture method to predict rib fracture risk was validated by means of detailed accident reconstructions and population-based reconstructions (Pipkorn et al 2019, Larsson et al 2021). Overall SAFER HBM version 10 with probabilistic rib fracture prediction method was capable to predict rib fracture risk based on the reconstructions.

For the present paper, an additional demonstration of the capability of the SAFER HBM v10 model to predict rib fracture risk was carried out by a ribcage subsystem response validation study. Oblique pendulum PMHS impact tests were reconstructed and the predicted rib fracture risk with the number of fracture ribs sustained by the PMHS were compared (Viano, 1989) (Figure 4).

In the pendulum impact simulations, the impact velocity was 4.4m/s (low severity) and 6.5m/s (mid severity), the mass of the impactor was 23.4kg and the diameter was 150 mm. The center of the impactor was aligned with the xiphoid process and rotated 30 degrees. In the PMHS test study, five tests were carried out for each impact velocity, and one female and four males were tested for each velocity. Acceleration was measured in the impactor and force was calculated from the acceleration. Force-Time corridors for oblique impacts at 4.4 and 6.5m/s were generated.



Figure 4. Validation of ribcage subsystem response by means of oblique pendulum impact tests according to Viano (1989)

The forces predicted using SAFER HBM v10 were inside or close to the experimental force-time corridors for both impact velocities (Figures 5a and 5b). In the 4.4m/s impact tests the average age of the PMHS was 46 year old and the number of rib fractures were 0.4. In the 6.5m/s impact tests the average age was 54 and average number of rib fractures were 5.4. In the corresponding simulations the SAFER HBM predicted a 2% risk for a 46 year old, and a 94% risk for a 54 year old to sustain more than 3 fractured ribs (NFR 3+) in 4.4 and 6.5m/s pendulum impacts respectively (Table I).

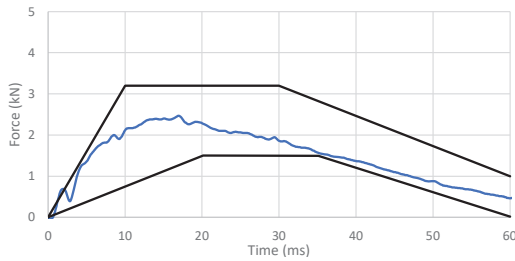


Figure 5a. Impactor force vs time for the 4.4m/s oblique pendulum impact test, corridor from Viano (1989)

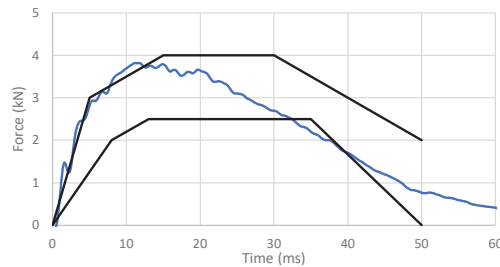


Figure 5b. Impactor force vs time for the 6.5m/s oblique pendulum impact test, corridor from Viano (1989)

Table 1.
Fractures in PMHS tests (Viano 1989) vs predicted rib fracture risk from the simulations in the oblique pendulum impact tests

Average Age	Average Impactor Speed	Average No. of Fractures	Predicted NFR3+ Risk
46 years	4.4m/s	0.4	2%
54 years	6.5m/s	5.2	94%

To compare various predictors for mild traumatic brain injuries 58 NFL head impact cases were reconstructed with the head model. A statistical correlation between numerous predictors with injury was found (Kleiven 2007). However, strain, was found to be the preferred predictor to be used to predict the risk for mild traumatic brain injury (Fahlstedt et al. 2022). The value for 100th, 99th, 95th, 90th, and 50th percentile for element and nodal averaged element strain was evaluated. It was found that 100th percentile strain with element value could give high strain due to only a few elements in a model. Therefore, the 99th percentile strain was selected to predict brain injury risk.

The capability for the lower arm model to predict fracture risk was developed by means of reconstructing two different human subject lower arm impact tests (Bayat 2020). In one configuration the arm was mounted to a force transducer and a reaction plate assembly free to move along linear guide rails. The impact load was provided by a guided mass dropped from various heights (Forman et al. 2014). In the other configuration a horizontal arm supported by two cables was impacted with a pneumatic piston at various impact velocities (Dumas et al. 2003). Based on these two test configurations with human subjects the capability to predict lower arm fracture risk by means of predicted lower arm force at the elbow was developed.

Morphing

A morphing method to enable creation of the individuals in the diverse population was selected and implemented for the SAFER HBM (Hwang, et al. 2016). The morphing method involves several steps. For a given age, sex, stature and body mass index (BMI) the external shape geometries are predicted by means of statistical geometry models developed by Reed and Parkinson (2008), while the skeleton geometries are based on other statistical shape models, ribcage (Wang 2016), pelvis femur and tibia (Klein 2015). These geometry models are further aligned to anatomical landmarks on each bone by means of a rigid registration algorithm. The predicted geometries are then used to define target landmarks, with corresponding source landmarks defined according to the baseline SAFER HBM geometry. The morphing is carried out by means of radial basis function (RBF) interpolation. By using this method, SAFER HBM can be morphed to populations of vehicle occupants to be used to develop protection systems that provides all road users with good protection.

Positioning

Starting from version 9, positioning of the SAFER HBM v9 as an occupant is carried out by the use of a dummy mechanism and a javascript in PRIMER (Figure 6) (Oasys Ltd, Sollihull, United Kingdom). The PRIMER dummy mechanism enables manipulations of the head, neck, torso, as well as the upper and lower extremities using rigid body joint definitions in PRIMER. Based on the final position 1D cable elements are created which then are used in a Marionette-method pre-simulation to position the HBM in the desired posture (Figure 6) (Poulard et al. 2015). The pre-simulation is typically 300 milliseconds long and run with global damping to generate a close to velocity free end-state for the model. After the pre-simulation, the nodal positions are read out and carried over to the baseline model, thus omitting any initial stresses and strains created in the positioning pre-simulation.

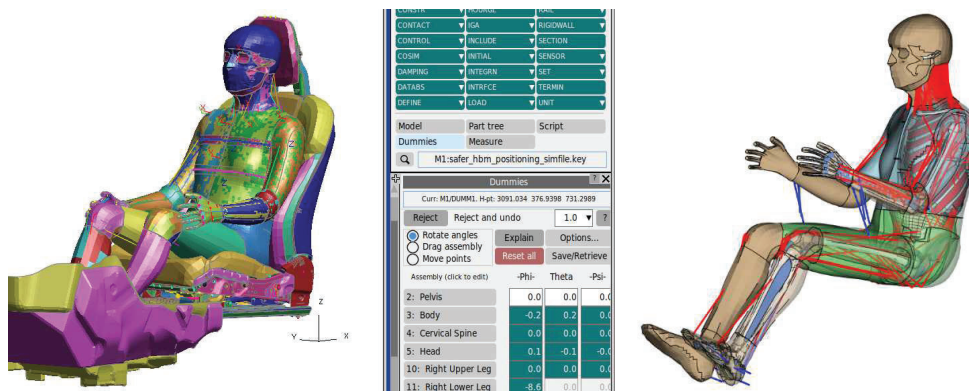


Figure 6. SAFER HBM v10 positioning using the Marionette-method and PRIMER. Left: Dummy positioning interface in Oasys Primer. Right: Initial position in Marionette-positioning pre-simulation to a passenger posture. Blue lines represent the positioning beams.

The tool is capable of modifying the posture of SAFER HBM occupant to the posture of all road users. The Marionett-method described above is used in steps to enable positioning of SAFER HBM to a pedestrian, bicyclist, or motorcyclist posture. For the lower extremities, initially the femurs are pulled to the desired position followed by the tibias.

Postural Control and Active Muscles

Real-world crashes occur in a variety of situations, often including a combination of low- and high-g events. Exemplified by braking followed by a frontal impact, a rear-end impact followed by a frontal impact, or a complex run off road crash. Creating a HBM capable of this includes several challenges, such as developing a model that is capable of predicting occupant kinematics for the low load and long duration events and injury risk for the high-g events. To enable time efficient analysis of the combined events requires careful selection of the modelling detail. The modelling detail is a compromise between the number of elements to avoid long run time while have a sufficient level of detail to enable reliable prediction of injury risk. To enable simulation of whole-sequence crash events including a low-g pre-crash phase, the first active musculature implementation for the SAFER HBM was made for an isolated arm to show proof of concept of using feedback postural control in an FE HBM (Östh et al. 2012a). The existing elbow joint in the THUMS v3 arm was replaced with a revolute joint, and the upper extremity muscles spanning the shoulder and elbow joints were modelled using line muscle elements. The updated model's passive properties were verified with respect to human subject data, and both posture maintenance and elbow perturbation experiments were simulated with the model.

The elbow model with active control was later implemented into the whole body HBM, together with postural flexion-extension controllers for the head, neck, and trunk (Östh et al. 2012b; Östh et al. 2015). The head, neck and trunk controllers were first iteratively tuned to the occupant response in light braking interventions and sled tests (Östh et al. 2012b), and some modifications to the baseline THUMS v3 were made to soften the passive model's response. Nodal constraints for skin nodes were removed, Young's modulus for the skin was softened, spinal ligament and intervertebral discs stiffness were reduced and buttocks soft tissue material was changed to the same as for the torso (Östh et al. 2012b)

To enable simulation of both driver and passenger occupants, the elbow model complemented with flexion-extension controllers for the shoulder were integrated (Östh et al. 2015) into the modified THUMS v3 which was the basis for the feedback postural control HBM at the time. The controllers were tuned through an optimization of the controller gains in a sled test series with volunteers in a driver environment, and later validated with respect to both driver and passenger volunteer responses to autonomous braking interventions (Östh et al. 2013; Ólafsdóttir et al. 2013). The head and T1 trajectories of the HBM was within one standard deviation of the average volunteer response for the simulated conditions (driver and passengers in autonomous braking, with and without a reversible pre-tensioned belt), but for most conditions the model was on the more flexible side of the volunteer responses.

In the analysis of volunteer data from both driver initiated and autonomous braking, a different type of response was found. When braking on their own, drivers extended their arms and neck, and braced prior to the braking, while during autonomous braking drivers reacted with postural response first when braking was applied (Östh et al. 2013). This was simulated with the HBM by the inclusion of open loop controlled leg musculature (Östh et al. 2014), which was prescribed published muscle activations from volunteer tests (Behr et al. 2010), in combination with a hypothesized anticipatory postural response which was modelled by using a time dependent reference signal for the postural controllers as a function of the applied acceleration. This method was successful in reproducing the driver responses, while the postural feedback control which worked well for autonomous braking was not able to do so.

To extend the analysis capability of the HBM to lateral and oblique planar movements, spatial tuning patterns for the cervical muscles were derived from volunteer tests with intramuscular electrodes in seated perturbation tests (Ólafsdóttir et al. 2015). The spatial tuning patterns were implemented into the feedback postural control scheme for the SAFER HBM (Ólafsdóttir et al. 2019), and the response of the model for both longitudinal and lateral evasive maneuvers was validated by means of volunteer data (Figure 7) (Larsson et al. 2019).

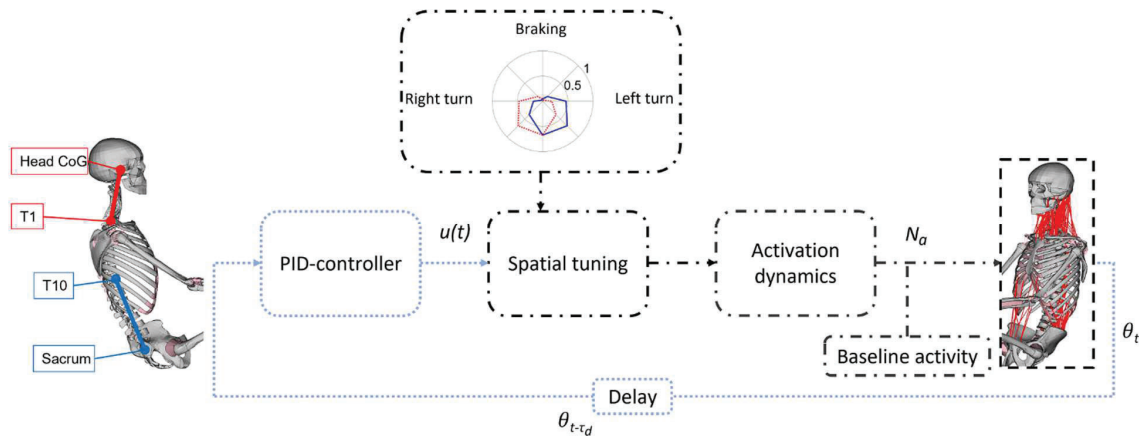


Figure 7. Schematic representation of the postural feedback control model for the SAFER HBM v10. The blue dotted lines represent signals common for the whole control system and the black dash-dotted lines represent signals on the muscle specific activation level. Adapted from Östh et al. (2022).

Recently, the active SAFER HBM v10 was used to study the effect of the feedback postural controllers on injury prediction in whole-sequence crash simulations (Östh et al. 2022), that is a pre-crash maneuver followed by a crash. The study showed that for frontal impacts, the muscle activation did not have any considerable effect on the kinematic response, however HBM injury predictions were affected in a higher acceleration frontal impact. For far-side impact, there was a moderate effect on kinematics in the form of reduced peak inboard head excursion with active muscles. The recommendation from the study was that muscle activations should also be included in the crash-phase of whole-sequence simulations to enable HBM simulation to better represent live occupants. However, as the postural control algorithm appears to give high muscle activations during the crash-phase, a strategy to hold the muscle activations constant during the crash was recommended and is used with the SAFER HBM for now.

Applications

As the first model to seamlessly predict human response in an evasive maneuver followed by a crash, the SAFER HBM was positioned in the driver seat in a vehicle interior model of a mid-sized passenger car, with an integrated restraint system in the form of a reversible pre-tensioned seat belt (Östmann and Jakobsson 2016; Saito et al. 2016). Demonstrating the feasibility to use the model, one study reported small effects on the occupant crash response from the reversible pre-tensioned seat belt (Östmann and Jakobsson 2016), while reducing the impact velocity as an effect of the pre-crash braking reduced occupant accelerations in the crash considerably. The other study showed reduced forward excursions during the pre-crash phase with increased reversible pre-tension force, as well as reduced chest deflections in the frontal impact simulated, as chest contact to the steering wheel rim was avoided when applying the reversible pre-tension (Saito et al. 2016). The capability of the SAFER HBM was further demonstrated in a more recent study (Wass et al. 2022), in which the model was used to study whole-sequence events consisting of a pre-crash braking followed by a far-side side-impact pulse. The braking intervention led to a more forward occupant position at the start of the crash phase, influencing results in the crash phase, compared to the impact only. A more forward impact point on the vehicle side resulted in 50 mm lowered lateral head excursion, compared to a mid-compartment impact configuration point.

Another strength of HBMs is that they can be used to represent a larger range of occupant positions and sizes. Several studies with the SAFER HBM have explored the influence of non-nominal seating postures and occupant sizes. Thirty-five postural variations for the 50th percentile male SAFER HBM v9 were simulated in three crash configurations representative of possible future crash scenarios (Leledakis et al. 2021). It was found that occupant postures such as crossing the legs increased pelvis excursions compared to a nominal position, that leaning inboard and outboard affected side impact kinematics considerably, as well as that resting the arm on the center console can increase inboard excursions in far-side impacts, compared to if the arm is on the outboard side of it. Expanding this study also to eleven male and female anthropometries, by morphing of the SAFER HBM v9 showed that seat fore-aft position had considerable effects on occupant speed relative to the vehicle interior in frontal impacts. Furthermore, knee restraint

(depending on seat adjustment and occupant size) had large effects on femur, pelvis, and lumbar spine loads (Figure 8) (Leledakis et al. 2022).

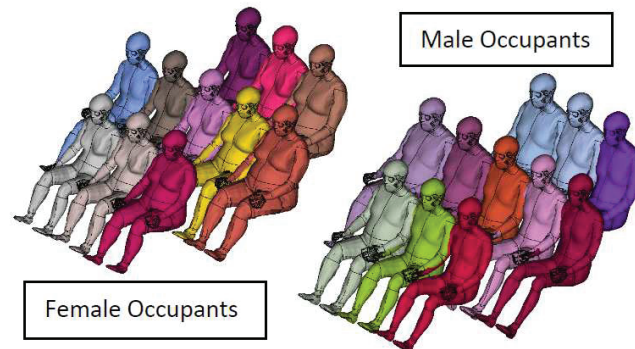


Figure 8. Eleven female and male anthropometries in the range from 1.48–1.90 m and 50–119 kg achieved through morphing of the SAFER HBM v9 and used to study occupant crash responses in four impact scenarios by Leledakis et al. (2022). Figure adapted from Leledakis et al. (2022).

SAFER HBM was also used to evaluate bicyclist safety. The potential injury reducing benefits of a bicycle helmet and bicyclist airbag mounted on the vehicle was evaluated (Pipkorn et al. 2020). SAFER HBM positioned on a bicycle model and impacted from the side in 40km/h (Figure 9). Brain injury risk was predicted by means of strain in the brain. It was found that generally head injury risk was reduced for a bicyclist wearing a helmet when impacted by a passenger vehicle in 40km/h. Additional reductions was obtained for a vehicle with a bicyclist airbag.



Figure 9. SAFER HBM v9 with helmet on bike impacted by a passenger vehicle travelling at 40km/h.

DISCUSSION

Starting with the overall objective to create a human surrogate model which is “omnidirectional, tunable and scalable with injury prediction capability, and biofidelic kinematics for high-g as well as low-g events” the SAFER HBM has become a capable tool to predict human kinematics in evasive maneuvers and in crashes, and injury risk in crashes. Validation of the capability of SAFER HBM models morphed to correspond to humans of various sex and sizes to predict human kinematics and rib fracture risk for both frontal and lateral loading is ongoing. Additional validations include the capability of the lumbar spine model to predict human lumbar spine vertebrae kinematics. Ongoing developments include tissue based risk functions for lumbar spine vertebrae and pelvis iliac wing fracture risks predictions. Additional development and validation efforts are to enhance the capability of SAFER HBM to predict occupant submarining.

The combination of the capabilities to predict human kinematics in evasive maneuvers, and to predict injury risks in addition to kinematics in crashes gives a model which is unique. The model can be used to evaluate whole-sequence crashes consisting of a pre-crash and crash phase efficiently. The level of modelling detail has been selected to be a compromise between short simulation run times and detailed representations of parts important for injury risk prediction. A pre-crash evasive maneuver can be up to 2 seconds in duration and the computer run time for an FE simulation with an HBM is roughly proportional to the number of elements. Therefore, for time efficient analysis of the pre-crash phase, an HBM comprising a minimum number of elements is preferred, still enabling biofidelic prediction of human kinematics in the pre-crash phase and injury risk prediction in the crash phase.

The latest version of SAFER HBM (v 10) contains approximately 410,000 elements. This is significantly less than the latest version of the GHBMC ‘detailed’ and the THUMS models which contain 2,3M and 1,9M elements, respectively. The relatively low number of elements in SAFER HBM makes the model an efficient tool for analysis of integrated pre-crash and crash events.

The SAFER HBM strategy is to develop a model that can be morphed to a family of models based on sex, weight, and stature that covers the population of road users. This strategy is different from the GHBMC and THUMS model development strategies in which individual models for vehicle occupants and pedestrians as well as models with fixed percentiles, such as a 5th female model, are developed (Park et al. 2014; Davis et al. 2015; Davis et al. 2016; Watanabe et al. 2012). Developing one model and morphing it to different sex, anthropometries and posture is an efficient method to create these models, as compared to developing models for fixed sex and percentiles. One of the main advantages of this strategy is that a variety of morphed models can be used to assess robust protection, by adapting for the situations and addressing equity of the population exposed.

The THUMS v3 was in 2008 capable of predicting in crash gross human kinematics (Toyota, 2008). The development of the capabilities to predict human kinematics in pre-crash events was initiated based on THUMS v3. The first studies were published in 2012, and by 2015 the SAFER HBM model was developed and validated for predicting human kinematics in autonomous and driver initiated braking maneuvers (Östh et al. 2015). The development of the capability of the model to predict pre-crash lateral evasive maneuver was the next step. For the validation, several series of volunteer tests were carried out (Östh et al. 2013; Ólafsdóttir et al. 2013; Ghaffari et al. 2018; 2019; 2021; Larsson et al. 2022). A model capable of predicting human kinematics for longitudinal as well as lateral maneuvers was available in 2017. Development of the capability of the model to predict human response for vertical load is ongoing and is expected to be finished by 2023.

Euro NCAP has announced inclusion of HBMs for virtual testing in the rating program. To enable inclusion, building trust in the models is an important challenge. Another important challenge is getting acceptance of the model in the community. SAFER HBM is a research-based tool and in order to build trust and get acceptance, the developments are documented and published in scientific journals.

HBMs have been mainly developed and used for vehicle occupant analyses. Development and validations, but not as extensive as for occupant analyses, have also been carried out for prediction of the response of road users outside the vehicle. These developments are important due to the fact that there are no commercially available mechanical human substitutes developed for analysis of road users outside the vehicle. Therefore, validated and biofidelic HBMs are sensible alternatives for analysis of road users outside the vehicle.

SAFER HBM is today an efficient tool capable of predicting human kinematics and injury risk for road users inside and outside the vehicle. In addition to the further developments and validations needed for enhancements addressing road users outside the vehicle, the refinements also include the occupants inside the vehicles, while improving the tool’s capability to predict occupant kinematics and injury risks. Challenges for occupant protection include a larger variety of seat positions, including reclined, and sitting postures, also driven by the relative increase of vehicle passenger (non-drivers) with the trends of shared mobility and potential future autonomous vehicles. A human body model designed to replicate human biomechanics and kinematics in a variety of scenarios can help assess and develop safety systems for human-centered real-world protection.

ACKNOWLEDGEMENT

This work has been carried out at SAFER Vehicle and Traffic Safety Centre at Chalmers, Sweden and is partly financed by FFI (Strategic Vehicle research and Innovation) by VINNOVA, the Swedish Transport Administration the Swedish Energy Agency and the industrial partners within FFI.

REFERENCES

- Akiyama, A., Okamoto, M., and Rangarajan, N. (2001). Development and application of the new pedestrian dummy. Proceedings of the 17th Conference on Enhanced Safety of Vehicles.
- Bayat, M., and Pongiaporre, N., (2020). Arm Injury Prediction with THUMS SAFER. Master Thesis KTH Royal Institute of Technology, School of Engineering Sciences, Stockholm, Sweden
- Behr, M., Poumarat, G., Serre, T., Arnoux, P. J., Thollon, L., and Brunet, C. (2010). Posture and muscular behaviour in emergency braking: An experimental approach. *Accident Analysis and Prevention*, 42(3), 797-801.
- Brynskog, E., Iraeus, J., Reed, M. P., and Davidsson, J. (2021). Predicting pelvis geometry using a morphometric model with overall anthropometric variables. *Journal of biomechanics*, 126, 110633.
- Choi, H.-Y., and Kwak, D.-S. Morphologic Characteristics of Korean Elderly Rib. *J. Automot. Saf. Energy*, 2011. 2(2): p. 122-12
- Davis, M. L., Vavalle, N. A., and Gayzik, F. S. (2015, September). An evaluation of mass-normalization using 50th and 95th percentile human body finite element models in frontal crash. In Proc. IRCOBI Conference.
- Davis, M., Koya, B., Schap, J. M., and Gayzik, F. S. (2016) Development and Full Body Validation of a 5th Percentile Female Finite Element Model. *Stapp Car Crash Journal*, 60: pp.509–544.
- Dumas, S., Bogges, B. M., Crandall, J., and MacMahon, C. (2003). Injury risk function for the small female wrist in axial loading. *Accident Analysis and Prevention* 35 (2003) 869–875
- Eppinger, R., Sun, E., Bandak, F., Haffner, M., Khaewpong, N., Maltese, M., and Zhang, A. (1999). Development of improved injury criteria for the assessment of advanced automotive restraint systems: II. National Highway Traffic Safety Administration National Transportation Biomechanics Research Center (NTBRC)
- Fahlstedt, M., Meng, S., and Kleiven, S. (2022). Influence of Strain Post-Processing on Brain Injury Prediction. *Journal of Biomechanics*, 132, 110940.
- Forman, J. L., Kent, R. W., Mroz, K., Pipkorn, B., Bostrom, O., and Segui-Gomez, M. (2012, October). Predicting rib fracture risk with whole-body finite element models: development and preliminary evaluation of a probabilistic analytical framework. In *Annals of Advances in Automotive Medicine/Annual Scientific Conference* (Vol. 56, p. 109). Association for the Advancement of Automotive Medicine.
- Forman, J., Perry, B., Alai, A., Freilich, A., Salzar, R., and Walilko, T. (2014). Injury tolerance of the wrist and distal forearm to impact loading onto outstretched hands. *Journal of trauma and acute care surgery*, 77(3), S176-S183.
- Gayzik, F. S., Hamilton, C. A., Tan, J. C., McNally, C., Duma, S. M., Klinich, K. D., and Stitzel, J. D. (2009). A multi-modality image data collection protocol for full body finite element model development. *SAE Technical Paper*, (2009-01), 2261.
- Gayzik, F. S., Moreno, D. P., Geer, C. P., Wuertzer, S. D., Martin, R. S., and Stitzel, J. D. (2011). Development of a full body CAD dataset for computational modeling: a multi-modality approach. *Annals of biomedical engineering*, 39(10), 2568-2583.
- Ghaffari, G., Brolin, K., Bråse, D., Pipkorn, B., Svanberg, B., Jakobsson, L., and Davidsson, J. (2018). Passenger kinematics in lane change and lane change with braking maneuvers using two belt configurations: standard and reversible pre-pretensioner. In Proc. IRCOBI Conference.
- Ghaffari, G., Brolin, K., Pipkorn, B., Jakobsson, L., and Davidsson, J. (2019). Passenger muscle responses in lane change and lane change with braking maneuvers using two belt configurations: Standard and reversible pre-pretensioner. *Traffic injury prevention*, 20 (sup1), S43-S51.
- Ghaffari, G., and Davidsson, J. (2021). Female kinematics and muscle responses in lane change and lane change with braking maneuvers. *Traffic injury prevention*, 22(3), 236-241.
- Huang, Y., King, A.I., and Cavanaugh, J.M. (1994) Finite element modeling of gross motion of human cadavers in side impact. *Stapp Car Crash Journal* 38.

- Hwang, E., Hallman, J., Klein, K., Rupp, J., Reed, M., and Hu, J., (2016). Rapid Development of Diverse Human Body Models for Crash Simulations through Mesh Morphing. SAE Technical Paper 2016-01-1491, 2016, doi:10.4271/2016-01-1491
- Iraeus, J., and Pipkorn, B. (2019). Development and Validation of a Generic Finite Element Ribcage (to be used for) Strain-based Rib Fracture Prediction. In Proc. IRCOBI Conference.
- Iraeus, J., Brolin, K., and Pipkorn, B. (2020). Generic finite element models of human ribs, developed and validated for stiffness and strain prediction–To be used in rib fracture risk evaluation for the human population in vehicle crashes, *Journal of the mechanical behavior of biomedical materials*: 103742.
- Kemper, A. R., McNally, C., Kennedy, E. A., Manoogian, S. J., Rath, A. L., and Ng, T. P. (2005). Material properties of human rib cortical bone from dynamic tension coupon testing. *Stapp Car Crash Journal* 49, 199–230.
- Kemper, A. R., McNally, C., Pullins, C. A., Freeman, L. J., Duma, S. M., and Rouhana, S. M. (2007). The biomechanics of human ribs: material and structural properties from dynamic tension and bending tests. *Stapp Car Crash Journal*. 51, 235–273.
- Klein, K., Hu, J., Reed, M., Hoff, C., and Rupp, J. (2015). Development and validation of statistical models of femur geometry for use with parametric finite element models, *Annals of Biomedical Engineering*, 43: 2503-14
- Kleiven, S. (2006). Evaluation of head injury criteria using a finite element model validated against experiments on localized brain motion, intracerebral acceleration, and intracranial pressure. *IJCrash2006Vol.11No.1pp.65–79*
- Kleiven, S. (2007). Predictors for Traumatic Brain Injuries Evaluated through Accident Reconstruction. *Stapp Car Crash Journal*, 51, pp. 81-114.
- Kleiven, S., and Hardy, W. N. (2002). Correlation of an FE model of the human head with experiments on localized motion of the brain – consequences for injury prediction. *Stapp Car Crash Journal*, 45.
- Kleiven, S., and von Holst, H. (2002a). Consequences of head size following trauma to the human head. *J Biomech*, 35 (2) 153–160. 33.
- Kleiven, S., and von Holst, H. (2002b). Consequences of brain volume following impact in prediction of subdural hematoma evaluated with numerical techniques. *Traffic Injury Prevention*, 2002b 3 (4) 303–310.
- Laituri, T. R., Prasad, P., Sullivan, K., Frankstein, M., and Thomas, R. S. (2005). Derivation and evaluation of a provisional, age-dependent, AIS3+ thoracic risk curve for belted adults in frontal impacts. SAE Technical Paper, (2005-01), 0297.
- Larsson, K-L., Blennow, A., Iraeus, J., Pipkorn, B., and Lubbe, N. (2021). Rib Cortical Bone Fracture Risk as a Function of Age and Rib Strain: Updated Injury Prediction Using Finite Element Human Body Models. *Front. Bioeng. Biotechnol.* 9:677768. doi: 10.3389/fbioe.2021.677768
- Larsson, E., Iraeus, J., Fice, J., Pipkorn, B., Jakobsson, L., Brynskog, E., and Davidsson, J. (2019). Active human body model predictions compared to volunteer response in experiments with braking, lane change, and combined maneuvers. In IRCOBI Conf. Proc.
- Larsson, E., Ghaffari, G., Iraeus, J., and Davidsson, J. (2022). Passenger Kinematics Variance in Different Vehicle Maneuvers–Biomechanical Response Corridors Based on Principal Component Analysis. In IRCOBI Conf. Proc.
- Leledakis, A., Östh, J., Davidsson, J., and Jakobsson, L. (2021). The influence of car passengers’ sitting postures in intersection crashes. *Accident Analysis and Prevention*, 157, 106170.
- Leledakis, A., Östh, J., Iraeus, J., Davidsson, J., and Jakobsson, L. (2022) The Influence of Occupant’s Size, Shape and Seat Adjustment in Frontal and Side Impacts. In IRCOBI Conf. Proc.
- Mendoza-Vazquez, M., Brolin, K., Davidsson, J., and Wisnans, J. (2013). Human rib response to different restraint systems in frontal impacts: a study using a human body model. *International Journal of Crashworthiness*, 18(5), 516-529.

- Ólafsdóttir, J. M., Brolin, K., Blouin, J. S., and Siegmund, G. P. (2015). Dynamic spatial tuning of cervical muscle reflexes to multidirectional seated perturbations. *Spine*, 40(4), E211-E219.
- Ólafsdóttir, J. M., Östh, J., and Brolin, K. (2019). Modelling reflex recruitment of neck muscles in a finite element human body model for simulating omnidirectional head kinematics. In *IRCOBI Conf. Proc.*
- Ólafsdóttir, J. M., Östh, J., Davidsson, J., and Brolin, K. (2013). Passenger kinematics and muscle responses in autonomous braking events with standard and reversible pre-tensioned restraints. In *Proc. IRCOBI Conference.*
- Östh, J., Brolin, K., and Happee, R. (2012a). Active muscle response using feedback control of a finite element human arm model. *Computer methods in biomechanics and biomedical engineering*, 15(4), 347-361.
- Östh, J., Brolin, K., Carlsson, S., Wismans, J., and Davidsson, J. (2012b). The occupant response to autonomous braking: a modeling approach that accounts for active musculature. *Traffic injury prevention*, 13(3), 265-277.
- Östh, J., Ólafsdóttir, J. M., Davidsson, J., and Brolin, K. (2013). Driver kinematic and muscle responses in braking events with standard and reversible pre-tensioned restraints: validation data for human models. *Stapp Car Crash Journal*, 57.
- Östh, J., Eliasson, E., Happee, R., and Brolin, K. (2014). A method to model anticipatory postural control in driver braking events. *Gait and posture*, 40(4), 664-669.
- Östh, J., Brolin, K., and Bråse, D. (2015). A human body model with active muscles for simulation of pretensioned restraints in autonomous braking interventions. *Traffic injury prevention*, 16(3), 304-313.
- Östh, J., Mendoza-Vazquez, M., Linder, A., Svensson, M. Y., and Brolin, K. (2017). The VIVA OpenHBM finite element 50th percentile female occupant model: whole body model development and kinematic validation. In *IRCOBI Conf. Proc.*
- Östh, J., Bohman, K., and Jakobsson, L. (2020). Evaluation of kinematics and restraint interaction when repositioning a driver from a reclined to an upright position prior to frontal impact using active human body model simulations. In *IRCOBI Conf. Proc.*
- Östh, J., Pipkorn, B., Forsberg, J., and Iraeus, J. (2021). Numerical reproducibility of Human Body Model crash simulations. In *Proc. IRCOBI Conference.*
- Östh, J., Larsson, E., and Jakobsson, L. (2022). Human body model muscle activation influence on crash response. In *IRCOBI Conf. Proc.*
- Östmann, M., and Jakobsson, L. (2016). An examination of pre-crash braking influence on occupant crash response using an active human body model. In *Proc. IRCOBI Conference.*
- Park, G., Kim, T., Subit, D., Donlon, J. P., Crandall, J. R., Svendsen, A., and Markusic, C. (2014). Evaluation of biofidelity of finite element 50th percentile male human body model (GHBMC) under lateral shoulder impact conditions. In *IRCOBI Conf. Proc.*
- Pipkorn, B., Alvarez, V., Fahlsted, M., and Lundin, L. (2020). Head Injury Risks and Countermeasures for a Bicyclist Impacted by a Passenger Vehicle. In *Proc. IRCOBI Conference.*
- Pipkorn, B., Östh, J., Brynskog, E., Larsson, E., Rydqvist, L., Iraeus, J., and Jakobsson, L. (2021). Validation of the SAFER Human Body Model Kinematics in Far-Side Impacts. In *Proc. IRCOBI Conference.*
- Poulard, D., Subit, D., Donlon, J. P., and Kent, R. W. (2015). Development of a computational framework to adjust the pre-impact spine posture of a whole-body model based on cadaver tests data. *Journal of biomechanics*, 48(4), 636-643.
- Reed, M. P., and Ebert, S. M. (2013). Elderly occupants: posture, body shape, and belt fit. University of Michigan, Ann Arbor, Transportation Research Institute.
- Robbin, S. (2001). HUMOS: Human model for safety – a joint effort towards the development of a refined human-like car occupant model, Proceedings of the 17th Conference on Enhanced Safety of Vehicles
- Roberts, C.W. (2020) Sex-based Geometric Differences in the Lower Extremity and Their Effect on Injury in the Automotive Crash Environment. PhD Thesis, University of Virginia, VA, USA.

- Ruan, J., El-Jawahri, R., Chai, L., Barbat, S., and Prasad, P. (2003) Prediction and analysis of human thoracic impact responses and injuries in cadaver impacts using a full human body finite element model. *Stapp Car Crash Journal* 47.
- Saito, H., Matsushita, T., Pipkorn, B., and Boström, O. (2016). Evaluation of frontal impact restraint system in integrated safety scenario using human body model with PID controlled active muscles. In Proc. IRCOBI Conference.
- Schneider, L. W. (1983). Development of anthropometrically based design specifications for an advanced adult anthropomorphic dummy family, volume 1. final report.
- Schwartz, D., Guleyupoglu, B., Koya, B., Stitzel, J. D., and Gayzik, F. S. (2015). Development of a computationally efficient full human body finite element model. *Traffic injury prevention*, 16(sup1), S49-S56.
- Shi, X., and Cao, L., (2014). A statistical human rib cage geometry model accounting for variations by age, sex, stature and body mass index. *Journal of Biomechanics*, 2014. 47(10): p. 2277-2285
- Toyota Motor Cooperation. (2008). Users' Guide of Computational Human Model THUMS (Total HUMAN Model for Safety), AM50 Occupant Model: Version 3.0-080225. Toyota Central RandD Labs., Inc.
- Viano, D. (1989). Biomechanical Responses and Injuries in Blunt Lateral Impact. SAE Paper 892432.
- Wass, J., Östh, J., and Jakobsson, L. (2022). Active Human Body Model Simulations of Whole-Sequence Braking and Far-Side Side-Impact Configurations. In Proc. IRCOBI Conference.
- Yulong, W., Cao, L., Bai, Z., Reed, M., Rupp, J., Hoff, C., and Hu, J. (2016). A parametric ribcage geometry model accounting for variations among the adult population, *Journal of biomechanics*, 49: 2791-98.
- Watanabe, R., Katsuhara, T., Miyazaki, H., Kitagawa, Y., and Yasuki, T. (2012). Research of the relationship of pedestrian injury to collision speed, car-type, impact location and pedestrian sizes using human FE model (THUMS Version 4). *Stapp Car Crash Journal*, 56, 269.
- Weaver, A., Schoell, S., Nguyen, C., Lynch, S., and Stitzel, J. (2014). Morphometric analysis of variation in the sternum with sex and age, *Journal of morphology*, 275: 1284-99.

COMPARISON OF HEAD-NECK KINEMATICS BETWEEN ISOLATED FINITE ELEMENT (FE) HEAD-NECK MODEL AND FULL-BODY MODEL IN LOW SEVERITY REAR-END IMPACT

I Putu A., Putra¹

Johan, Iraeus¹

Fusako, Sato^{1,2}

Mats Y., Svensson¹

Astrid, Linder^{1,3}

Robert, Thomson¹

¹Division of Vehicle Safety, Department of Mechanics and Maritime Sciences, Chalmers University of Technology, Gothenburg, Sweden

²Vehicle Safety Research Group, Safety Research Division, Japan Automobile Research Institute
2530 Karima, Tsukuba, Ibaraki, Japan

³The Swedish National Road and Transport Research Institute, Gothenburg, Sweden

Paper Number 23-0276

ABSTRACT

The objective of the present study was to analyze whether the kinematics of an isolated head-neck model can replicate those observed on a whole body model in order to reduce simulation time in development or optimization tasks. Previous studies have shown how muscle controllers improved head-neck kinematics responses over a passive neck muscle implementation. These studies used volunteer T1 displacement time histories prescribed on the model T1 as the loading input to develop the neck controller characteristics. It was not clear whether the implementation of a controller based on volunteer kinematics with an isolated head-neck model was directly transferable to a full-body model. The current study shows that the head-neck model produced almost identical responses as the full body model for the first 200ms of the event for most kinematic variables. The head rotational displacement corresponded well during the first 150ms. The isolated head-neck model predicted more displacement and rotations than when mounted on a full-body model. The current simplification of a head-neck model still produced reasonable kinematic responses during the critical time period to assess soft tissue neck injuries, making it suitable for developing and tuning neck muscle controllers.

INTRODUCTION

Finite Element (FE) Human Body Models (HBMs) have been a powerful and essential tool when studying road user safety. However, until recently, FE HBMs that represented average female anthropometry did not exist. To fill this gap, an open-source HBM of the 50th percentile female stature called VIVA+ 50F (John et al. 2022a, 2022b) was developed (John et al. 2022a, 2022b) and validated against Post-Mortem Human Subject (PHMS) responses in a rear impact (John et al. 2022b). It was further developed by adding active reflexive neck muscle controllers (Putra et al. 2022). Neck muscle activities have been shown to influence the head-neck kinematics during rear-impact volunteer tests (Brault et al. 2000, Siegmund et al. 2003, Blouin et al. 2006, G.P Siegmund, 2011, Dehner et al. 2013, Mang et al. 2015).

With added muscle controllers, the VIVA+ 50F head and neck kinematics was improved over a passive neck implementation compared to volunteer responses (Putra et al. 2022). The model used in previous studies consisted of a head-neck model with the volunteer T1 displacement time histories prescribed on the model T1. Therefore, it was not clear whether the implementation and optimization of the active muscle controller using the isolated head-neck model could also be used in the full-body model. In addition, only a female model was available at the time of the implementing an active neck muscle controller. Consequently, a direct comparison between female and male models could not be conducted.

Based on identified limitations, the objective of the present study was to analyze whether the isolated head-neck model can replicate the full-body model head-neck kinematics and be used to develop an active muscle controller strategy.

MATERIAL AND METHODS

The overall flowchart of the study is presented in Figure 1 below. Similar processes for both the average female and male VIVA+ models, VIVA+ 50F and 50M, were conducted, but only the female model is shown in the flowchart. First, the full-body model was run, using the boundary conditions matching the volunteers' test setup to generate the T1 linear and rotational accelerations. The generated T1 accelerations were then prescribed to the isolated VIVA+ head-neck models. This was conducted to ensure that both models had similar T1 accelerations. Finally, the head C.G. and cervical vertebra C.G. kinematics of the VIVA+ full-body models and VIVA+ head-neck models were compared and analyzed.

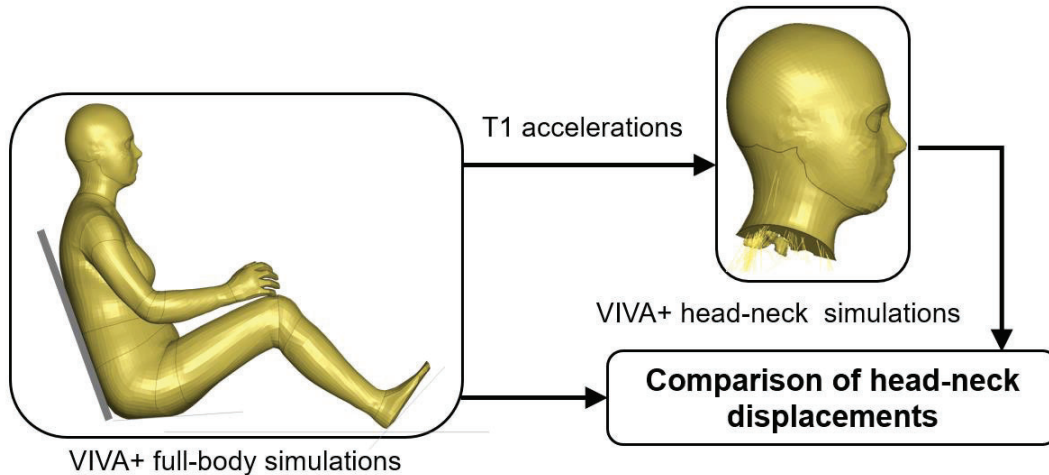


Figure. 1 Flow Chart of the Present Study's Methods

VIVA+ Female and Male Occupant Human Body Model

The baseline of VIVA+ FE HBM is an average 50th percentile female model, which is morphed to create an average 50th percentile male (Figure 2). The male and female models have identical elements definitions with the gender specific nodal coordinates defined by several statistical shape models describing the outer body shape, ribcage, femur, tibia and pelvis (John et al. 2022a). Besides geometry changes, differences in male and female head mass, soft tissues densities, knee ligaments characteristics, and quadriceps muscle stiffness were included (John et al. 2022a). In the present study, sub-models that consist only of head-neck were created by cutting both average female and male models below the first thoracic vertebrae (T1).

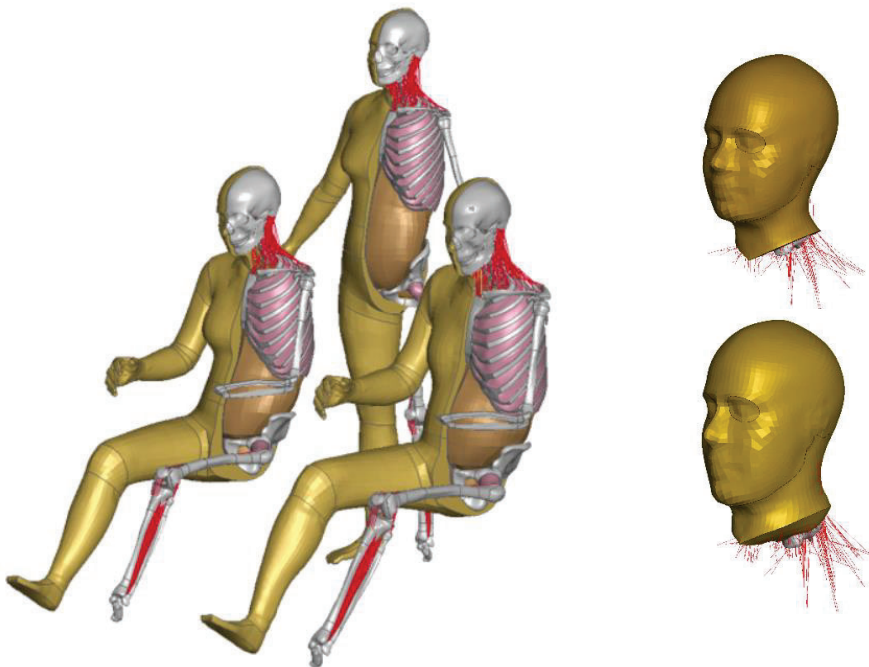


Figure. 2 VIVA+ Finite Element Human Body Models and Isolated VIVA+ 50F and 50M Head-Neck Models

Rear end Impact Volunteer Test based on Sato et al. 2014

Volunteer kinematic data was derived from the volunteer test series of Sato et al. (2014), which was a low-speed, rear-impact sled test with a delta velocity of 5.8km/h and peak acceleration of 42m/s^2 . Four male volunteers and two female volunteers were seated in a rigid seat (seatback angle 20 degrees from vertical) without a head restraint. Head C.G displacements and accelerations, T1 C.G displacements, and C1-C7 rotational displacements (recorded with a high-speed X-ray camera) data were used in the present study to compare the VIVA+ models kinematics.

Simulation Set-up

Comparisons of head and neck kinematics responses between the VIVA+ head-neck models and the full-body models in their passive neck muscle configurations were conducted. The aim was to evaluate whether the head-neck system of the VIVA+ model would generate similar head and neck kinematics in the isolated head-neck compared to the full-body model. This would demonstrate that the isolated model was a suitable basis for active muscle controller optimizations to identify the controller characteristics (Putra et al. 2020).

Full HBM model simulations of the VIVA+ 50F and 50M models were done following the Sato et al. (2014) set-up (Figure 3) to generate T1 accelerations. Sled acceleration from the experiment was prescribed on the seat model. The duration of each simulation was 650ms, with the first 450ms used to settle the model under gravitational acceleration. The T1 accelerations produced by the full-body model simulations were then used to prescribe the T1 motion for the isolated head-neck models. In the head-neck model, the lower nodes of the skin and several nodes of the soft tissues were constrained to move with the T1 (Figure 4).

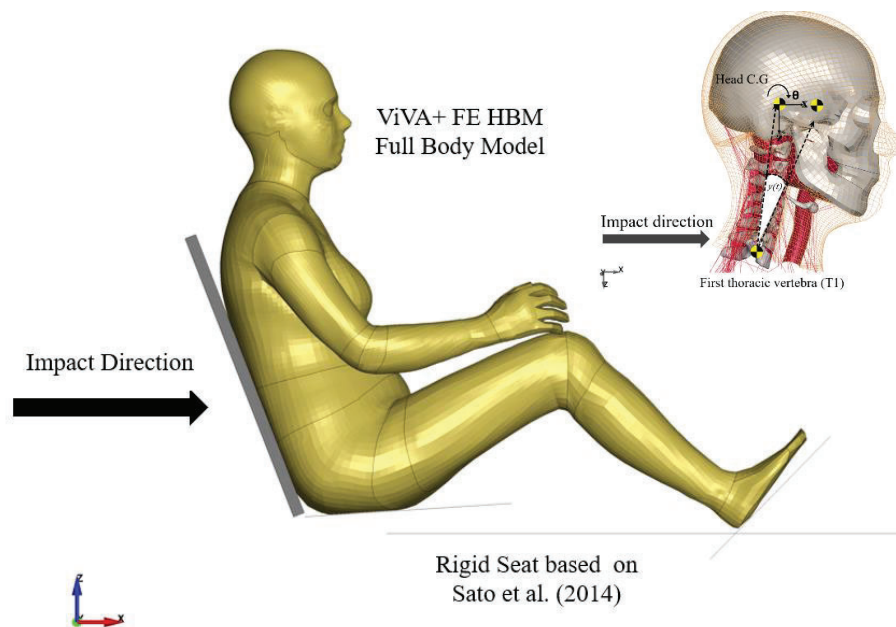


Figure. 3 Simulations set-up of VIVA+ 50F and 50M Head-Neck and Full Body Model based on Sato et al. (2014).

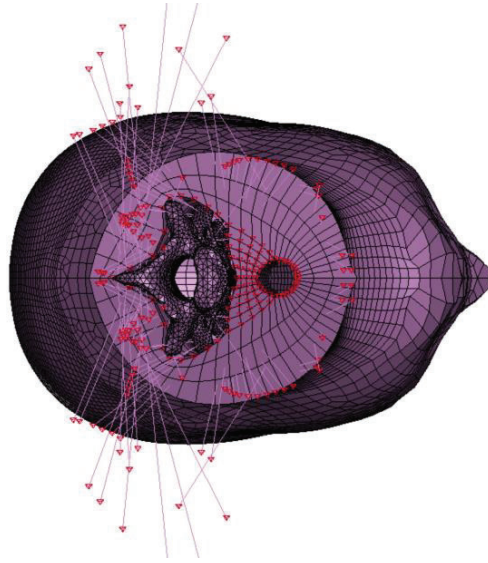


Figure. 4 List of Constrained Nodes to Allow the Isolated Head-Neck Model Moves with the T1

RESULTS

The T1 C.G x- and z-linear displacement and T1 rotational y-displacement of the VIVA+ 50F and 50M are presented with the volunteer kinematics in Figure 5. The goal of this study was to compare the isolated head-neck kinematics to those produced by a full HBM simulation. The full HBM calibration and validation to the sled test was beyond the scope of this study and not necessary for the purpose of model comparison. Although the responses are not identical, the results of the simulations are similar to those of the volunteers.

The T1 C.G. displacements (x- and z-) and T1 C.G. y-rotation from full-body simulations (Figure 5) were then prescribed to the T1 C.G. of the head-neck models. Figure 6 show that the female head-neck model could replicate the full-size female model's responses for the first 200ms except for head C.G. rotational displacement 7) when both models have identical T1 kinematics. The head-neck model's head C.G. rotations only followed the full-body model's head rotations for 150ms. These responses were observed for both female (Figure 6) and male (Figure 7).

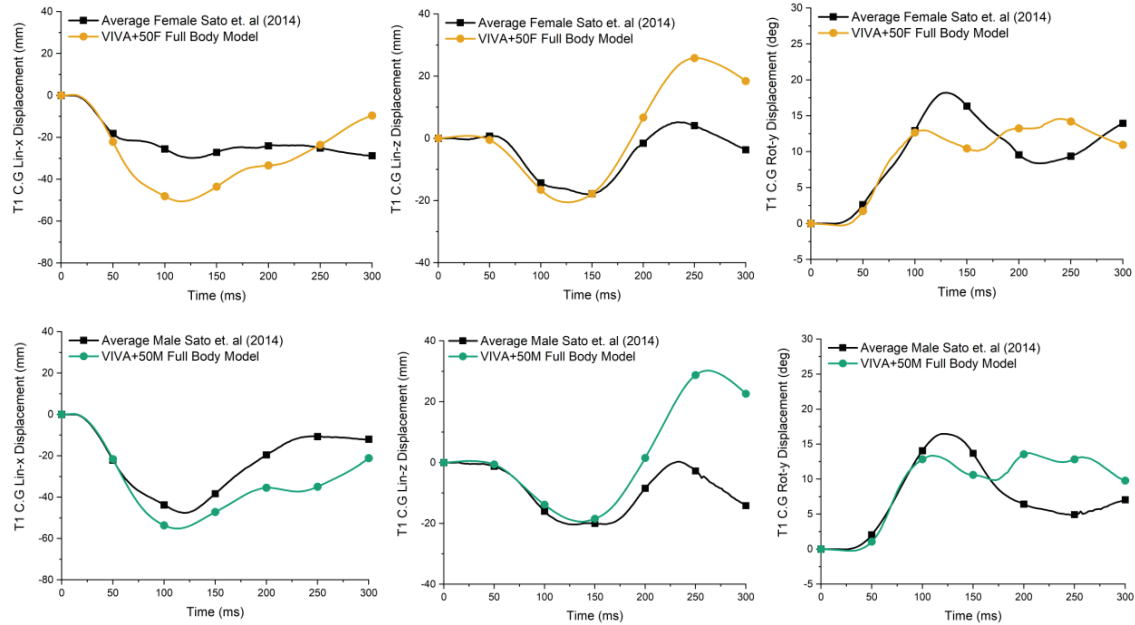


Figure 5. Comparison of T1 C.G Displacements and Rotation based on Full-Body Model Simulation with VIVA + 50F and VIVA+ 50M and volunteer tests from Sato et al. (2014) at 5.8km/h

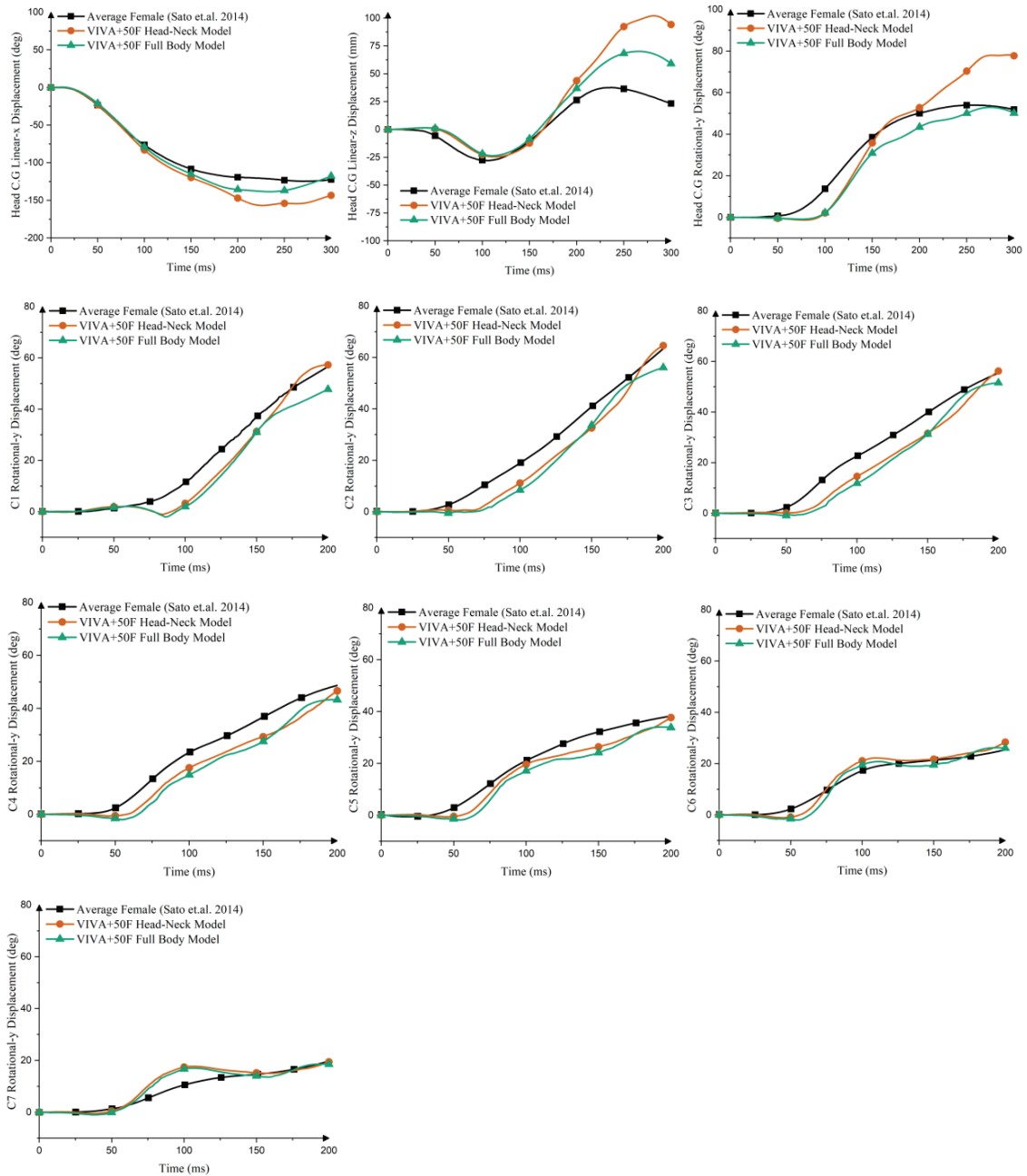


Figure 6. Comparison of Head-Neck Kinematics of VIVA+ Head-Neck Female Model and Full-Body Female Model with Similar T1 Displacement and Rotations as Input.

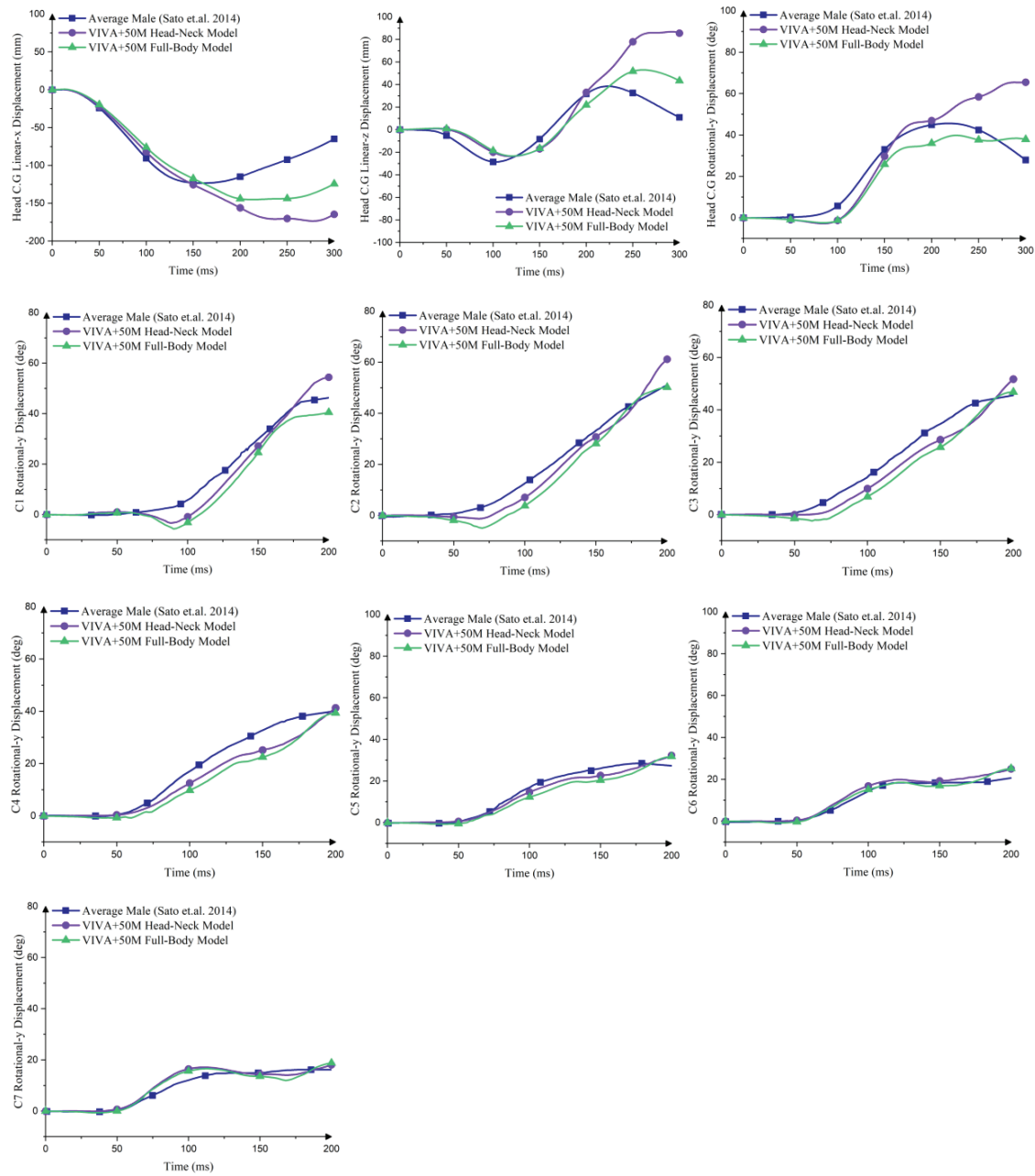


Figure 7. Comparison of Head-Neck Kinematics of VIVA+ Head-Neck Male Model and Full-Body Male Model with Similar T1 Displacement and Rotations as Input.

DISCUSSION

The objective of the current study was to assess whether a head-neck model with prescribed T1 displacements and rotations can be used to develop an active muscle controller strategy. The main reason was that running active muscle controller optimizations using the full-body model is computationally very expensive. However, running an isolated head-neck model under similar loading conditions reduces computational time by almost 75%.

The comparison between head-neck kinematics of a head-neck model and full-body model for both female and male models revealed that the head-neck model produced almost identical responses up until 200ms for most kinematic variables but only until 150ms for the head rotational displacement. Currently, most of the whiplash injuries hypotheses are associated with the retraction phase of the neck (Svensson et al. 1993, Yoganandan et al. 2002, Ono et al. 2006), which occurs in the first 150ms after impact. Based on these hypotheses and the simulation results, it was suggested that the isolated head-neck model could be used to develop an active muscle controller that produces similar head-neck kinematics responses as a full-body model for the duration of the event where soft tissue neck injuries are hypothesized to occur.

The main differences in kinematics between the head-neck model and full-body of the VIVA+ 50F and 50M models occurred at 150ms (in head rotational y-displacement) and at 200ms (in head linear x- and z-displacement). The head-neck model most often produced more displacements and rotations than the full-body model. The main reason for the less stiff response of the head-neck model can be explained by the difference in modelling the neck's soft tissue and skin. In the full-body model, the neck's soft tissue and skin are "seamlessly" connected to the soft tissues and skin of the upper torso with the lower muscle attachments moving with their anatomical structures. However, in the head-neck model the lower nodes of the skin and several nodes of the soft tissues were constrained to move with the T1 vertebra. The lower muscle attachments were also fixed to a plane that only followed the motions of T1 and not their true anatomical motions.

Figure 4 shows that not all nodes on the lower neck surface were constrained. Simulations conducted with this definition resulted in an overly stiff response. The interaction of structures that cross this intersection between the neck and upper torso vary across the cross-section and the constraints illustrated in Figure 4 gave the best results in the study. Further investigations of the boundary conditions could produce better results if the sub-model should agree with the full model over a longer time period. This would require even further investigation of the neck muscle attachments below the section plane as these affect the muscle forces and resulting influence on the response.

CONCLUSIONS

Computer simulations of an isolated head-neck complex can reasonably duplicate the associated kinematics observed in a full-body model. Reducing the model to a sub-model with only the relevant body segments reduced simulation times by 75%. This model reduction facilitates optimization studies to obtain neck control characteristics. These optimizations require 150+ simulations and more than one optimization run are typically needed to explore the model parameter solution space. The boundary conditions for the sub-model are important to define and the existing implementation is suitable for the study of head-neck kinematics in low severity rear impacts.

ACKNOWLEDGEMENT

This study was conducted within the project VIRTUAL and was received funding from the European Union Horizon 2020 Research and Innovation Programme under Grant Agreement No. 768960.

EU Trademark Application No. 01880153

REFERENCES

- Blouin, J. S., Inglis, J. T., and Siegmund, G. P. (2006). Auditory startle alters the response of human subjects exposed to a single whiplash-like perturbation. *Spine (Phila. Pa. 1976)*. 31, 146–154. doi: 10.1097/01.brs.0000195157.75056.df.
- Brault, J. R., Siegmund, G. P., and Wheeler, J. B. (2000). Cervical muscle response during whiplash: Evidence of a lengthening muscle contraction. *Clin. Biomech.* 15, 426–435. doi: 10.1016/S0268-0033(99)00097-2.
- Dehner, C., Schick, S., Kraus, M., Scola, A., Hell, W., and Kramer, M. (2013). Muscle Activity Influence on the Kinematics of the Cervical Spine in Frontal Tests. *Traffic Inj. Prev.* 14, 607–613. doi: 10.1080/15389588.2012.734937.
- John J, Klug C, Kranjec M, Svenning E and Iraeus J (2022a) Hello, world! VIVA+: A human body model lineup to evaluate sex-differences in crash protection. *Front. Bioeng. Biotechnol.* 10:918904. doi:10.3389/fbioe.2022.918904
- John, J., Putra, I. P. A., and Iraeus, J. (2022b). Finite element human body models to study sex-differences in whiplash: Validation of VIVA+ passive responses in rear-impact. IRCOBI Conference. IRC-22-36, Porto, Portugal
- Mang, D. W. H., Siegmund, G. P., Brown, H. J., Goonetilleke, S. C., and Blouin, J. S. (2015). Loud preimpact tones reduce the cervical multifidus muscle response during rear-end collisions: A potential method for reducing whiplash injuries. *Spine J.* 15, 153–161. doi: 10.1016/j.spinee.2014.08.002.
- Ono, K., Ejima, S., Suzuki, Y., Kaneoka, K., Fukushima, M., and Ujihashi, S. (2006). Prediction of Neck Injury Risk Based on the Analysis of Localized Cervical Vertebral Motion of Human Volunteers During Low-Speed Rear-end impacts. *IRCOBI Conf. Proc.*, 103–113
- Putra, I. P. A., Iraeus, J., Sato, F., Svensson, M. Y., & Thomson, R. (2022). Finite element human body models with active reflexive muscles suitable for sex based whiplash injury prediction. *Frontiers in bioengineering and biotechnology*, 10, 968939. <https://doi.org/10.3389/fbioe.2022.968939>
- Putra, I. P. A., Iraeus, J., Sato, F., Svensson, M. Y., Linder, A., and Thomson, R. (2020). Optimization of Female Head–Neck Model with Active Reflexive Cervical Muscles in Low Severity Rear Impact Collisions. *Ann. Biomed. Eng.*, 1–14.
- Sato, F., Nakajima, T., Ono, K., and Svensson, M. (2014). Dynamic Cervical Vertebral Motion of Female and Male Volunteers and Analysis of its Interaction with Head/Neck/Torso Behavior during Low-Speed Rear. *Ircobi.Org*, 227–249. Available at: http://www.ircobi.org/downloads/irc14/pdf_files/31.pdf.
- Siegmund, G. P. (2011). What occupant kinematics and neuromuscular responses tell us about whiplash injury. *Spine (Phila. Pa. 1976)*. 36, S175–S179. doi: 10.1097/BRS.0b013e3182387d71.
- Siegmund, G. P., Sanderson, D. J., Myers, B. S., and Inglis, J. T. (2003). Awareness affects the response of human subjects exposed to a single whiplash-like perturbation. *Spine (Phila. Pa. 1976)*. 28, 671–679. doi: 10.1097/00007632-200304010-00010.
- Svensson, M. Y., Aldman, B., Hansson, H. a, Lövsund, P., Seeman, T., Suneson, a, et al. (1993). Pressure Effects in the Spinal Canal during Whiplash Extension Motion: A Possible Cause of Injury to the Cervical Spinal Ganglia. *Int. IRCOBI Conf. Biomech. Impacts*, 189–200.
- Yoganandan, N., Pintar, F. A., and Cusick, J. F. (2002). Biomechanical analyses of whiplash injuries using an experimental model. *Accid. Anal. Prev.* 34, 663–671. doi: 10.1016/S0001-4575(01)00066-5.